

NONDESTRUCTIVE EVALUATION OF THE EFFECTS OF CARBURIZING  
PROCESS PARAMETERS ON MICROSTRUCTURE AND RESIDUAL  
STRESS STATE OF SAE 9310 STEEL VIA MAGNETIC BARKHAUSEN  
NOISE METHOD

A THESIS SUBMITTED TO  
THE GRADUATE SCHOOL OF NATURAL AND APPLIED SCIENCES  
OF  
MIDDLE EAST TECHNICAL UNIVERSITY

BY

ZAFER YILDIRIM

IN PARTIAL FULFILLMENT OF THE REQUIREMENTS  
FOR  
THE DEGREE OF MASTER OF SCIENCE  
IN  
METALLURGICAL AND MATERIALS ENGINEERING

FEBRUARY 2022



Approval of the thesis:

**NONDESTRUCTIVE EVALUATION OF THE EFFECTS OF  
CARBURIZING PROCESS PARAMETERS ON MICROSTRUCTURE AND  
RESIDUAL STRESS STATE OF SAE 9310 STEEL VIA MAGNETIC  
BARKHAUSEN NOISE METHOD**

submitted by **ZAFER YILDIRIM** in partial fulfillment of the requirements for the degree of **Master of Science in Metallurgical and Materials Engineering, Middle East Technical University** by,

Prof. Dr. Halil Kalıpçılar  
Dean, Graduate School of **Natural and Applied Sciences** \_\_\_\_\_

Prof. Dr. C. Hakan Gür  
Head of the Department, **Metallurgical and Materials Engineering** \_\_\_\_\_

Prof. Dr. C. Hakan Gür  
Supervisor, **Metallurgical and Materials Engineering, METU** \_\_\_\_\_

**Examining Committee Members:**

Prof. Dr. Rıza Gürbüz  
Metallurgical and Materials Eng, METU \_\_\_\_\_

Prof. Dr. C.Hakan Gür  
Metallurgical and Materials Eng, METU \_\_\_\_\_

Prof. Dr. Benat Koçkar  
Mechanical Engineering., Hacettepe University \_\_\_\_\_

Assoc. Prof. Dr. Caner Şimşir  
Metallurgical and Materials Eng, METU \_\_\_\_\_

Assist. Prof. Dr. Eda Aydoğan Güngör  
Metallurgical and Materials Eng, METU \_\_\_\_\_

Date: 11.02.2022

**I hereby declare that all information in this document has been obtained and presented in accordance with academic rules and ethical conduct. I also declare that, as required by these rules and conduct, I have fully cited and referenced all material and results that are not original to this work.**

Name Last name : Yıldırım, Zafer

Signature :

## **ABSTRACT**

### **NONDESTRUCTIVE EVALUATION OF THE EFFECTS OF CARBURIZING PROCESS PARAMETERS ON MICROSTRUCTURE AND RESIDUAL STRESS STATE OF SAE 9310 STEEL VIA MAGNETIC BARKHAUSEN NOISE METHOD**

Yıldırım, Zafer

Master of Science, Metallurgical and Materials Engineering

Supervisor : Prof. Dr. C. Hakan Gür

February 2022, 103 pages

Carburizing is a surface treatment process applied for improving the surface hardness, wear resistance, and also fatigue life of some critical aerospace and automotive components, such as gears, bearings, and bushings. It consists of carbon diffusion into low-C steels in the austenitized condition which results in a carbon gradient along with the depth, then followed by quenching, sub-zero treatment, and tempering. In a carburized component, a strong and wear-resistant surface layer (the case) with compressive residual stress, as well as hardness and residual stress gradients from the case to the core is expected.

Residual stresses, which are critical for the performance and stability of the engineering components, are defined as the self-equilibrating elastic stresses in a component in the absence of external stresses, created during manufacturing. In carburized components, the C-gradient affects the phase transformations on cooling and, thus, the final patterns of the microstructure and the residual stress. Besides, depending on the carbon content, carburized steels may contain retained austenite up to 10%, which affects the magnitude and the depth profile of the residual stress, and also, the dimensional stability of the part.

Controlling the success of the carburizing process is vital to satisfy the design requirements and to guarantee safety with expected performance and lifetime. This necessitates practical, reliable, and time- and cost-effective non-destructive evaluation methods by the manufacturers. The aim of this thesis is to determine non-destructively the effects of the parameters of the carburizing process chain on microstructure, hardness, and residual stress state by using the Magnetic Barkhausen Noise (MBN) method.

In the experimental part, a series of SAE 9310 steel specimens having different microstructure and residual stress states were prepared by altering the cooling rate (air-cooling, quenching), the carburizing time (3h, 6h), the cryogenic treatment temperature (-25°C, -75°C, -100°C), and the tempering temperature (150°C, 300°C). The specimens were systematically characterized through metallographic investigations, hardness measurements, measurements of retained-austenite and residual stress by the XRD method, and MBN measurements. The results show that a good correlation exists between the results obtained by conventional methods and the parameters derived from the MBN signals.

Keywords: Magnetic Barkhausen Noise, Residual Stress, X-Ray Diffraction, Carburizing of Steel, Microstructure

## ÖZ

### **KARBÜRLEME PROSES PARAMETRELERİNİN SAE 9310 ÇELİĞİNDEKİ MİKRO YAPI VE KALINTI GERİLİM ÜZERİNDE OLUŞTURDUĞU ETKİLERİN BARKHAUSEN GÜRÜLTÜSÜ YÖNTEMİ İLE TAHRİBATSIZ İNCELENMESİ**

Yıldırım, Zafer  
Yüksek Lisans, Metalurji ve Malzeme Mühendisliği  
Tez Yöneticisi: Prof. Dr. C. Hakan Gür

Şubat 2022, 103 Sayfa

Karbürleme, dişliler, rulmanlar ve burçlar gibi bazı kritik havacılık ve otomotiv parçalarının yüzey sertliğini, aşınma direncini ve ayrıca yorulma ömrünü iyileştirmek için uygulanan bir yüzey işlemidir. Düşük karbonlu çeliklerin östenit fazında karbon difüzyonu sonucu karbon gradyan oluşumunu ve sonrasında su verme, sıfır altı işlem ve menevişleme işlemlerini kapsamaktadır. Karbürlenmiş bir parçada, yüzeyden çekirdeğe doğru sertlik ve kalıntı gerilim gradyanlarının yanı sıra basma kalıntı gerilimine sahip mukavemetli ve aşınmaya dayanıklı bir yüzey tabakası oluşur.

Kalıntı gerilmeler bir mühendislik parçasının performansı ve servis ömrü için önemli olan, parçanın imalat işlemleri esnasında oluşan elastik gerilmelerdir ve dış gerilmelerin yokluğunda parça içerisinde dengededir. Karbürlenmiş parçalarda, karbon gradyanı, soğutma üzerindeki faz dönüşümlerini ve dolayısıyla mikro yapının son halini ve kalıntı gerilmeyi etkiler. Ayrıca, karbon miktarına bağlı olarak, karbürlenmiş çelikler %10'a kadar kalıntı östenit içerebilir, bu da kalıntı gerilmenin

büyükliğini ve derinlik profilini ve ayrıca parçanın boyutsal kararlılığını etkilemektedir.

Karbürleme işleminin kontrolü, tasarım gerekliliklerini karşılamak, beklenen performans ve kullanım ömrünü garanti etmek için hayati önem taşır. Bu durum, üreticileri pratik, güvenilir, zaman ve maliyet açısından verimli, tahribatsız muayene yöntemlerine yöneltmektedir. Bu tezin amacı, karbürleme proses parametrelerinin mikroyapı, sertlik ve kalıntı gerilme durumu üzerindeki etkilerini Manyetik Barkhausen Gürültüsü (MBN) yöntemini kullanarak tahribatsız olarak belirlemektir.

Deney bölümünde, soğutma hızı (hava soğutma, su verme), karbürleme süresi (3 saat, 6 saat), kriyojenik işlem sıcaklığı ( $-25^{\circ}\text{C}$ ,  $-75^{\circ}\text{C}$ ,  $-100^{\circ}\text{C}$ ) ve meneviş sıcaklığı ( $150^{\circ}\text{C}$ ,  $300^{\circ}\text{C}$ ) değiştirilerek farklı mikroyapı ve kalıntı gerilme durumlarına sahip çeşitli SAE 9310 çelik numuneler hazırlanmıştır. Numuneler, metalografik incelemeler, sertlik ölçümleri, XRD yöntemiyle kalıntı ostenit ve kalıntı gerilim ölçümleri ve MBN ölçümleri yoluyla sistematik olarak karakterize edilmiştir. Sonuçlar, geleneksel yöntemlerle elde edilen sonuçlar ile MBN sinyallerinden elde edilen parametreler arasında iyi bir korelasyon olduğunu göstermektedir.

Anahtar Kelimeler: Manyetik Barkhausen Gürültü Metodu, Kalıntı Gerilme, X-Işını Kırılması, Çeliklerin Karbürlenmesi, Mikroyapı



To my family

## ACKNOWLEDGMENTS

First and foremost, I am deeply grateful to my supervisor Prof. Dr. C.Hakan Gür for his invaluable advice, continuous support, and patience through the study. It was a great honor to work with him. I would also like to express my special thanks to Assoc. Prof. Dr. Caner Şimşir for his guidance and for introducing me to the concept of X-Ray Diffraction residual stress measurements.

I would like to thank Dr. İbrahim Çam from METU-Central Laboratory for introducing me to the basics and theory of MBN measurements. I would like to extend my special thanks to Yahya Tunç for helping to sample preparations and X-Ray Diffraction measurements.

I would like to extend my sincere thanks to members of the Dynamic Systems Special Processes Department of Turkish Aerospace for manufacturing the samples. And especially, I would also like to thank Kadir Göker Önder for his continuous support and encouragement.

I wish to express my sincerest thanks to my parents Filiz and Cuma Yıldırım for all that I am, and my brother Onur Yıldırım.

Finally, I would like to thank my wife Hazal Yıldırım for giving me motivation and believing in me, it would be impossible for me to complete my study without her understanding.

## TABLE OF CONTENTS

ABSTRACT.....	v
ÖZ.....	vii
ACKNOWLEDGMENTS.....	x
TABLE OF CONTENTS.....	xi
LIST OF TABLES.....	xiii
LIST OF FIGURES.....	xiv
LIST OF ABBREVIATIONS.....	xix
LIST OF SYMBOLS.....	xx
INTRODUCTION.....	1
1.1    General.....	1
1.2    Motivation.....	2
1.3    Aim of Study.....	3
THEORY.....	5
2.1    Carburizing.....	5
2.1.1    Pack Carburizing.....	5
2.1.2    Salt Bath Carburizing.....	6
2.1.3    Gas Carburizing.....	6
2.2    Residual Stress: Formation and Relief.....	11
2.3    Residual Stress Measurements by XRD Method.....	13
2.4    Magnetic Barkhausen Noise Method.....	17
2.5    Retained Austenite Measurement by XRD.....	20
LITERATURE REVIEW.....	23

EXPERIMENTAL PROCEDURE.....	33
4.1 Material and Sample Preparation.....	33
4.2 Heat Treatment Processes .....	37
4.3 Microstructural Investigation.....	39
4.4 Retained Austenite Measurement .....	39
4.5 Hardness Measurements .....	41
4.6 Residual Stress Measurement .....	43
4.7 Magnetic Barkhausen Noise Measurements.....	45
RESULTS AND DISCUSSION.....	49
5.1 Microstructural Investigation.....	49
5.2 Retained Austenite Measurements.....	55
5.3 Hardness Test Results .....	60
5.4 Results of Magnetic Barkhausen Noise Measurements.....	66
5.4.1 Magnetic Hysteresis Curves .....	75
5.5 XRD Results .....	81
5.5.1 Residual Stress Measurements .....	81
CONCLUSION .....	89
6.1 Recommendations for Further Studies .....	91
REFERENCES .....	93
APPENDICES .....	101
A. TTT Diagrams of 9310 Steel at Initial, 3 h and 6 h Carburized Condition	101
B. CTT Diagrams of 9310 Steel at Initial, 3 h and 6 h Carburized Condition	102

## LIST OF TABLES

### TABLES

Table 3.1 Sample tempering time and corresponding average grain and carbide size [32] .....	25
Table 4.1 Chemical composition of SAE 9310 (AMS 6265N) standard and the steel used .....	33
Table 4.2 Sample identification according to their process routes .....	38
Table 4.3 Sample preparation recipe for metallographic examination .....	39
Table 4.4 The phase transition temperatures of samples, calculated by JMatPro, based on the carbon content at the surface.....	41
Table 5.1 Chemical composition of the grain boundary and the grain taken by EDS .....	54
Table 5.2 Retained-austenite content of the specimens .....	57
Table 5.3 Results of the hardness measurements: surface and core hardness, and the depths corresponding to 697HV and 513HV .....	65
Table 5.4 Results of MBN measurements .....	74
Table 5.5 Magnitudes of principal surface residual stresses (effective) measured by XRD methods.....	83
Table 5.6 Depth profiles of residual stresses for some samples, measured by XRD .....	85
Table 5.7 Surface hardness, MBN, retained austenite, and the principal surface residual stress values at electropolished surfaces of the samples .....	87

## LIST OF FIGURES

### FIGURES

Figure 2.1. Schematic representation of carbon diffusion into steel [4] .....	6
Figure 2.2. Mass transformation of carbon in the gas environment [38] .....	7
Figure 2.3. The typical carburizing cycle of steels.....	9
Figure 2.4. Stages of quenching and cooling rate curve [8].....	10
Figure 2.5. Effect of carbon content in steel on TTT diagram [39] .....	11
Figure 2.6. Transition line of the case and the core [57].....	12
Figure 2.7. Representation of diffraction of X-Rays by a crystal lattice [40].....	14
Figure 2.8. Principal axes of the strain [10] .....	15
Figure 2.9. Schematic of tilting and angles of XRD [12].....	16
Figure 2.10. Graph of interplanar spacing versus $\sin^2(\psi)$ [13].....	16
Figure 2.11. Magnetic domains a) random orientation b) aligned in the direction of an applied magnetic field [15].....	17
Figure 2.12. Magnetic hysteresis curve and magnetic jumps [16].....	18
Figure 2.13. Schematic of applied voltage versus Magneto-elastic Parameter (MP) .....	18
Figure 2.14. Example of MBN results [19].....	19
Figure 2.15. MBN patterns of different stress types and hardness values [20].....	20
Figure 2.16. Representation of XRD machine [22].....	21
Figure 3.1. RMS voltage obtained by MBN method versus applied current of samples with different tempering time [32] .....	24
Figure 3.2. MBN pattern of untempered, standard tempered and over tempered samples with 125 Hz frequency [33].....	26
Figure 3.3. MBN pattern of untempered, standard tempered and over tempered samples with 4 Hz frequency [33].....	26
Figure 3.4. Hardness test results of martensite, tempered martensite, fine pearlite-ferrite and coarse pearlite-ferrite structures for SAE 1040 and SAE 4140 [34] .....	27

Figure 3.5. Magnetoelastic parameter measured at MBN method of martensite, tempered martensite, fine pearlite-ferrite and coarse pearlite-ferrite structures for SAE 1040 and SAE 4140 [34] .....	28
Figure 3.6. Hardness values versus corresponding RMS values of MBN signals [35].....	29
Figure 4.1. Some of the manufactured specimens .....	34
Figure 4.2. Microstructure of incoming material, 200x.....	35
Figure 4.3. A representative microstructure after pre-hardening, 200x.....	36
Figure 4.4. Retained austenite calibration blocks .....	40
Figure 4.5. Image of sample under microhardness machine camera .....	42
Figure 4.6. Intergranular oxidation at 1000x, without etching .....	42
Figure 4.7 Penetration depths versus $\sin^2(\psi)$ of ferrite and austenite and different metals radiations [10].....	44
Figure 4.8 Sample dimensions and electropolish location.....	45
Figure 4.9. An example for settings and MBN pattern.....	46
Figure 4.10. Some of the calibration trials as a function of amplification.....	47
Figure 4.11. Example hysteresis curve obtained from Stresstech Rollscan $\mu$ Scan 500-2 .....	47
Figure 5.1. Optical micrographs of the case zones, 1000x, %3 nital etched .....	50
Figure 5.2. SEM micrographs of the case zones.....	51
Figure 5.3. Optical micrographs of the core zones, 1000x, %3 nital etched .....	52
Figure 5.4. SEM micrographs of the core zones.....	53
Figure 5.5. Intergranular oxidation under a scanning electron microscope.....	54
Figure 5.6. XRD pattern of retained austenite measurements of the a) A and B b) A-1 and B-1, showing the effect of carburizing time .....	55
Figure 5.7. XRD pattern of retained austenite measurements of the a) A-1-2, A-2-2 and A-3-2, showing the effect of sub-zero treatment b) A-3-1, A-3-2, and A-3-3, showing the effect of tempering temperature .....	56
Figure 5.8. Effect of sub-zero treatment temperatures on the amount of retained austenite of A-X-1, A-X-2, B-X-1, B-X-2 samples, X denotes 1,2,3.....	58

Figure 5.9. Representative TTT diagram of the A-3-3, calculated by JMatPro, no scale .....	59
Figure 5.10. Hardness depth profiles of the A, A-1, B, B-1, showing the effects of cooling rate .....	60
Figure 5.11. Hardness depth profiles of the A-1-1, A-2-1, A-3-1, showing the effect of sub-zero treatment temperature .....	61
Figure 5.12. Hardness depth profiles of the B-2-1, B-2-2, B-2-3, showing the effect of tempering temperature .....	62
Figure 5.13. Hardness depth profiles of the sample group A .....	63
Figure 5.14. Hardness profiles of the sample group B .....	63
Figure 5.15. Relative RMS voltage versus relative magnetic excitation field data of the group A samples .....	66
Figure 5.16. Relative RMS voltage versus relative magnetic excitation field data of the B and B-2-2 .....	67
Figure 5.17. Relative RMS voltage versus relative magnetic excitation field data of the A-1-2, A-2-2, A-3-2, cryogenic treatment at -25°C, -75°C and -100°C .....	68
Figure 5.18. Relative RMS voltage versus relative magnetic excitation field data for A-2-2 and B-2-2, carburized for 3hours and 6 hours, respectively .....	69
Figure 5.19. Relative RMS voltage versus relative magnetic excitation field data of A-3-1, A-3-2 and A-3-3, untempered, tempered at 150°C and 300°C, respectively .....	69
Figure 5.20. Graph of maximum peak versus RMS, MBN measurements .....	71
Figure 5.21. Variation of MBN-RMS with hardness, group A .....	72
Figure 5.22. Variation of MBN-Maximum peak with hardness, group A .....	72
Figure 5.23. Variation of MBN-RMS with hardness, group B .....	73
Figure 5.24. Variation of MBN-Maximum peak with hardness, group B .....	73
Figure 5.25. Magnetic hysteresis curves of A and B samples, showing the effect of carburizing time.....	75
Figure 5.26. Magnetic hysteresis curves of A and A-1, showing the effect of cooling rate .....	76



Figure 5.27. Magnetic hysteresis curves of B and B-1, showing the effect of cooling rate.....	76
Figure 5.28. Magnetic hysteresis curves of A-2-2, B-2-2, showing the effect of cryogenic and tempering treatment on 3hours and 6hours carburized samples .....	77
Figure 5.29. Magnetic hysteresis curves of A-1, A-1-1, A-2-1, A-3-1, showing the effect of sub-zero treatment temperature .....	78
Figure 5.30. Magnetic hysteresis curves of B-1, B-1-1, B-2-1, B-3-1, showing the effect of sub-zero treatment temperature .....	78
Figure 5.31. Magnetic hysteresis curves of A-1-2, A-2-2, A-3-2, showing the effect of sub-zero treatment temperature .....	79
Figure 5.32. Magnetic hysteresis curves of A-2-1, A-2-2, A-2-3, showing the effect of tempering temperature .....	80
Figure 5.33. Magnetic hysteresis curves of B-2-1, B-2-2, B-2-3, showing the effect of tempering temperature .....	80
Figure 5.34. d-spacing versus $\sin^2(\psi)$ values of the A-3-1 sample .....	82
Figure 5.35. Magnitude of the surface residual stresses of the samples, as heat-treated surface .....	84
Figure 5.36. Magnitude of the surface residual stresses of the samples, after 30 $\mu$ m electropolishing.....	84
Figure 5.37. Residual stress profiles of the A and A-3-1 samples.....	86
Figure 5.38. Graph of the surface residual stresses measured by XRD versus the MBN max. peak height and the hardness values .....	87
Figure A.1. TTT diagram of 9310 steel at initial condition, calculated by JMatPro .....	101
Figure A.2. TTT diagram of 3 hours carburized 9310 steel that surface carbon content reached 0,91wt.%C, calculated by JMatPro.....	101
Figure A.3. TTT diagram of 6 hours carburized 9310 steel that surface carbon content reached 0,97wt.%C, calculated by JMatPro.....	102
Figure B.4. CCT diagram of 9310 steel at initial condition, calculated by JMatPro .....	102

Figure B.5. CCT diagram of 3 hours carburized 9310 steel that surface carbon content reached 0,91wt.%C, calculated by JMatPro .....	103
Figure B.6. CCT diagram of 3 hours carburized 9310 steel that surface carbon content reached 0,97wt.%C, calculated by JMatPro .....	103

## LIST OF ABBREVIATIONS

### ABBREVIATIONS

CCT	Continuous Cooling Transformation
CHD	Case Hardened Depth
EDS	Energy Dispersive X-Ray Spectroscopy
HRC	Rockwell C Hardness
HV	Vickers Hardness
MBN	Magnetic Barkhausen Noise
MP	Magnetoelastic Parameter
N&T	Normalized & Tempered
NDT	Non-Destructive Testing
RMS	Root Mean Square
SEM	Scanning Electron Microscope
TTT	Time-Transformation Temperature
XRD	X-Ray Diffraction

## LIST OF SYMBOLS

### SYMBOLS

$a_c$	Activity of carbon
$B$	Magnetic flux
$B_r$	Remanence
$C_{(z,t)}$	Carbon content at any time and distance from the surface
$C_0$	Initial carbon content of steel
$C_s$	Surface carbon concentration
$D$	Diffusion coefficient [ $m^2/s$ ]
$d$	Distance between diffracting lattice planes [ $\text{\AA}$ ]
$E$	Elastic Modulus [GPa]
$f$	Magnetizing frequency [Hz]
$H$	Applied magnetic field [A/m]
$H_c$	Coercivity [A/m]
$hkl$	Miller indices
$H_s$	Saturation magnetization [A/m]
$M_f$	Martensite finish temperature [ $^{\circ}C$ ]
$M_s$	Martensite start temperature [ $^{\circ}C$ ]
$Q$	Activation energy for diffusion [J/mol]
$V_{PP}$	Magnetizing voltage [Volts]

$\delta$	Penetration depth of Barkhausen noise signal [ $\mu\text{m}$ ]
$\varepsilon$	Elastic strain
$\theta$	Angle between the incident ray and scatter plane
$\lambda$	X-ray wavelength [ $\text{\AA}$ ]
$\mu$	Permeability
$\mu_r$	Relative permeability
$\nu$	Poisson's ratio
$\sigma$	Conductivity of a material under test [ohm]



# CHAPTER 1

## INTRODUCTION

### 1.1 General

Carburizing is a special surface treatment process applied for improving the surface hardness and wear resistance as well as the service life of the engineering components by introducing compressive residual stress at the case. Carburizing steels are generally the members of low carbon low alloy steels, used in specific components including gears, bearings, and bushings where high strength and surface hardness at the case and tough core are required. The process consists of several sub-processes like quenching, cryogenic treatment, and tempering. At the end of each process residual stress state of the component changes. Controlling the residual stress is critical since it can affect all designed properties as well as the product's service life. For example, compressive residual stresses have a positive effect on the component mechanical properties whereas tensile residual stresses lower the mechanical properties that lead part to failure before the designed service life.

Residual stresses can be measured by destructive or non-destructive methods, each method has advantages and limitations. Non-destructive methods are preferred for industrial applications due to their advantages such as non-destructive evaluation of material properties, measurement speed, and control of all products. The X-Ray Diffraction method is widely utilized due to the residual stress measurement accuracy of the technique; however, the analysis of the whole component takes a long time. Therefore, fast and accurate alternative methods are demanded in the industry to increase the production rate. The Magnetic Barkhausen Noise (MBN) method can be an alternative solution to XRD, for residual stress measurements of ferromagnetic materials. But, MBN methods do not give the residual stress directly,

it should be calibrated and correlations should be performed on each type of product and applied process.

## **1.2 Motivation**

Components with high-performance needs such as helicopter transmission systems, landing gears, etc. consist of various types of carburized steel parts designed for heavy-duty missions. Due to heavy working conditions, raw steels are produced with expensive special processes such as VIM-VAR (Vacuum Induction Melting-Vacuum Arc Remelting) and forging. Since the parts have critical characteristics including designed microstructure, case depth, and residual stress state 100% inspection is demanded to guarantee safety. Destructive testing of those features increases the production cost and decreases the production rate due to the long inspection time. Hence, the importance of non-destructive evaluation methods has been increased in the industry.

The MBN method brings several advantages such as non-destructive evaluation ability, fast, reliable results, and suitability for automation. Furthermore, it reduces the need for conventional tests (metallography, hardness, etc.) to inspect microstructure and case depth having long and costly preparation and measurement states. The residual stress measurement by the XRD methods takes a long time and due to the complex geometry of the part destructive sample preparation is required, but the MBN can measure in several seconds without any special sample preparation.



### **1.3 Aim of Study**

This thesis aims to investigate the efficiency of the MBN method for the non-destructive evaluation of the residual stress and microstructure alterations in carburized SAE 9310 steel. For this purpose, MBN measurements were performed on the steel samples prepared by changing carburizing time (3h and 6h), cooling rate (air cooling, oil), sub-zero treatment temperature (-25°C, -75°C, and -100°C) and tempering temperature (150°C and 300°C). Microhardness tests, metallographic investigations, retained austenite and residual stress measurements by the XRD method were also performed on the same samples. Then, the MBN measurement results were compared and correlated with those of conventional characterization methods.



## **CHAPTER 2**

### **THEORY**

#### **2.1 Carburizing**

Carburizing is a heat treatment process that is widely utilized in several industries including aerospace, automotive, and machining. It improves the hardness of the diffusion zone, fatigue life, and as well as the service performance of the components. Thanks to the carburizing, cheap steels that have poor mechanical properties can be utilized and can be selected at the design of the components. There are mainly three types of carburizing according to the carburizing media in other words sources of carbon atoms are pack carburizing, liquid carburizing, and gas carburizing [1].

##### **2.1.1 Pack Carburizing**

Pack carburizing is a procedure in which the components are packed in a box with an external carbon source generally coke and catalyst such as barium carbonate, then heated together for the diffusion process. Furthermore, because of the unpredictable temperature and surface carbon content, acquiring precise case depth and metallurgical features such as carbide network, retained austenite, surface hardness, and also residual stress amount is challenging. Inefficient energy use and adverse environmental effects are two further drawbacks of the process Therefore, that process is no longer widely employed [2].

### 2.1.2 Salt Bath Carburizing

The second method is the salt bath carburizing, in this method liquid is used as carburizing media. The molten salt bath contains sodium cyanide and barium chloride that produce the case depth. Due to the presence of cyanide, it is not environmentally friendly. So, it has limited application in the industry [3].

### 2.1.3 Gas Carburizing

In gas carburizing, the carburizing gas media consists of carbon monoxide, carbon dioxide, methane, and several gases created by the reactions. Gas carburizing is a fast and precise heat treatment process that is also more environmentally friendly carburizing process than others. As a result, gas carburizing is widely employed in a variety of industries such as automotive, aerospace, medical, machining industries, etc. [4].

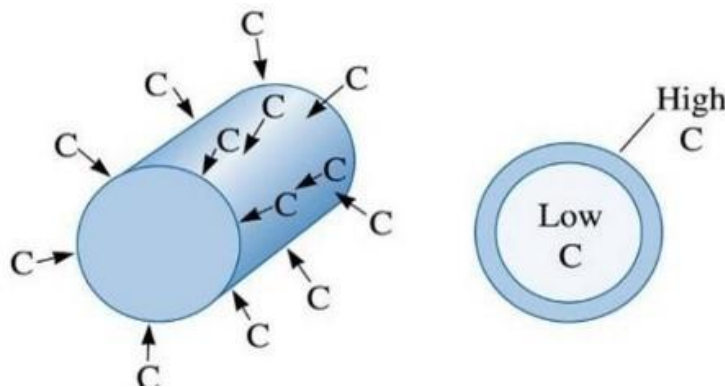


Figure 2.1. Schematic representation of carbon diffusion into steel [4]

The carbon atoms diffuse into the steel substrate according to Fick's Diffusion Laws (Figure 2.1 and 2.2) and can be computed by equation 1.

$$\frac{C(z,t)-C_s}{C_0-C_s} = \text{erf} \left( \frac{z}{2\sqrt{D^*t}} \right) \quad \text{Eq.1}$$

where  $C_{(z,t)}$  is the carbon content in steel at any time and any depth from the surface,  $C_s$  is the carbon content at steel surface,  $C_0$  is the carbon content of the steel at the beginning,  $z$  is the depth from the surface,  $t$  is the time and  $D$  is the diffusion coefficient of the process. Diffusion coefficient highly depends on the process activation energy and temperature,

$$D = D_0 \exp\left(-\frac{Q}{R \cdot T}\right) \quad \text{Eq.2}$$

where  $D_0$  is the pre-exponential temperature-independent coefficient ( $\text{m}^2/\text{s}$ ),  $Q$  is the activation energy for diffusion ( $\text{J/mol}$ ),  $R$  is the gas constant ( $8,314 \text{ J/mol} \cdot \text{K}$ ) and  $T$  is the absolute temperature (in K) [5].

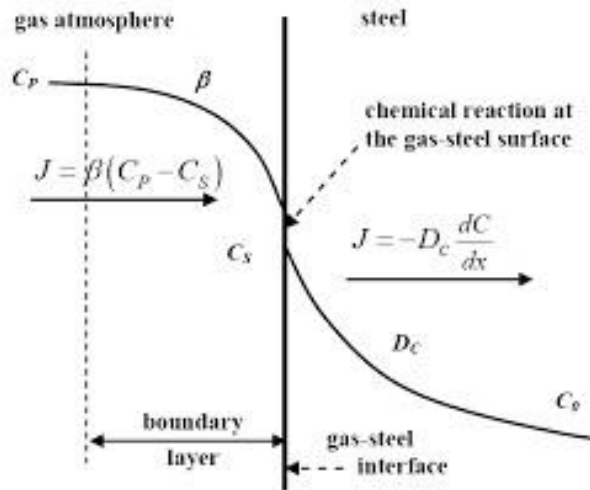
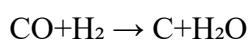
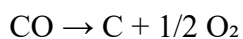
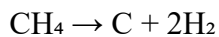
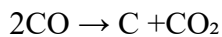


Figure 2.2. Mass transformation of carbon in the gas environment [38]

The gas atmosphere consists of CO, CO<sub>2</sub>, methane, and hydrogen. The reactions that occur inside the furnace and on the steel surface are; [6].



The combination of these reactions generates an equilibrium of carbon in the gas media. The carbon potential acts as a driving force for the diffusion of carbon atoms at the steel surface. If the carbon potential of the furnace atmosphere is more than the carbon content of steel carburizing begins and surface carbon content rises.

Carburizing heat treatment cycle consists of several subprocesses such as austenitizing, carburizing, quenching, cryogenic (sub-zero) treatment, and tempering (Figure 2.3). For the carburizing, the steel is firstly heated to a temperature below austenitizing and then allowed for a period of time to balance the temperature of the steel substrate's surface and core. Since for the heavy batches and thick parts, unbalanced temperature distribution may cause distortion and lower case depth. After pre-heating, the steel is heated to a carburizing temperature of roughly 950°C depending on its chemical composition. Due to the gas reactions inside the furnace, the carbon potential of the furnace increases. At the end of the carburizing process, the part is cooled to room temperature slowly to keep distortion at a minimum degree. The part is then heated to the austenitizing temperature in the same way with pre-heating of carburizing. Although the austenitizing temperature is below that of carburizing, the carbon diffusion continues. At the end of the austenitizing stage, the part is quenched into the oil. The quenching stage is crucial for the hardness profile, microstructure, residual stress state, and distortion.

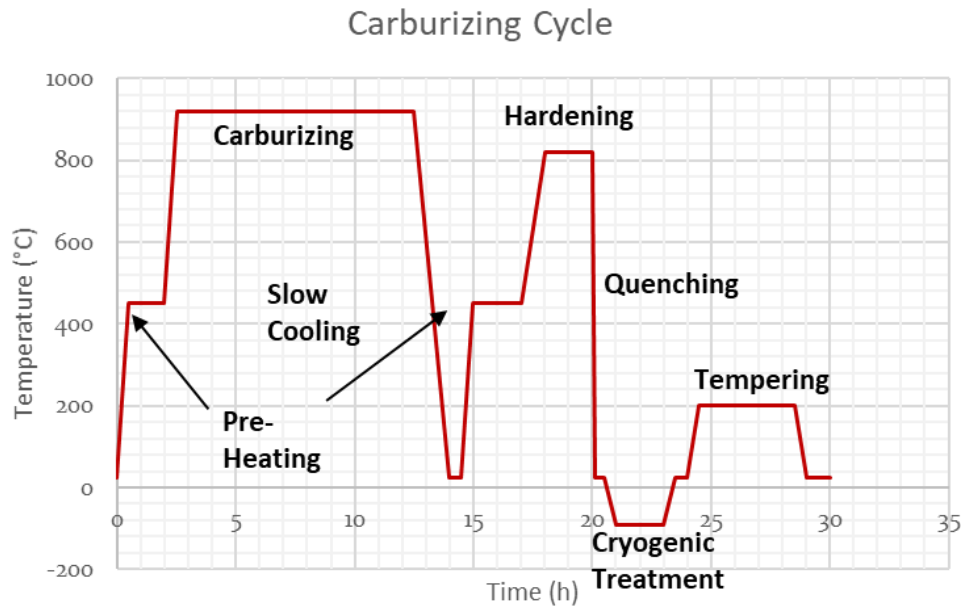


Figure 2.3. The typical carburizing cycle of steels

After quenching the steel contains martensite, and untransformed retained austenite microstructures.

Austenitizing is the heat treatment process the steel parts are heated above  $A_{c3}$  temperature and allowed for a certain time sufficient to produce a homogeneous single austenite phase and temperature distribution at steel surface and core. Depending on the cooling rate different phase transformations occur obeying the CCT diagram [7].

Quenching is a method of rapidly cooling metal to modify mechanical properties and also phase distribution. Brine, water, oils, polymers are examples of quenchants [8]. Cooling rates vary depending on the type of quenchant employed, the temperature of the quenchant, the agitation of the quenchant, and other factors. The quenching process is mainly divided into three stages. They can be named as vapor blanket, nucleation of boiling, and convective cooling stages.

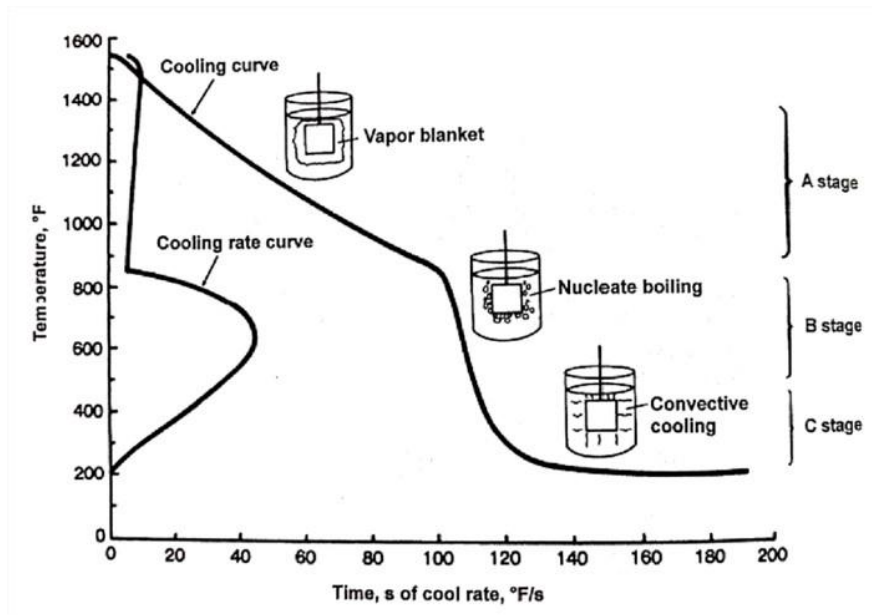


Figure 2.4. Stages of quenching and cooling rate curve [8]

The immersed heated steel in quenchant enters in vapor blanket stage and the metal is surrounded by a blanket vapor. Cooling capacity is low in this stage because of the poor heat transfer capacity of the gas phase and it should last in a fast manner, and agitation plays an important role to get rid of the phase. After passing that, steel enters in boiling nucleation stage. In this stage, the heat removal rate rises to maximum because of the heat of evaporation of quenchant and convective heat transfer. That stage lasts when the metal's temperature falls below the quenchant boiling temperature. And finally, the convective cooling stage is reached, the only active mechanism is the convection. The lowest cooling rate is observed in this stage (Figure 2.4). By playing these cooling rates different phases with different amounts can be obtained such as pearlite, bainite, martensite, and retained austenite.

The amount of retained austenite is determined by the alloying elements but mostly by the carbon content. The temperature of martensite start and finish drop as the carbon content rises (Figure 2.5). Therefore, after a point martensite finish temperature decrease below room temperature even down to sub-zero temperatures.



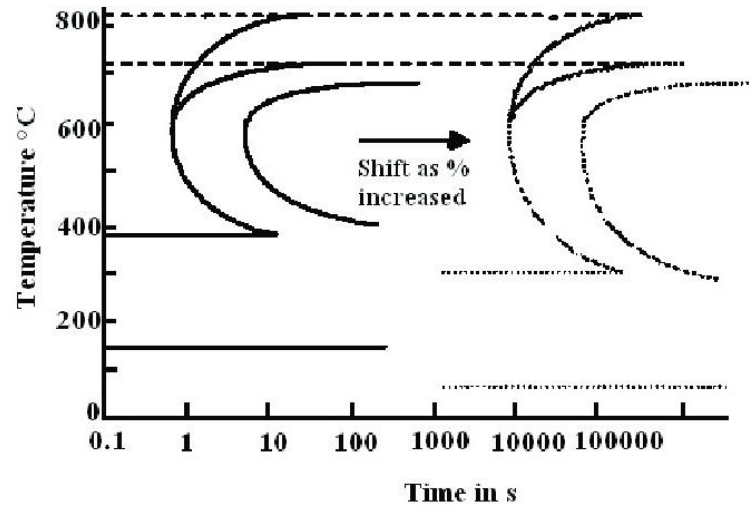


Figure 2.5. Effect of carbon content in steel on TTT diagram [39]

The amount of retained austenite must be minimized. Because retained austenite is unstable at room temperature and during the service of the part, it can be transformed into the martensite phase by deformation-induced transformation. Fresh martensite is a very brittle phase and it will lead part to catastrophic failure. So, to avoid these problems and risks the steel part is subjected to sub-zero treatment for a certain time and treatment temperature depending on the steel type. Finally, the steel part is tempered and converted into tempered martensite which is a more ductile and tougher phase than the martensite. The residual stress condition of the components varies at the end of each process.

## 2.2 Residual Stress: Formation and Relief

*Macherauch and Vöhriger* investigated the residual stress formation depending on the transformation sequence of the core and the case as prior core transformation, and prior case transformation [56]. When the core transformation precedes the case transformation, between core transformation time ( $t_{c,i}$ ) and surface transformation time ( $t_{s,i}$ ) compressive stress is observed at the core and balanced by the tensile stress at the case region. Compressive stress formation is observed in the case after surface transformation time ( $t_{s,i}$ ) (Figure 2.6). When the case transformation precedes the

core transformation, the core of the sample still consists of austenite and is surrounded by an already transformed case. When the core starts to transform with the expansion, compressive stress exists at the core and is balanced by tensile residual stress at the case.

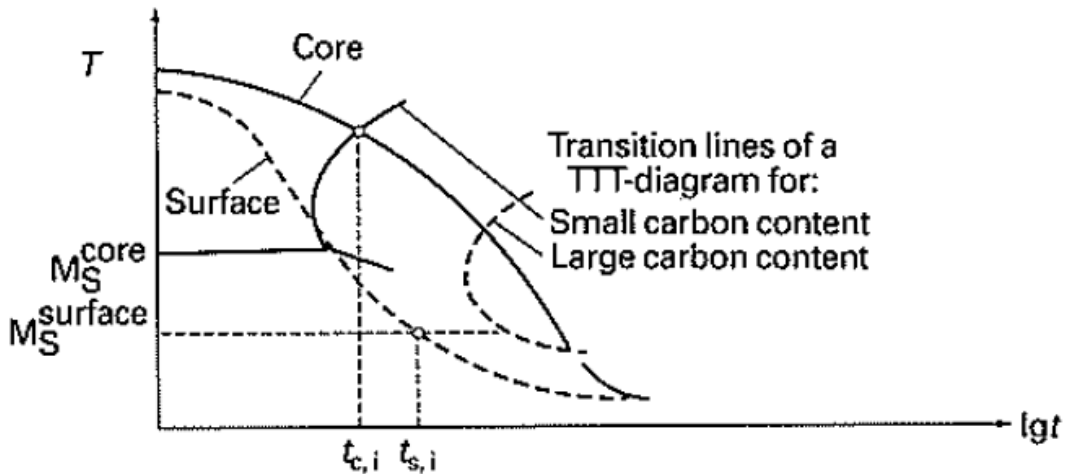


Figure 2.6. Transition line of the case and the core [57]

Since increasing the %wt. C alters TTT and CCT diagrams of the steels by shifting the ferrite and bainite curves to a longer time and decreasing the martensite start ( $M_s$ ) and finish temperatures to lower temperatures, the carbon gradient causes a difference at  $M_s$  temperatures of the case and the core of the components. Since any austenite to martensite transformation causes a volume expansion, initiation of austenite to martensite transformation at the core earlier than the case develops the surface compressive stress [57]. In carburized low alloy steel, the case is the last section of materials that transform into martensite depending on the part shape, and the geometry and most of the time expansion of martensite causes compressive residual stress because the core is already transformed into martensite. However, it must be noted that residual stress formation is highly dependent on the shape and geometry of the material since any alteration at part geometry changes the residual stress formation and the mechanism by affecting the cooling rate and the sequence.

The residual stress state of a component is affected by the post processes including tempering and sub-zero treatment. Since the carburizing lowers the martensite start temperature, the steels contain retained austenite at room temperature, by the action of the sub-zero treatment the retained austenite transforms into martensite. Formation of martensite and carbide rises the compressive stress at the case [43-51]. The tempering operation decreases the residual stress of the carburized steel and as the operating temperature increases the residual stress approach to zero more since the martensite loses its tetragonality by carbide formation [57].

### **2.3 Residual Stress Measurements by XRD Method**

Residual stress can be defined as the elastic stress that exists in a part in the absence of any external loads [9]. It is produced due to the manufacturing processes such as heat treatment, machining, shot peening, and welding. Residual stress has the potential of changing all design parameters as well as the product's service life. For example, for the gears and dynamic parts, compressive residual stress improves the performance and fatigue life of the component by retarding the crack formation. Conversely, tensile stress decreases. It also increases the affinity to stress corrosion cracking. Therefore, control of residual stress is crucial and it should be measured by either destructive or non-destructive methods. Hole Drilling, Curvature, and Layer Removal methods are examples of destructive methods. X-Ray Diffraction, Neutron Diffraction, and Magnetic Barkhausen Noise methods are examples of nondestructive methods.

For the measurement of residual stress from the XRD pattern, the strain amount in the known crystal lattice is utilized. The principles of X-Ray Diffraction can be explained by Bragg's Law [10].

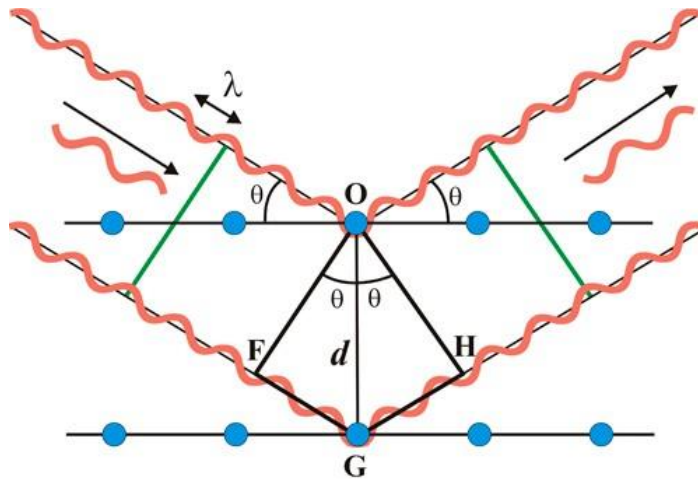


Figure 2.7. Representation of diffraction of X-Rays by a crystal lattice [40]

Incident X-Ray beams are scattered by O and G atoms in different planes and turn into diffracted beams in constructive interference. The incident beam's rays are always in phase and parallel till the top ray collides with the surface atom "O". The lower ray travels an additional path till the atom "G" (Figure 2.7). When two rays go on adjacent and parallel, the additional distance has to be an integral multiple of the wavelength [10]. The difference at two beam's paths can be calculated using the equations 3,4 and 5;

$$|FG| + |GH| = n\lambda \quad \text{Eq.3}$$

$$|FG| + |GH| = d\sin(\theta) + d\sin(\theta) \quad \text{Eq.4}$$

$$n\lambda = 2d\sin(\theta) \quad \text{Eq.5}$$

where; n is an integer,  $\lambda$  is the wavelength of the x-ray, d is the distance between two atomic layers, and  $\theta$  is the angle between the incident ray and the scattering plane.

The presence of stress on a polycrystalline material causes a change in the crystal's lattice parameters which can be observed on XRD data. The peaks at the XRD pattern may shift to a lower or higher angle depending on stress type and broaden [11]. The strain in the crystal lattice can be calculated by equation 6;

$$\varepsilon = \frac{d_n - d_0}{d_0} \quad \text{Eq.6}$$

However, the strain produced by stress not only exists in one direction but also in transverse directions. By assuming as the stress is planar, transverse and longitudinal strains are related with each other by Poisson's ratio.

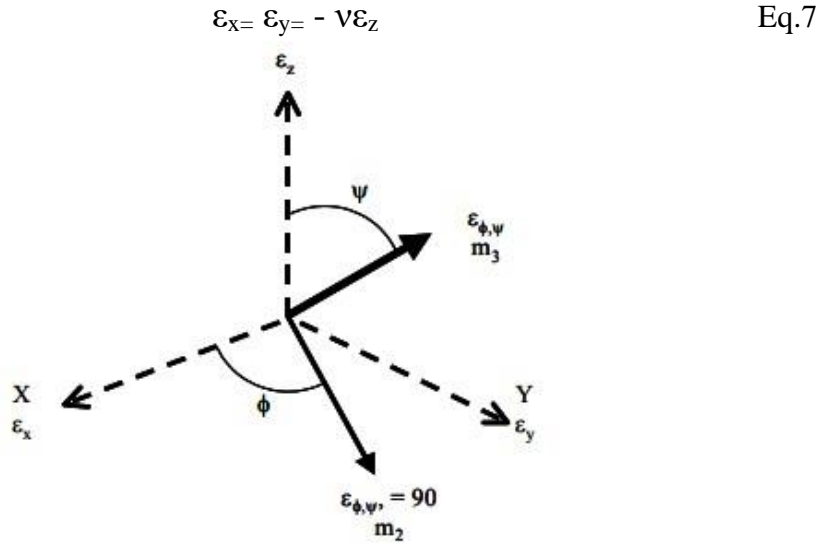
$$\varepsilon_x = \varepsilon_y = -\nu \varepsilon_z \quad \text{Eq.7}$$


Figure 2.8. Principal axes of the strain [10]

Then based on Hooke's Law, the residual stress can be calculated by using equation 8,

$$\sigma = E * \varepsilon \quad \text{Eq.8}$$

where;  $\sigma$  is the stress,  $E$  is the elastic modulus of the material, and  $\varepsilon$  is the strain.

So according to the above equation, the stress can be calculated by equation 9;

$$\sigma = \frac{E}{(1+\nu)\sin^2(\psi)} \left( \frac{d_\psi - d_0}{d_0} \right) \quad \text{Eq.9}$$

where,  $\psi$  is the tilt angle during the XRD measurement (Figure 2.9).

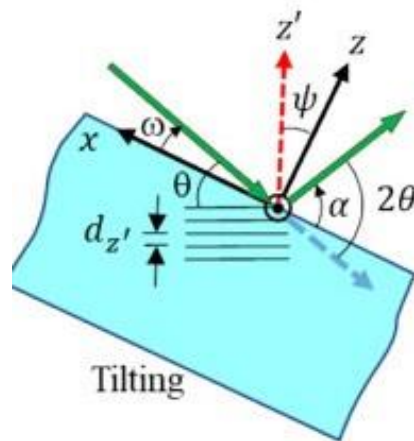


Figure 2.9. Schematic of tilting and angles of XRD [12]

For stress determination by the  $\sin^2(\psi)$  method is commonly used. Measurements are taken at various tilt angles and interplanar spacings are calculated at those angles and a plot is drawn (Figure 2.10).

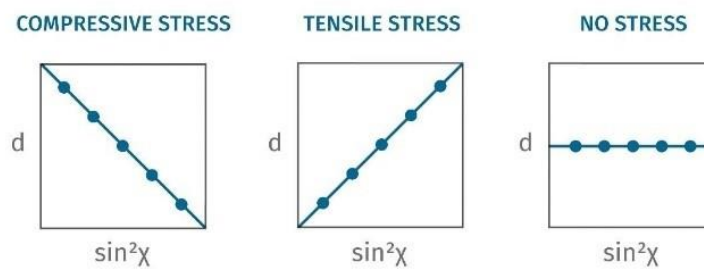


Figure 2.10. Graph of interplanar spacing versus  $\sin^2(\psi)$  [13]

The gradient of the graph can be indicated as “m”. And the equation 9 turns into equation 10,

$$\sigma = \frac{E}{(1+\nu)} m \quad \text{Eq.10}$$

Stress state can be precisely determined by the slope of the interplanar spacing versus  $\sin^2(\psi)$ , if the slope is positive that means the material contains tensile stress, and if the slope is negative the material has compressive stress (Figure 2.10).

## 2.4 Magnetic Barkhausen Noise Method

Ferromagnetic materials are composed of magnetic domains. In the absence of any magnetic field, the domains are in random orientation (Figure 2.11) [52]. However, when a magnetic field is applied, they become ordered in parallel to the magnetic field direction by the domain wall movement. These movements create noise, which was explained in 1919 by Prof. Heinrich Barkhausen. However, the technique caught the attention of researchers and industry at the beginning of the 1980s.

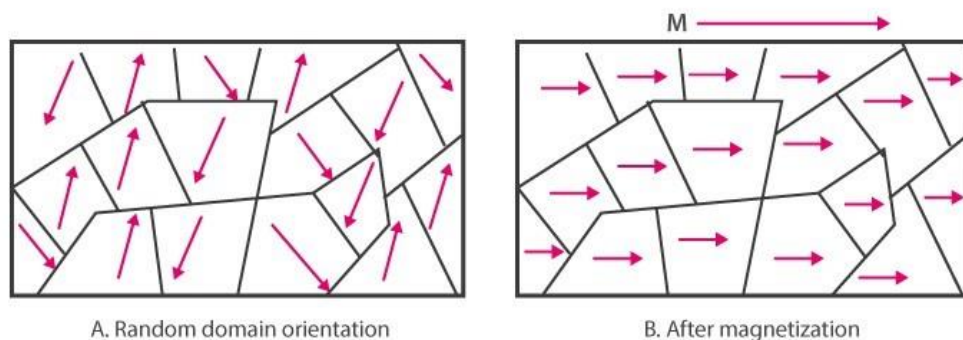


Figure 2.11. Magnetic domains a) random orientation b) aligned in the direction of an applied magnetic field [15]

According to Moorthy *et al*, during the movement of walls, the pinning sites such as grain boundaries, residual stresses, dislocations, second phase particles, and precipitates cause sudden jumps (Figure 2.12) [14]. By the number of changes at the signal levels residual stress states, hardness, carburizing depths, and phase changes can be detected and measured. However, for exactly measuring one of them, other ones should be known to obtain an accurate result.

Applied voltage and frequency are critical for the precision and reliability of the Magnetic Barkhausen Noise (MBN) measurements. Voltage should be set to the most sensitive region at the voltage versus magneto-elastic parameter (MP) diagram (Figure 2.13). For instance, based on such a result the applied voltage should be

around 6V since any difference in microstructure or residual stress manifests itself clearly by giving higher or lower signals from the rest of the material.

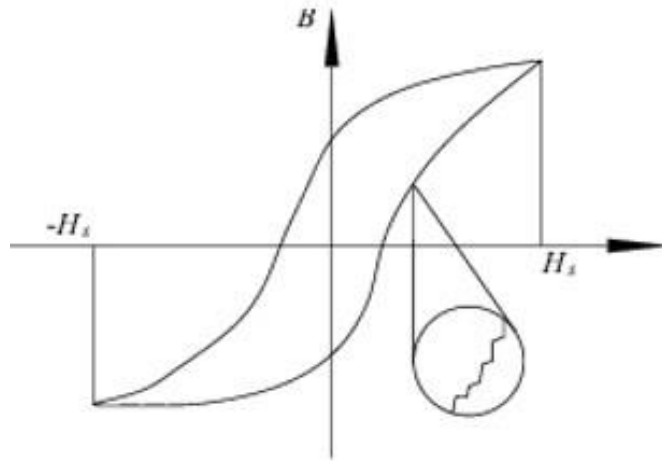


Figure 2.12. Magnetic hysteresis curve and magnetic jumps [16]

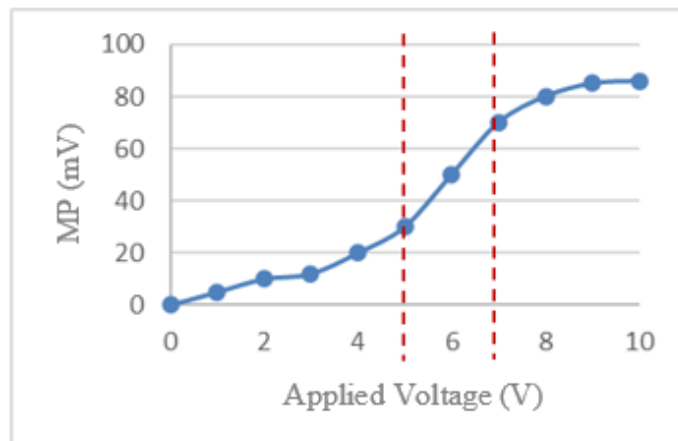


Figure 2.13. Schematic of applied voltage versus Magneto-elastic Parameter (MP)

The magnetizing frequency is another important parameter during the MBN measurements. The penetration depth of investigation depends on frequency, calculated by equation 11.

$$\delta = \frac{1}{\sqrt{\pi\mu\sigma f}} \quad \text{Eq.11}$$



where;  $\delta$  is the penetration depth,  $\mu$  is the magnetic permeability,  $\sigma$  is the electrical conductivity, and  $f$  is the magnetic frequency.

As shown in equation 11, as the frequency increases the penetration depth decreases; conversely, as the frequency decreases the penetration depth increases [17].

Grinding burn inspections can also be done by MBN methods. During the grinding of gears or bearings when high surface hardness, heavy grinding parameters, and insufficient cooling combine the temperature of the ground sample increases. When it passes the tempering temperature of the component, hardness decreases locally on the surface. That is called retempering and it gives a high signal on MBN data (Figure 2.14).

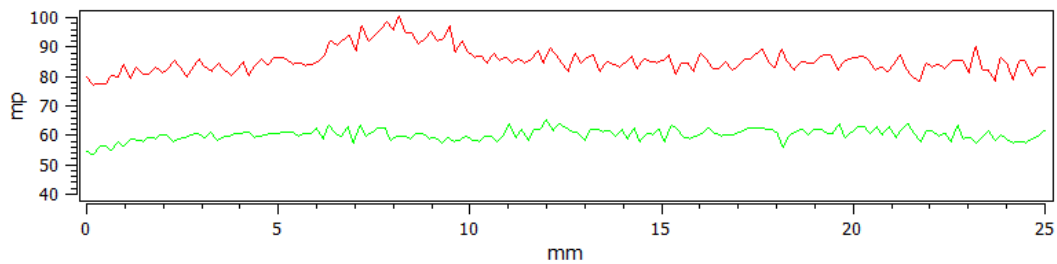


Figure 2.14. Example of MBN results [19]

Local quenching may occur when the surface temperature of the components exceeds the austenitizing temperature and is caused by the action of a cooling fluid. As a result, fresh hard martensite is formed at the surface. It causes low MBN signals at the re-hardened region. The re-hardened zone is surrounded by a softer phase not able to reach austenitizing temperature can be expressed as the heat-affected zone just like in welding.

Soft materials produce high signals while harder phases produce low signals. Also, compressive stress regions give low signals whereas tensile ones give high signals (Figure 2.15).

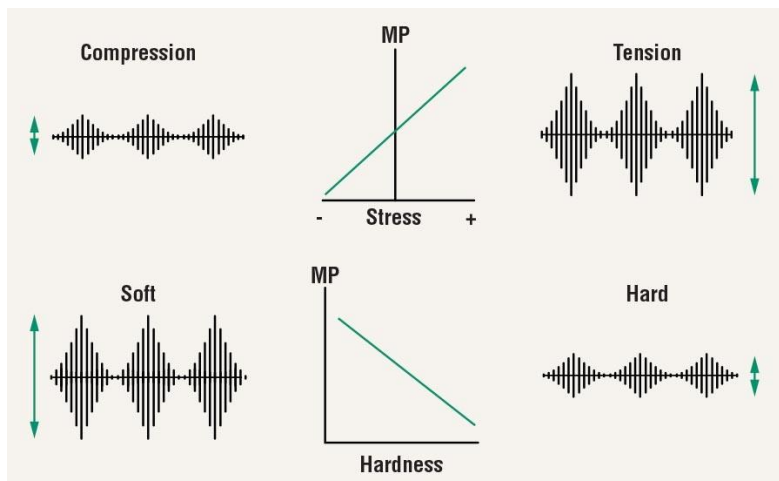


Figure 2.15. MBN patterns of different stress types and hardness values [20]

## 2.5 Retained Austenite Measurement by XRD

Austenite is a steel phase with a Face Centered Cubic (FCC) structure that is stable at high temperatures, as a numeric value for the temperature it can be said to be upon the Ac1 temperature. During the cooling below austenitizing temperature, the austenite phase transforms into ferrite (Body Centered Cubic-BCC) or martensite (Body Centered Tetragonal-BCT) depending on the cooling rate, steel carbon content, and alloying element's amount.

The volume percentage of austenite can be calculated from XRD data since austenite gives peaks at different angles than the other ferrite and martensite. Moreover, ferrite and martensite give nearly identical intensities, with no distinction [21].

For retained austenite measurement by XRD, generally, Cr or Mo is used as the anode material. For example, the Cr tube provides the best resolution of XRD data. And Mo tube produces more peaks than the other tubes.

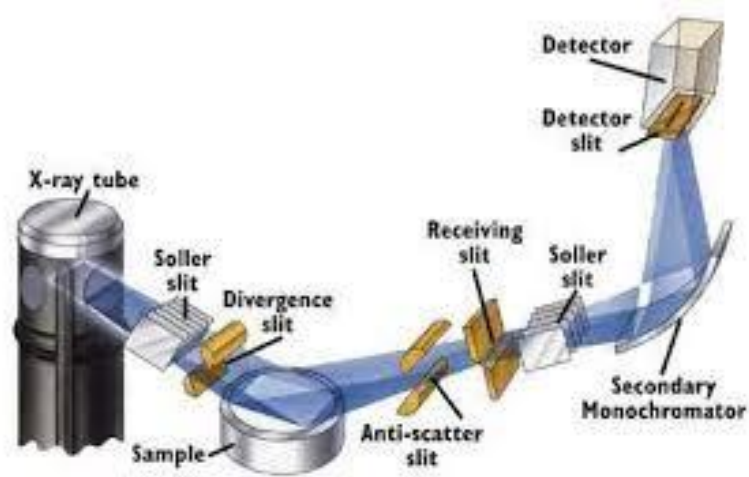


Figure 2.16. Representation of XRD machine [22]

The austenite phase produces peaks at (111), (200), and (220) planes and the ferrite phase produce peaks at (110), (200), and (211) planes. The volume of the austenite phase is calculated from produced peak's intensities by four peak methods, equations 12, and 13.

$$V_{\gamma} = \frac{\frac{1}{q} \sum_{j=1}^q \frac{I_{\gamma j}}{R_{\gamma j}}}{\left[ \left( \frac{1}{p} \sum_{j=1}^p \frac{I_{\alpha p}}{R_{\alpha p}} \right) + \left( \frac{1}{q} \sum_{j=1}^q \frac{I_{\gamma j}}{R_{\gamma j}} \right) \right]} \quad \text{Eq.12}$$

where;  $V_{\gamma}$  is the volumetric amount of austenite,  $I_{\gamma}$  is the intensities of austenite peaks,  $I_{\alpha}$  is the intensities of ferrite peaks,  $R_{\alpha p}$  is the reliability factor and changes for austenite and ferrite.

$$R_{\alpha}^{hkl} = \frac{1/(|F|^2 p L P e^{-2M})}{v^2} \quad \text{Eq.13}$$

where;  $|F|^2$  is the structure factor times its complex conjugate,  $p$  is the multiplicity factor of (hkl) reflection,  $LP$  is Lorentz Polarization factor,  $e^{-2M}$  is the Debye-Waller or temperature factor, and  $v$  is the volume of the unit cell.

The majority of the engineering steel is made up of several alloying elements which create their carbides. They must be eliminated from the value obtained by calculations accurately the amount of retained austenite, equation 14. Carbide amount can be determined by chemical extraction or metallographic methods.

$$V_{\alpha} + V_{\gamma} + V_C = 1 \quad \text{Eq.14}$$

The expected amount of retained austenite (in wt.%) and the level of martensite start, finish temperatures can be calculated by using equations 15 and 16. [25].

$$M_s (\text{°C}) = 520 - 320(\%C) - 50(\%Mn) - 30(\%Cr) - 20(\%(Ni+Mo)) - 5(\%(Cu+Si)) \quad \text{Eq.15}$$

$$\text{Amount of transformed martensite} = 1 - 0,929 * e^{0,00976*(M_s-T)^{1,07}} \quad \text{Eq.16}$$

## CHAPTER 3

### LITERATURE REVIEW

*Buzzetti, Merletti et al.* studied on MBN method to control its reliability and accuracy on gear and feasibility in industrial applications. In industry, nital etch inspection method is used to determine whether ground areas have been over tempered or re-hardened. But, when the grinding is light, it does not provide a clear indication at nital etch while containing different residual stresses. They constructed an experiment plan on carburized AISI 9310 steel gears that were subjected to grinding with various severity levels. The measurements were taken with Stresstech Rollscan 200-1 machine with Viewscan software, and they set the gain as 40 and magnitude to 70 both of them are in arbitrary units. Following the inspections, they were faced with that, gently ground tooth flank produced 30MP and homogeneous MBN profile through the whole tooth. On the other hand, heavily ground teeth flank produced around 150MP and irregular MBN profile. As a result, they stated that MBN is a reliable method for qualitative assessment of residual stress, but for the quantitative method, XRD correlation should be performed to convert the magnetic parameter to MPa directly [29].

*C.C.H.Lo et al.* investigated the dependence of Barkhausen signals on magnetic materials condition using induction hardened steel rods with different case depths. They characterized the case depth of rods by microhardness. Then, by the usage of encircling induction coil magnetic signals were detected. They indicated that all hardened rods gave weak MBN signals at surfaces while getting close to the transition zone, martensite to ferrite/pearlite region, MBN signals were increased due to the lower dislocation density acts as pinning site for domain wall. In addition to that, they calculated their MBN skin depth at 10kHz as 0,29mm for  $\sigma = 5 \times 10^6 \text{ } \Omega\text{m}$  and  $\mu_r = 60$  and the sample had 0,38mm case depth. Therefore, they stated that the MBN signals obtained primarily from a surface layer thinner than the nominal case

depths of hardened rods and so, the MBN signals decrease slightly with case depth [30].

*Anglada-Rivera et. al.* studied the effect of applied stress and grain size on MBN and hysteresis loops. They performed the test with the SAE 1005 steel, heat the samples to 900°C, and cooled them with three different cooling rates for obtaining different grain sizes. They reported that as tensile stress increase obtained MBN voltage increase till a certain point, they named it as critical Barkhausen applied stress. After that point, MBN voltage decreases although the tensile stress reaches higher values. It was explained by domain wall dynamics by the combination of applied stress and magnetic field on motion of domain wall. In addition to that, they also stated that MBN voltage decreases with grain size since fine grains contain more domains and walls than coarse grains [31].

*V.Moorthy et. al.* was focused on the evaluation of the tempering process on MBN measurements in that study. 0,2%wt. C ferritic steel samples were utilized at quenched and tempered conditions, they applied 600°C tempering with different durations starting from 0,5hours to 100hours. They observed that the as-quenched sample showed a single peak but when tempering was carried out, two different peaks were shown, and as tempering time increases peaks become more distinguishable (Figure 3.1).

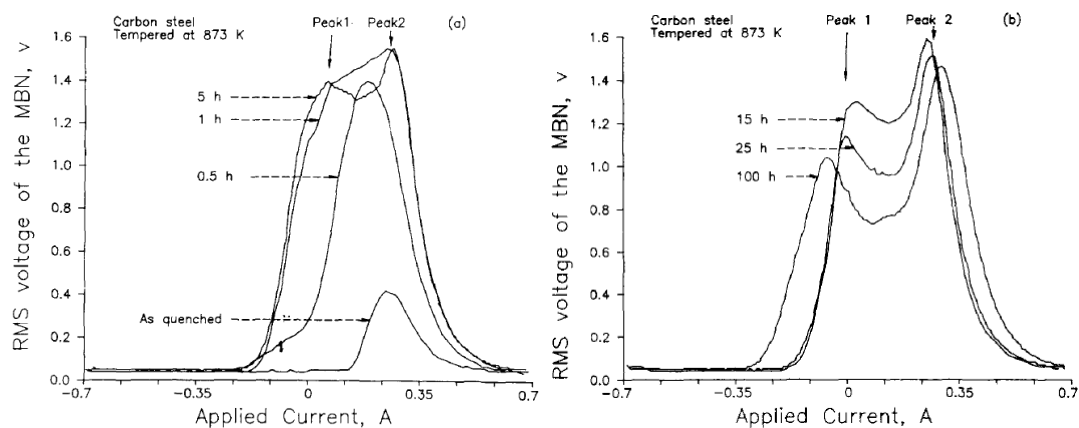


Figure 3.1. RMS voltage obtained by MBN method versus applied current of samples with different tempering time [32]

They stated that the phenomenon occurred due to two reasons they can be regarded as grain boundaries and second phase precipitates since both two of them were the main barriers to domain wall movement. While tempering time increases grain size and carbide size get bigger (Table 3.1). Therefore, at a longer time grain boundary and carbides effect can be observed distinctly [32].

Table 3.1 Sample tempering time and corresponding average grain and carbide size [32]

Sample tempering time (h)	Average size of laths/grains ( $\mu\text{m}$ )	Average size of carbides ( $\mu\text{m}$ )
1	3.74	0.13
5	5.57	0.17
15	8.94	0.26
25	10.65	0.34
100	21.48	0.46

*V.Moorthy, B.A.Shaw and J.T.Evans* studied the relation between hardness changes depending on tempering operation and the MBN method. For that study carburized EN36 steel was used, the samples were carburized and quenched. One group sample was investigated at an as-quenched state (untempered), the other group samples were tempered at 192°C for two hours (stated as standard tempering) and the last group samples were tempered at 250 C for four hours (over tempered). Then hardness testing and MBN measurements were carried out. 125 Hz excitation frequency and 10-2000 kHz filtering were set for MBN measurements of the near-surface region. And for subsurface region analysis, 4 Hz excitation frequency and 2-15 kHz filtering were set. They stated that for near-surface setup, the MBN method gives signals at a mean depth of 100 $\mu\text{m}$ . And subsurface setup gives signals around 500  $\mu\text{m}$ . All three group samples gave a single peak with a near-surface setup and two peaks with the subsurface setup but peak height increases as tempering temperature rises at both setups (Figure 3.2 and 3.3).

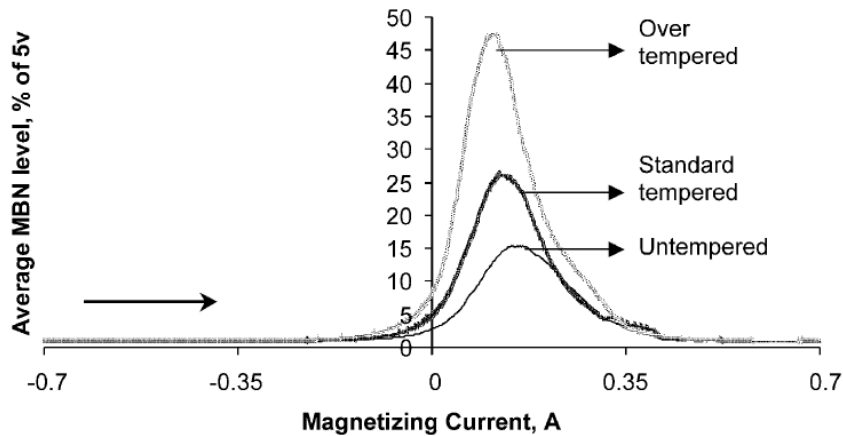


Figure 3.2. MBN pattern of untempered, standard tempered and over tempered samples with 125 Hz frequency [33]

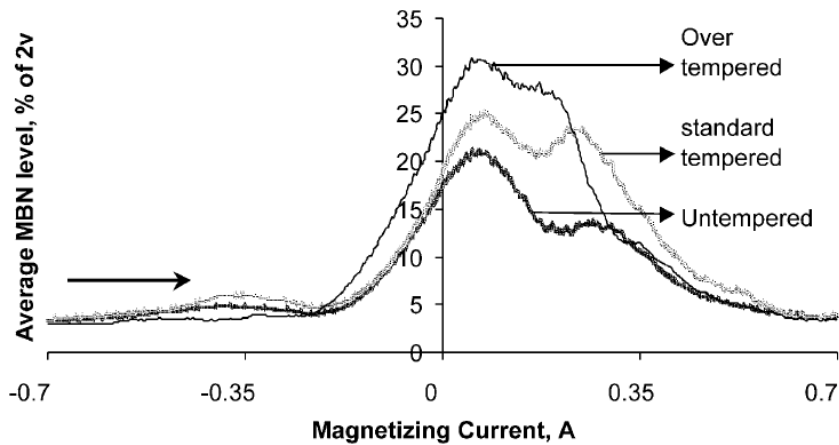


Figure 3.3. MBN pattern of untempered, standard tempered and over tempered samples with 4 Hz frequency [33]

The study demonstrated a good correlation between hardness values and the MBN signals and MBN signals were sensitive to hardness. So, they stated that MBN measurements at higher excitation frequency can be used for surface hardness measurements. Also, low excitation frequency can be utilized to obtain approximate hardness value at the deeper region [33].

*Gür* and *Çam* were focused on the evaluation of microstructure via the MBN method with low alloy SAE 1040 and SAE 4140 steels. To obtain martensite, tempered martensite, fine pearlite-ferrite, and coarse pearlite-ferrite microstructures several



heat treatment processes were carried out. Microstructural control was accomplished initially at SEM and hardness testing (Figure 3.4).

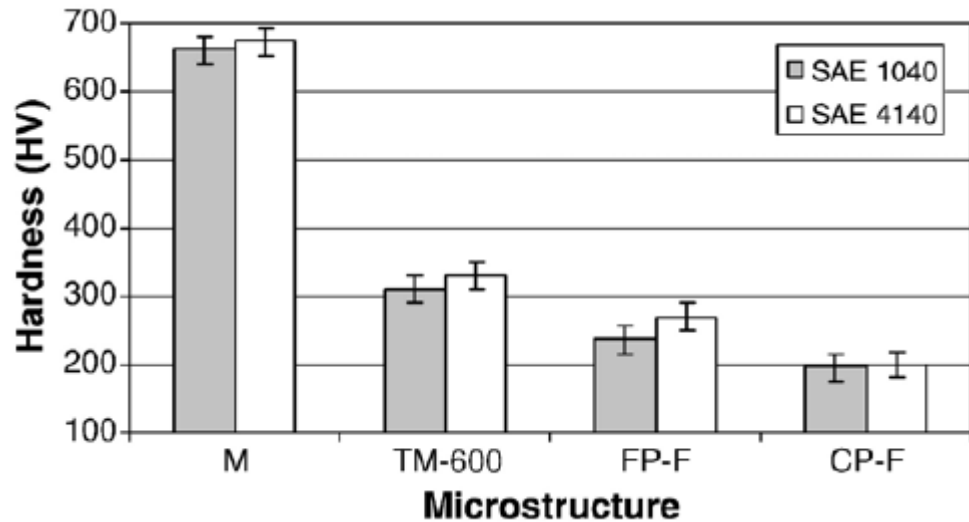


Figure 3.4. Hardness test results of martensite, tempered martensite, fine pearlite-ferrite and coarse pearlite-ferrite structures for SAE 1040 and SAE 4140 [34]

The MBN measurements were taken at Rollscan/ $\mu$ scan 500-2 device with 125 Hz excitation frequency, 20 amplification, and gain to generate the smooth sinusoidal wave. According to them, the lowest MP values were measured at the as-quenched samples, and MBN emission increased in the order of tempered martensite, fine pearlite-ferrite, and coarse pearlite-ferrite (Figure 3.5). For instance, tempered martensite had a higher MP voltage than the as-quenched martensite samples. It was explained with the domain nucleation due to tempering application. In addition to that, the ferrite phase gets coarser, and average domain wall sizes increase. Resistance to domain wall motion and nucleation decreases, so MBN signals were amplified to higher values.

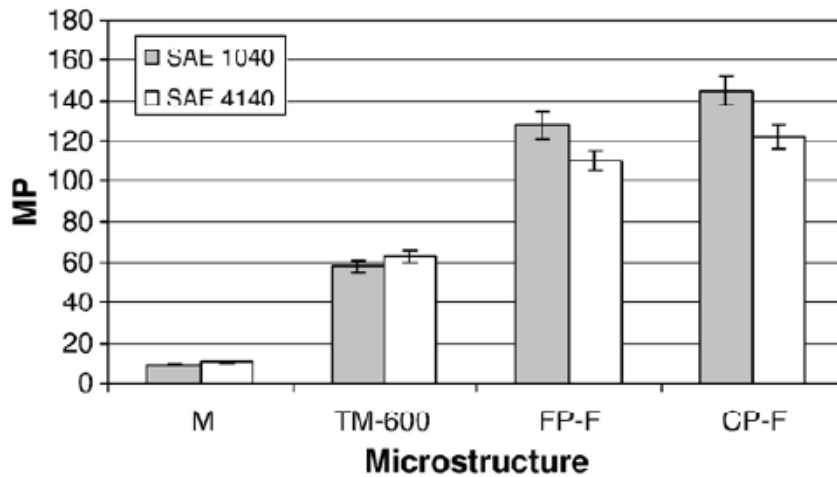


Figure 3.5. Magnetoelastic parameter measured at MBN method of martensite, tempered martensite, fine pearlite-ferrite and coarse pearlite-ferrite structures for SAE 1040 and SAE 4140 [34]

As a result, they stated that the MBN method is sensitive to microstructural change and may be a useful tool for analyzing the microstructure of ferromagnetic components during manufacturing and service [34].

*Arslan et al.* used the MBN method to examine the microstructural analysis of AISI D2 steel. Six different austenitization temperatures within 900°C -1150°C were used to obtain different retained austenite, martensite, and carbide distributions. After the production of samples, hardness tests and metallographic investigations were carried out using an optical microscope and SEM. Then MBN measurements were performed with Rollscan/ $\mu$ scan 600 device with 250Hz excitation frequency and 10-1000kHz band-pass filter setup. Hardness values of samples increases as the austenitization temperature rises (Figure 3.6).

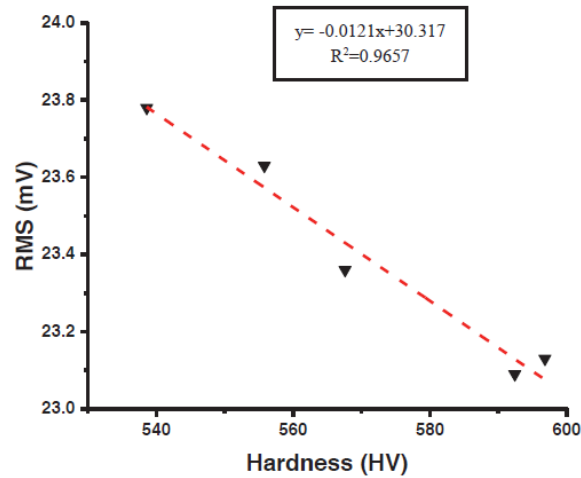


Figure 3.6. Hardness values versus corresponding RMS values of MBN signals [35]

While hardness values increase, the RMS of MBN signals decrease. They stated that the MBN method strongly depends on microstructure and hardness values even the slightest variation [35].

Davut and Gür focused on the characterization of quenched and tempered SAE 5140 steel microstructures via the MBN method. Quenched samples were tempered ranging from 200°C to 600°C and MBN measurements were carried out at Rollscan,µScan 500-2 device. In addition to the MBN method, hardness testing and microstructural analysis under SEM were performed. They claimed that MBN results were affected by tempering temperature due to changes in dislocation density, lattice straining, phase distribution, and hardness of the material. As tempering temperature increases peak height of measurements also increases. According to the study, tempering up to 300°C rises peak height slightly however, after 400°C increments at peak height was found higher. They explain that with the  $\epsilon$ -carbide formation at 200°C and 300°C microstructural alteration was little. So, the peak of MBN does not alter significantly. After 400°C transformations of  $\epsilon$ -carbide to cementite took place and dislocation density decreased. It resulted in ease of magnetic domain wall movement and increase at peak height. In addition to that, they stated that there is a

linear relation between hardness and the RMS value of MBN. Reduction in hardness increased RMS voltages [36].

According to several studies, Gür stated that continuously increasing magnetic field increases the size of domains parallel or nearly parallel while annihilating the other domain orientations on ferromagnetic materials. And the application of alternating magnetic field produces characteristic hysteresis curves and varying properties can be observed on those curves such as saturation magnetization, coercivity, remanence, and permeability. He stated that remanence is sensitive to the structure of the material and dislocation density, an increase in dislocation density may result in a decrease in remanence. Coercivity is primarily related to the microstructure of materials and so, it may be utilized to characterize microstructures. Additively, the presence and distribution of dislocations increase the coercivity. Studies also showed that hysteresis loops obtained via the MBN method cannot be shown as the true curves of the materials since actual values were far beyond the values measured at the MBN method [37].

*Yan et al.* aimed to investigate the effect of cryogenic treatment on microstructure and mechanical properties of carburized 20Cr2Ni4A and 17Cr2Ni2MoVNb steels. All test specimens were carburized at 930°C for 6,7 hours and underwent subcritical annealing at 620°C for 4 hours. Then the specimens were austenitized and quenched into the oil. Tempering operation at 150°C for 2 hours was applied to one group sample, for the other group sub-zero treatment at -196°C for 1 hour was applied before tempering. Microstructural investigations were carried out by XRD, optical and scanning electron microscopes, and microhardness measurements were performed with the Vickers method. They reported that sub-zero treatment had a significant effect on retained austenite content at the surface, it was decreased from 13,1 to 9,6 for the 20Cr2Ni4A specimens, and from 19,2 to 9,5 for the 17Cr2Ni2MoVNb. In addition, the surface hardness values of sub-zero treated specimens were higher than the quenched and tempered specimens for both steel groups, 122HV for the 17Cr2Ni2MoVNb and 34HV for the 20Cr2Ni4A specimens. Furthermore, they said that the surface microstructures of both steel groups consist

of high carbon needles like tempered martensite, spherical carbide, and retained austenite, sub-zero treated specimens contained more dispersed and fine carbides than the quenched specimens [41].

*Prieto et al.* studied the effect of sub-zero treatment on the fracture toughness of AISI 420 steel. Two groups of test specimens were produced, one group of specimens were quenched into oil from 1030°C, and tempered at 410°C for 10 minutes. Other group specimens were sub-zero treated at -196°C for two hours after quenching and tempered at 410°C for 10 minutes. Plane-strain fracture tests, hardness tests were performed and microstructural correlations were made by SEM and XRD. Test results indicated that carbide refinement was observed at the sub-zero treated part led to an increase in 5% hardness and 30% fracture toughness [42].



## CHAPTER 4

### EXPERIMENTAL PROCEDURE

#### 4.1 Material and Sample Preparation

As samples, SAE 9310 (AMS 6265N) steel was used (Table 4.1). Due to its superior hardenability high case hardness values and excellent core toughness can be obtained after carburizing operations. Because of these features, this steel is a powerful candidate for heavy-duty applications such as transmission gears, pistons, and boring bars.

Table 4.1 Chemical composition of SAE 9310 (AMS 6265N) standard and the steel used

Element	Min. (according to standards)	Max. (according to standards)	The steel used in the thesis
C	0,070	0,130	0,100
Si	0,150	0,350	0,260
Mn	0,400	0,700	0,530
P	-	0,015	0,005
S	-	0,015	<0,0009
Cr	1,000	1,400	1,320
Mo	0,080	0,150	0,100
Ni	3,000	3,500	3,170
Cu	-	0,350	0,050
B	-	0,001	<0,0005

VIM-VAR (Vacuum Induction Melting – Vacuum Arc Remelting) process was also applied to the steel stock by the manufacturer. It improves the cleanness degree of

the steel by reducing the amounts of impurities and discontinuities, allowing for higher strength and toughness.

To eliminate the effects of the steelmaking process, all specimens were prepared from the same rod (200mm diameter and 100mm height) by wire erosion (Figure 4.1).



Figure 4.1. Some of the manufactured specimens

The incoming steel was in Normalized and Tempered condition. Its microstructure consists of ferrite and dispersed carbide particles, with an average hardness of around 215HV (Figure 4.2).



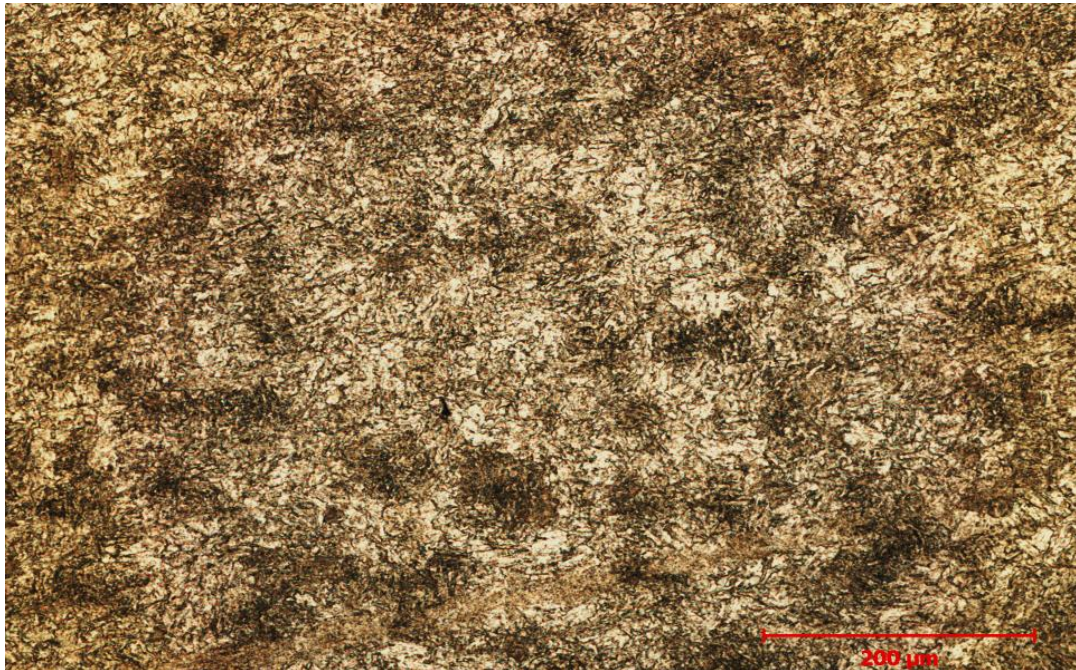


Figure 4.2. Microstructure of incoming material, 200x

After wire erosion, the diameters of samples were reduced to 35mm and cut into 15mm height by an industrial saw. Heat is generated during the wire erosion machine, in order to remove the heat-affected zone, a turning operation was performed on the samples into the sizes of 30mm diameter and 14mm height. The pre-hardening operation was applied to all samples in one batch in an atmosphere-controlled furnace to obtain homogenous grain size (5 or finer per ASTM E112) and uniform microstructure (Figure 4.3) [46].



Figure 4.3. A representative microstructure after pre-hardening, 200x

The operation was carried out at 820°C for 2 hours in an atmosphere-controlled furnace at the carbon potential of 0,2 wt.%C and then quenched in oil at 90°C. Tempering operation was applied subsequently at 540°C for 3 hours in an inert nitrogen atmosphere. After pre-hardening and tempering operations, low carbon martensite was obtained, having a hardness in between 252HV and 260HV. Scale formation was observed after quenching in oil and tempering at high temperatures. In addition, the furnace atmosphere was regulated by endogas flow. The surface chemistry of the samples was changed due to the slight fluctuation of the input gas content and non-decreasing below 0,2 wt.% C in the atmosphere. To eliminate any negative effects, the samples were ground about 0,5mm on. Finally, 30mm diameter 13mm height cylindrical samples were obtained. The grinding operation also decreased the surface roughness of the samples.

## 4.2 Heat Treatment Processes

Carburizing heat treatments commenced shortly after the sample manufacturing. Recommended AGMA standards call for a carburizing temperature of 925°C. The process sequence started with pre-heating at 450°C for 90 minutes to obtain a homogeneous temperature distribution throughout the whole sample. If the samples are loaded into the carburizing furnace at the ambient temperature, the case and core section of the samples reach the carburizing temperature at different times. This may result in considerable thermal stress and distortion. The pre-heating stage minimizes that issue. The batch was instantly loaded into the carburizing furnace for the next step. After completing the carburizing recipe, the batch was either immersed in an oil bath or cooled in air. Then, the final stages were cryogenic treatment and tempering.

The carburizing operations were carried out as follows: the carbon potential at the carburizing stage was set to 1.15 wt.%C, and the quenching oil temperature and oil agitation speed were set to 90°C and 50%, respectively. They were the experiment's constant parameters. As variables, two carburizing times were selected as 3 hours or 6 hours at 925°C. Two cooling rates were applied: quenching, or air-cooling. Three sub-zero temperatures were chosen: -25, -75, or -100°C. And finally, two tempering temperatures were selected as 150, or 300 °C.

In total, 8 carburizing batches were prepared, yielding 22 samples. To ensure repeatability and increase confidence, the samples were created with their back-ups (Table 4.2).

Table 4.2 Sample identification according to their process routes

Test Sample	Carburizing No#	Sub-Zero Treatment #	Tempering #
A	C1 (Air-cooled)	N/A	N/A
A-1	C1	N/A	N/A
A-1-1	C1	S1	N/A
A-1-2	C1	S1	T1
A-1-3	C1	S1	T2
A-2-1	C1	S2	N/A
A-2-2	C1	S2	T1
A-2-3	C1	S2	T2
A-3-1	C1	S3	N/A
A-3-2	C1	S3	T1
A-3-3	C1	S3	T2
B	C2 (Air-cooled)	N/A	N/A
B-1	C2	N/A	N/A
B-1-1	C2	S1	N/A
B-1-2	C2	S1	T1
B-1-3	C2	S1	T2
B-2-1	C2	S2	N/A
B-2-2	C2	S2	T1
B-2-3	C2	S2	T2
B-3-1	C2	S3	N/A
B-3-2	C2	S3	T1
B-3-3	C2	S3	T2

<b><u>Designation</u></b>		
C1	Carburizing 1	925°C / 180min. Cp:1,15
C2	Carburizing 2	925°C / 360min. Cp:1,15
S1	Sub-Zero Treatment 1	-25°C / 120min.
S2	Sub-Zero Treatment 2	-75°C / 120min.
S3	Sub-Zero Treatment 3	-100°C / 120min.
T1	Tempering 1	150°C / 120min.
T2	Tempering 2	300°C / 120min.

TUS (Temperature Uniformity Survey) and SAT (System Accuracy Test) calibrations of the furnaces are performed periodically per AMS2750 and the furnaces have  $\pm 6^{\circ}\text{C}$  tolerance [54]. By the SCADA systems temperature uniformity, the gas content of the atmosphere, etc. can be monitored instantly.

### 4.3 Microstructural Investigation

The samples were metallographically prepared at ATM Saphir 550 grinding and polishing machine with the following recipe given in Table 4.3 after embedding into Bakelite.

Table 4.3 Sample preparation recipe for metallographic examination

#	Grinding & Polishing Disc	Suspension	Operation
1	Aka-Piatto 220	N/A	Coarse Grinding (75 $\mu\text{m}$ )
2	Aka-Allegran 3	N/A	Fine Grinding (9 - 3 $\mu\text{m}$ )
3	Aka-Ramda	DiaMaxx Poly 6 $\mu\text{m}$	Polishing (6 $\mu\text{m}$ )
4	Aka- Napal	DiaMaxx Poly 1 $\mu\text{m}$	Polishing (1 - 0,025 $\mu\text{m}$ )

Then, the samples were etched with 2% nital and examined under Nikon ECLIPSE LV150N optical microscope at magnifications of 50x, 200x, 500x, and 1000x. In addition to optical microscope, scanning electron microscope was also utilized via Nova Nanosem430 device.

### 4.4 Retained Austenite Measurement

Retained austenite measurements were taken on the GNR Arex D machine which uses a Mo X-Ray source and Zr filter. The angles between  $21,5^{\circ}$  and  $44,0^{\circ}$  were scanned in 120 seconds per sample by applying 50kV voltage and 20mA current.

Before the measurements the machine was calibrated with a calibration block that contain 5,3%, 10,3%, 15,7%, 20,1%, and 25,6% retained austenite to increase the accuracy of the measurements (Figure 4.4).



Figure 4.4. Retained austenite calibration blocks

The retained austenite measurement results are influenced by sample preparation and surface quality in the same way that other non-destructive testing methods are. To obtain accurate data, heat treatment residue and scale should be gently removed from the surface. Electropolishing is one of the better options for such an application. Because other methods of material removal or surface preparation, such as grinding, sanding, dry blasting, and so on, may result in the transformation of retained austenite due to the high instability of the related phase. As a result, an electropolishing operation was carried out, and measurements were taken 30m below the surface.

Since C-content directly affects the martensite start and finish temperatures, and thus the amount of retained- $\gamma$ , the phase transition temperatures were calculated for the maximum carbon contents at the surface achieved after carburizing (Table4.4)

Table 4.4 The phase transition temperatures of samples, calculated by JMatPro, based on the carbon content at the surface

Transitions	Initial (0,10 wt.%C) °C	3 Hours Carburized (0,91 wt.%C) °C	6 Hours Carburized (0,97 wt.%C) °C
Pearlite	690,6	705,3	704,5
Bainite	549,8	353,8	339,2
Ferrite	763,2	662,3	656,6
Martensite Start	381,5	103,5	83,5
Martensite %50	347,7	58,9	37,6
Martensite %90	269,1	-44,8	-68,9

#### 4.5 Hardness Measurements

The samples were measured by a microhardness testing machine, QNESS Q30. Case depth measurements were taken using a microhardness test machine with the HV0,5 method and a 50µm increment between testing points towards to core from the case per ASTM E92 and ASTM E384. Each measurement line had 30 indentation points and at the horizontal axis, case to the core axis, the distance between the two points was 50µm. For the vertical axis that distance was 100µm with the zigzag pattern, by this mean indentation points separated from each other. This is significant since as indentations get closer after a certain distance, they begin to affect each other, depending on the hardness measurement method and material in other words the indentation size. Three parallel measurement lines were inserted into the cross-section of each sample. The first indentations were performed 70µm beneath the surface (Figure 4.5).

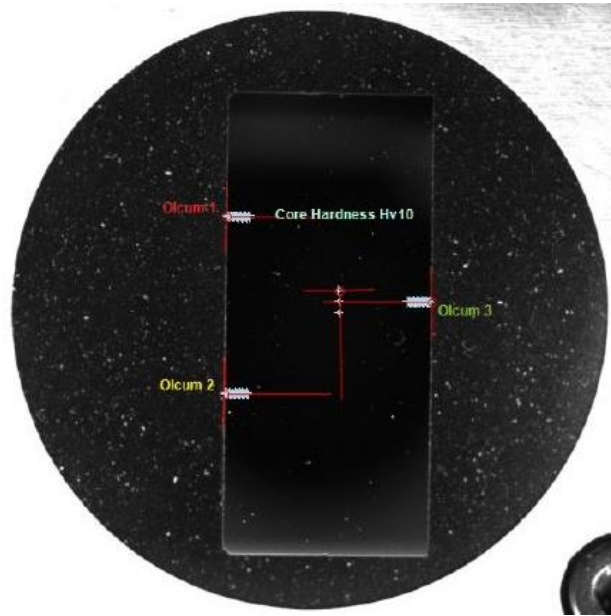


Figure 4.5. Image of sample under microhardness machine camera

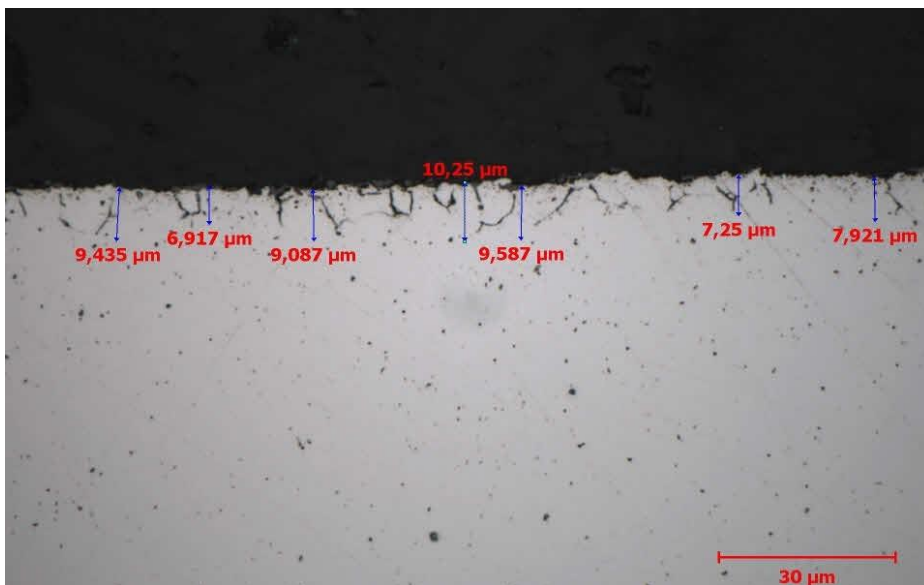


Figure 4.6. Intergranular oxidation at 1000x, without etching

At the surface of the carburized samples, there was an intergranular oxidation layer with an approximately 10  $\mu\text{m}$  thickness from the carburizing cycle (Figure 4.6). Surface hardness, total carburizing depth, and effective case depth information were interpreted after the hardness profile of the samples have been obtained. The total



case depth is the highest distance of the carbon diffusion from the surface. In AGMA B923-B05, the effective case depth is defined as the depth at which 50 HRC hardness is measured [26]. In addition to the case depth measurements, hardness measurements were also performed at the center of the samples.

#### 4.6 Residual Stress Measurement

Stresstech Xstress G2R system having Chromium X-Ray source and Vanadium filter was used. Before measuring residual stress, % retained austenite was measured. In the presence of a secondary phase, residual stress measurement should be performed on the secondary phase too, since it also accommodates residual stress [27]. For the system used the recommended approximate two theta angle for the (211) ferrite peak is  $156.1^\circ$  and for the (220) austenite peak is  $128.8^\circ$  [10]. Since the samples contain both martensite and austenite, measurements were performed by considering those angles. The residual stress measurements were taken with three different phi angles ( $\varphi$ ) as  $0^\circ$ ,  $45^\circ$ , and  $90^\circ$ .

To construct a reliable and accurate  $d$  versus  $\sin^2 X$  graph, measurements were carried out at fifteen tilt angles, that contain seven positives, seven negatives, and zero degrees. The XRD method gives the residual strain amount directly, then with the usage of strain, stress values were calculated. However, for the calculation, some assumptions have to be made such as  $\sigma_{33}$  accepted as zero (i.e., biaxial stress), and the slope of the fitting of  $d$  versus  $\sin^2 x$  graph is used. During the measurements, shear stresses were left as unknown and the normal residual stresses were considered [58]. In addition, the unstrained lattice parameter,  $d_0$ , should be known. The calculation of each  $d_0$  value for each sample is difficult since this parameter is measured from the powder, so a sufficient amount of powder should be obtained with constant carbon content. However, in the case of carburizing, carbon content decreases gradually from the case to core, making it difficult to form powder with the same carbon content. But, according to Murray and Noyan, because  $d_0$  is a multiplier at the formula, the elastic strain at the maximum level would be less than

2%, so  $d_0$  can be accepted as the lattice strain at a zero-degree tilt,  $d_x=0$  [28]. They stated that the error would be less than 2%. Therefore, during the conversion of strain to stress the  $d_0$  values were accepted as the stress at zero tilt angle. To calculate the stress, two mechanical properties of the samples, Elastic modulus, and Poisson's ratio, must be known. For the ferrite, they were taken into account as 211 GPa and 0,3 respectively, and 196 GPa and 0,28 for the austenite.

*Fitzpatrick et al.* stated that the majority of the metallic materials strongly absorb X-Rays and as a consequence intensity of the incident beam reduced in a very short distance below the surface (Figure 4.7) [10]. The XRD residual stress measurements were performed via Cr anode and corresponding penetration depth vary ranging in 3-6 $\mu\text{m}$  for both ferrite and austenite.

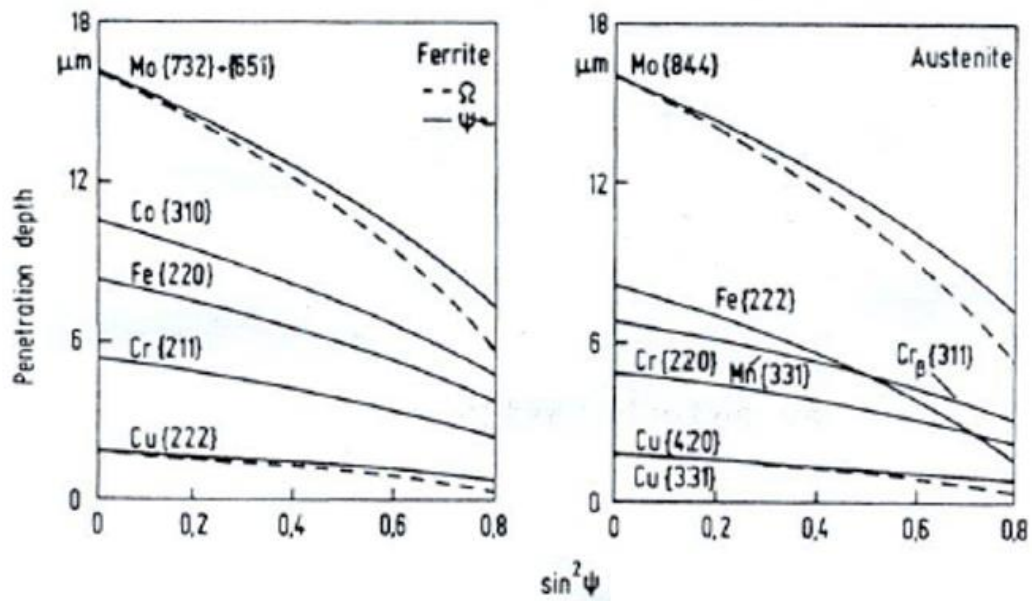


Figure 4.7 Penetration depths versus  $\sin^2(\psi)$  of ferrite and austenite and different metals radiations [10]

After completing stress measurements at the surfaces, depth profile analysis began for the selected samples. Depth profile analyzes were planned to get data at 10,50,100,200,400 and 600 $\mu\text{m}$ . To minimize stress relaxation during material

removal the electropolishing method was applied to the center of samples with  $\varnothing$  10mm using Struers A2 electrolyte at Struers Movipol electropolishing machine.

The MBN measurements and residual stress measurements via XRD methods are the part, and the geometry dependent, the performed measurements are valid for that setup. Therefore, any change in the part geometry changes the test results. Also, the residual stress measurements were performed after 30 $\mu$ m electropolishing at the center of the specimens, any measurements at different locations such as radial surface may give different results than the flat surface measurements (Figure 4.8).

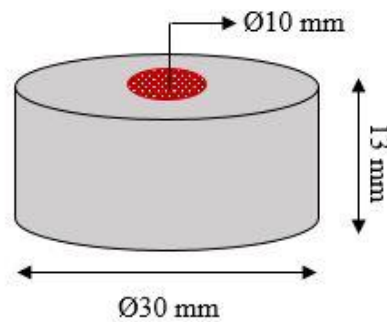


Figure 4.8 Sample dimensions and electropolish location

Quenching oil film, heat treatment residue and intergranular oxides exist at the surface of specimens. Since the penetration depth of the method is around 5 $\mu$ m with the experiment setup, they affect the residual stress measurement, electropolishing is advised at the sample preparation step [55].

#### 4.7 Magnetic Barkhausen Noise Measurements

Magnetic Barkhausen Noise (MBN) measurements were performed by Stresstech Rollscan  $\mu$ Scan 500-2 equipment with 10V magnetizing voltage, 125Hz excitation frequency. In addition, a filter was applied to obtain a smooth MBN curve between 10 to 1000kHz and the number of bursts was set to 18 (Figure 4.9). The probe has two sensors Rollscan and  $\mu$ Scan, such that MBN pattern with magnetoelastic

parameter and hysteresis curve can be obtained with a single run, and the distance between poles of the probe is 3mm.

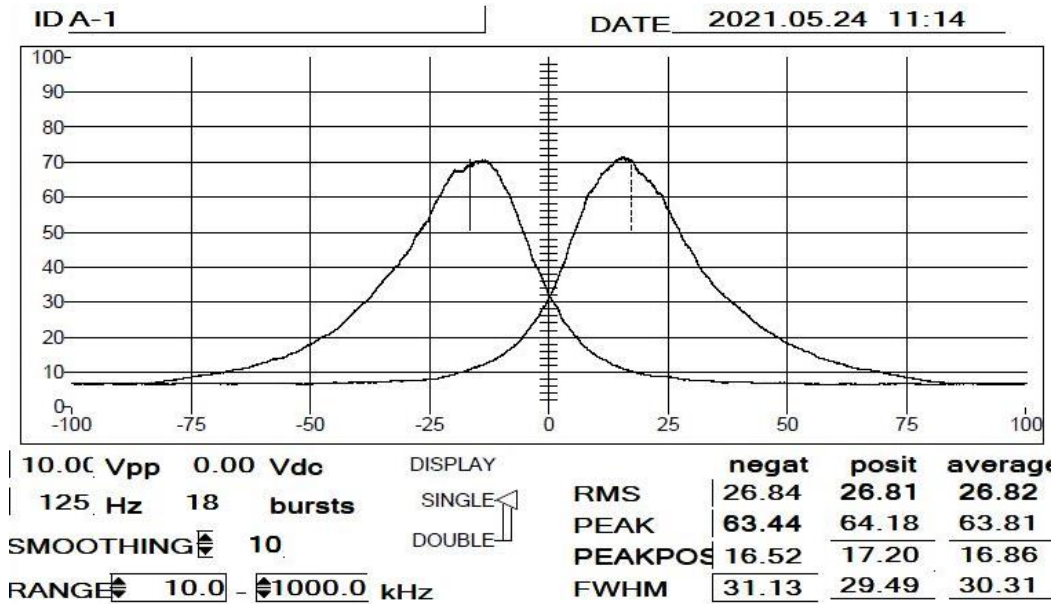


Figure 4.9. An example for settings and MBN pattern

The gain should be amplified to obtain smooth sine-waveform excitation for accurate measurements. Calibration of the equipment before the measurements are quite important, so the calibration was made with the non-carburized sample (pre-hardened state) to observe the effect of each heat treatment operation. As a result, after running calibration trials, the gain magnetization voltage was set to 20dB and 90 as the amplification (Figure 4.10)

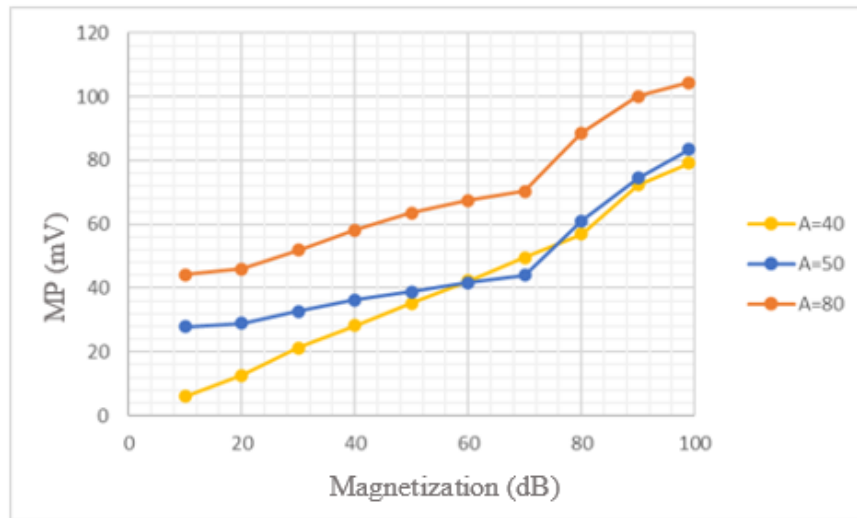


Figure 4.10. Some of the calibration trials as a function of amplification

The measurement system also generates a representative magnetic hysteresis curve for the local measurement area, so relative information on saturation, coercivity, and remanence can be obtained (Figure 4.11)

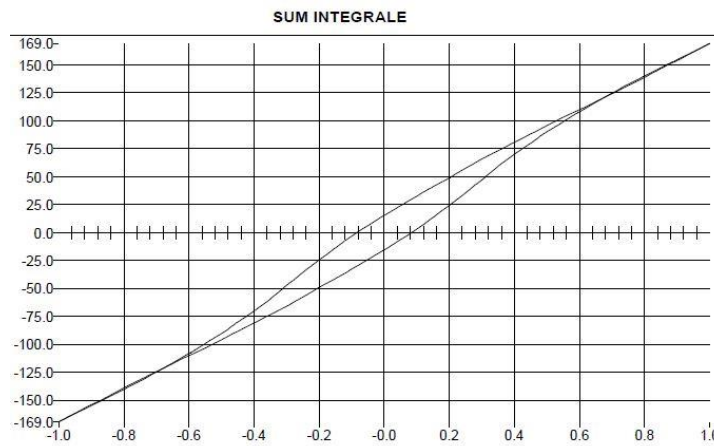


Figure 4.11. Example hysteresis curve obtained from Stresstech Rollscan  $\mu$ Scan 500-2

When using a high frequency ranging from 20 to 1000 kHz, the information can be obtained at 150 to 20  $\mu$ m below the surface [43]. The penetration depth is calculated as 106 $\mu$ m for 125 kHz frequency by using equation 11,  $\mu_r$  was taken as 100 [45]. The electrical resistivity of the carburized SAE 9310 was taken as 17,4  $\mu\Omega \cdot \text{cm}$  [44].



## CHAPTER 5

### RESULTS AND DISCUSSION

#### 5.1 Microstructural Investigation

The microstructural investigation was performed as discussed in the experimental procedure section. Observed microstructures were also checked with the corresponding CCT diagrams and retained austenite measurements.

It was observed that the case of air-cooled and as-quenched samples exhibited martensite and retained austenite (Figure 5.1 and Figure 5.2). The samples developed such microstructures as a result of a shift in the pearlite and bainite start curves on the CCT diagram and a decrease in the martensite start temperatures caused by the carburizing process. Even air cooling was sufficient to achieve the required cooling rate for the transformation of austenite to the martensite phase. On the other hand, microstructures of core regions showed differences while the A sample consist of ferrite and bainite, the A-1 sample consist of martensite.

The case microstructures of the A-1 and the A-3-1 samples show that sub-zero treatment transformed the retained austenite to martensite (Figure 5.1 and Figure 5.2). Retained austenite was shown as white and martensite phase shown as brown at the optical microscope, amount of white area decreased after sub-zero treatment. The rate of decrease was measured at XRD as around 13% between A-1 and A-3-1. The sub-zero treatment did not affect the microstructures of the core region, and the martensite phase was observed in both A-1 and A-3-1 samples (Figure 5.3 and Figure 5.4).

Tempering operation at 150°C transformed martensite to tempered martensite and formed  $\epsilon$ -carbide at the case [50]. On the other hand, tempering at 300°C might transform retained austenite to bainite at the case if kinetic and thermodynamic

requirements were satisfied (Figure 5.1 and Figure 5.2). Under an optical microscope, no retained austenite was observed, and XRD measurements confirmed this.

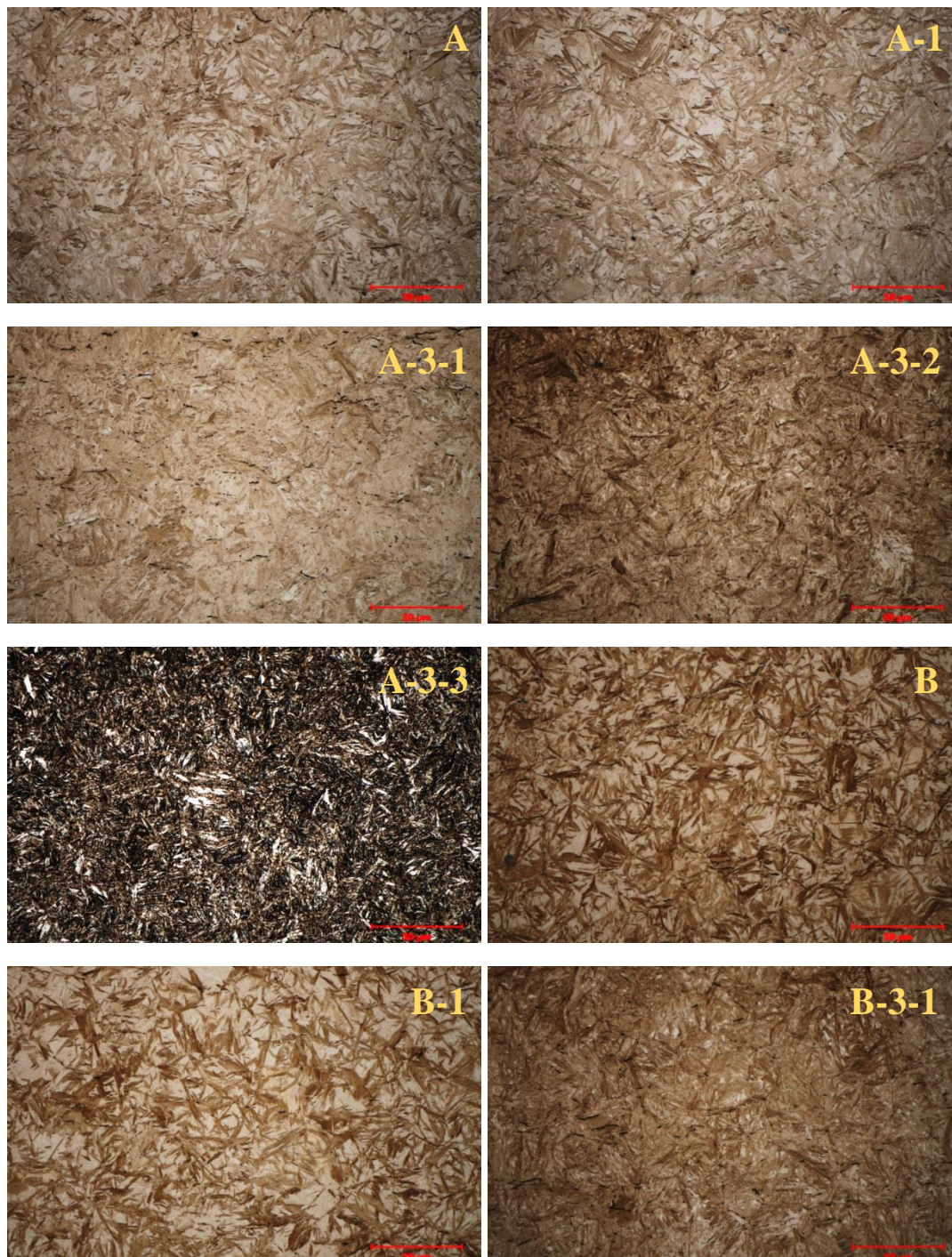


Figure 5.1. Optical micrographs of the case zones, 1000x, %3 nital etched



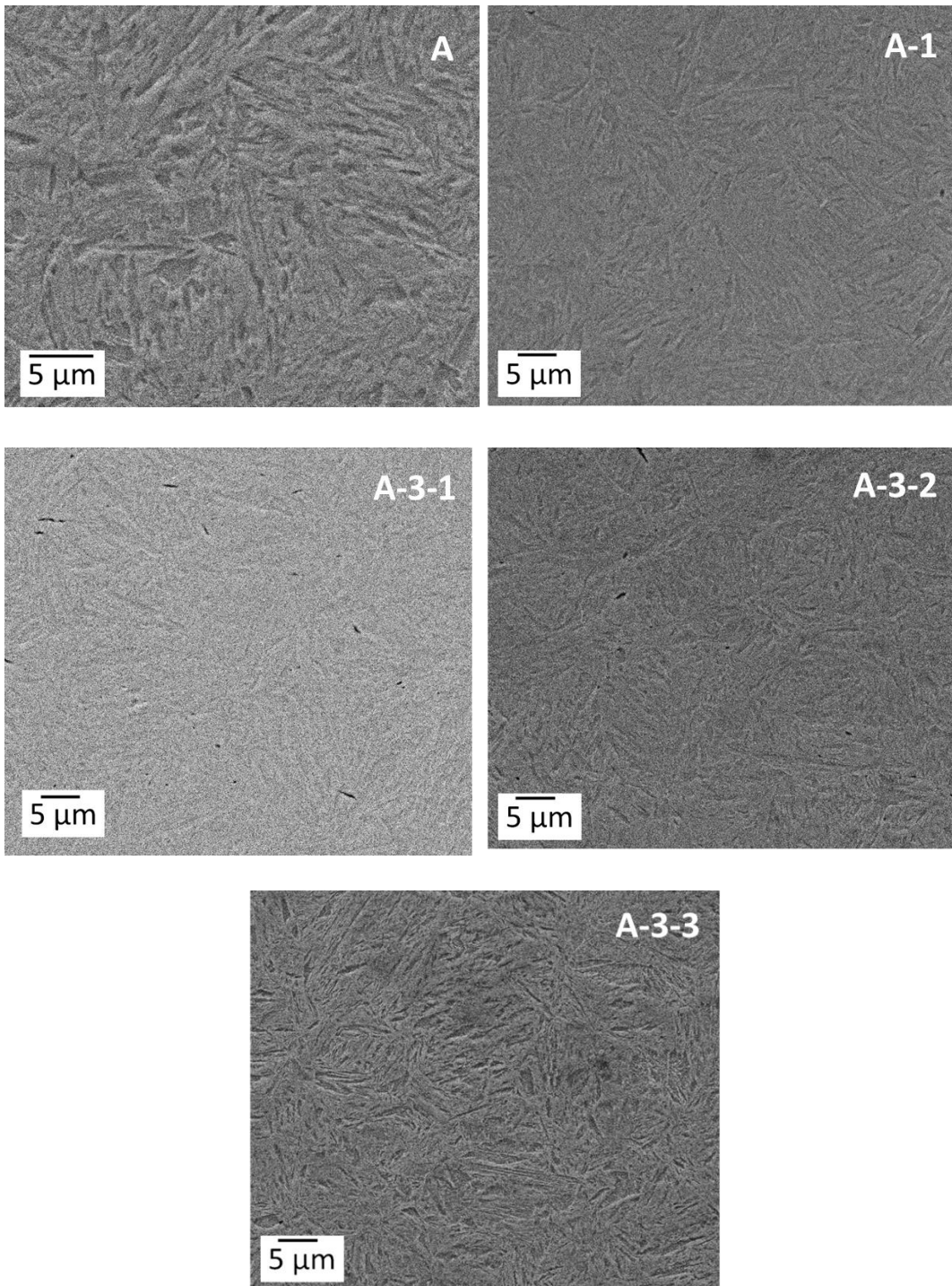


Figure 5.2. SEM micrographs of the case zones

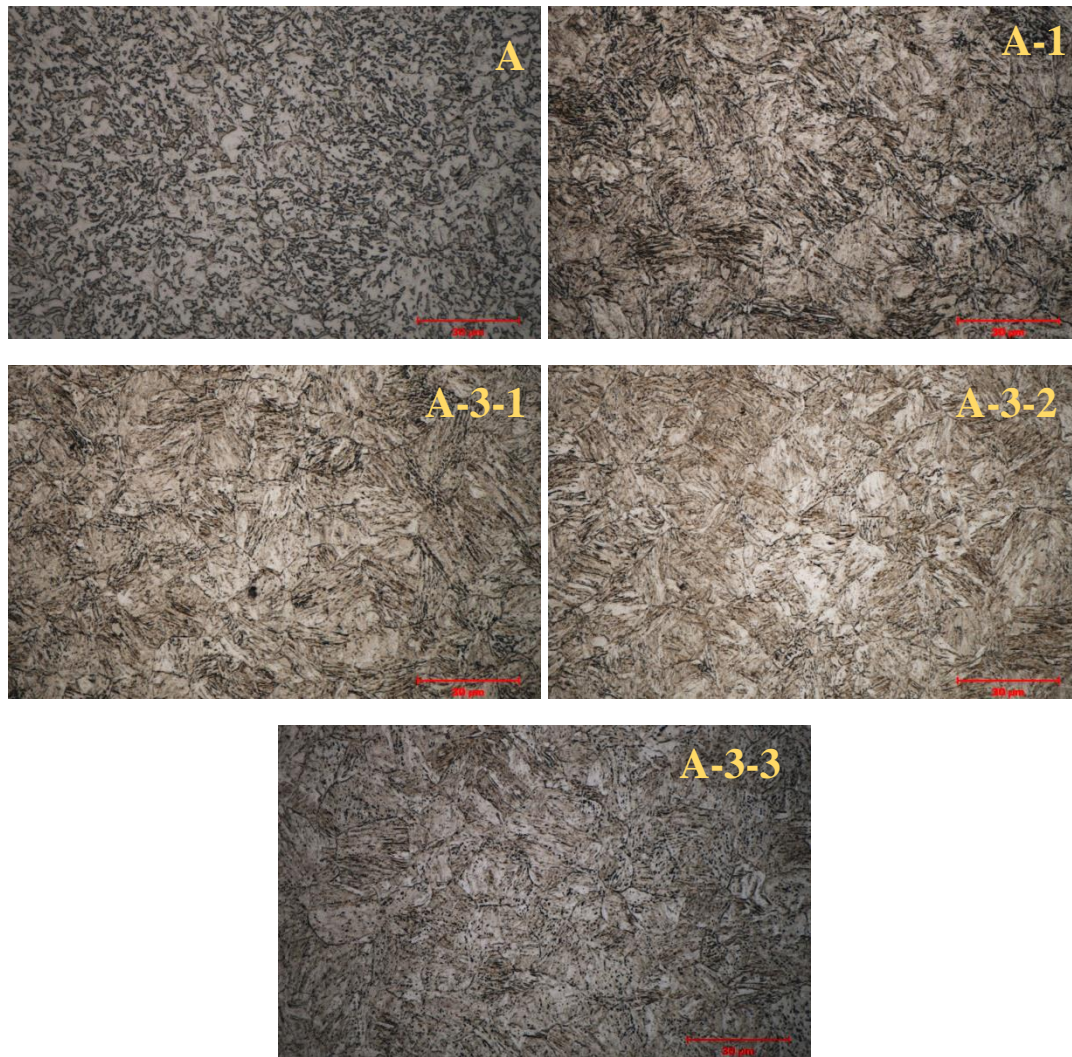


Figure 5.3. Optical micrographs of the core zones, 1000x, %3 nital etched

Besides, no microstructural changes were observed after tempering operations at core regions (Figure 5.3 and Figure 5.4). The cooling type was found to be the most effective parameter on the microstructure of the core region and thus the hardness among the experimental carburizing parameters (Figure 5.3 and Figure 5.4).

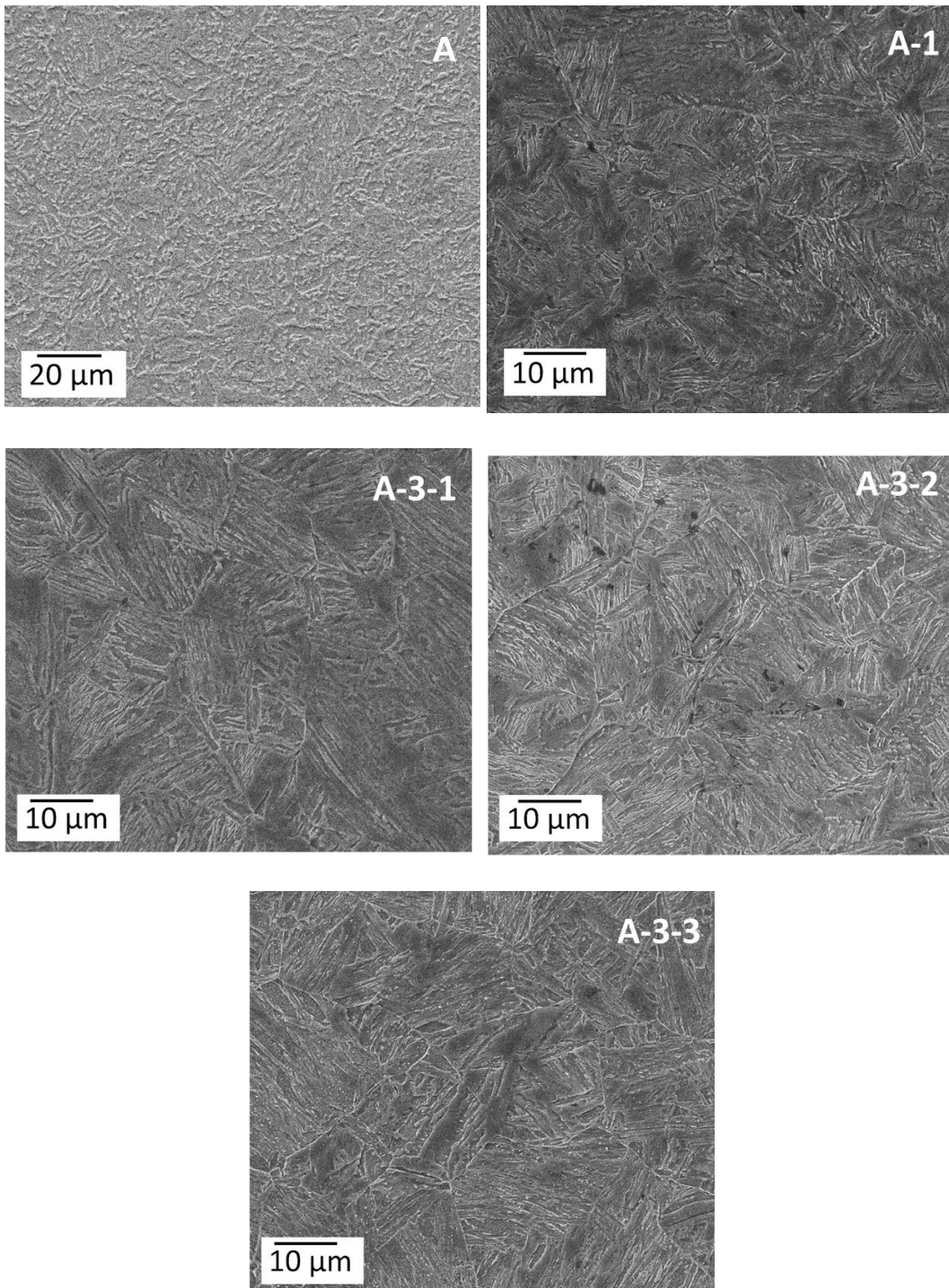


Figure 5.4. SEM micrographs of the core zones

Intergranular oxidation was analyzed at SEM by EDS technique and the oxygen amount of the related grain boundaries was found higher than the other regions (Figure 5.5). Although the light elements such as Carbon and Oxygen analysis at EDS have higher error than the heavy elements, EDS results showed that Oxygen accumulated at grain boundaries (Table 5.1).

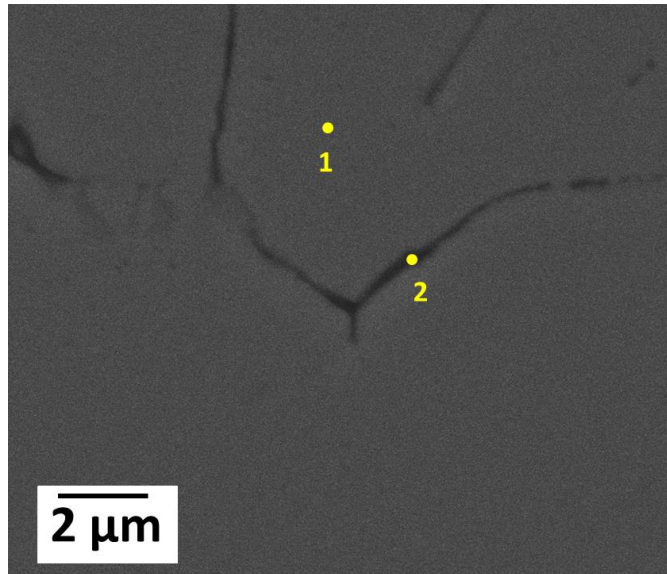


Figure 5.5. Intergranular oxidation under a scanning electron microscope

Table 5.1 Chemical composition of the grain boundary and the grain taken by EDS

Element	Point 1		Point 2	
	Wt. %	At. %	Wt. %	At. %
<b>C</b>	0,80	3,58	1,38	5,62
<b>O</b>	0,09	0,32	2,04	6,24
<b>Si</b>	0,59	1,13	4,45	7,73
<b>Cr</b>	0,88	0,92	0,61	0,64
<b>Mn</b>	0,45	0,44	0,46	0,41
<b>Ni</b>	3,23	2,97	2,18	1,82
<b>Fe</b>	Balance	Balance	Balance	Balance



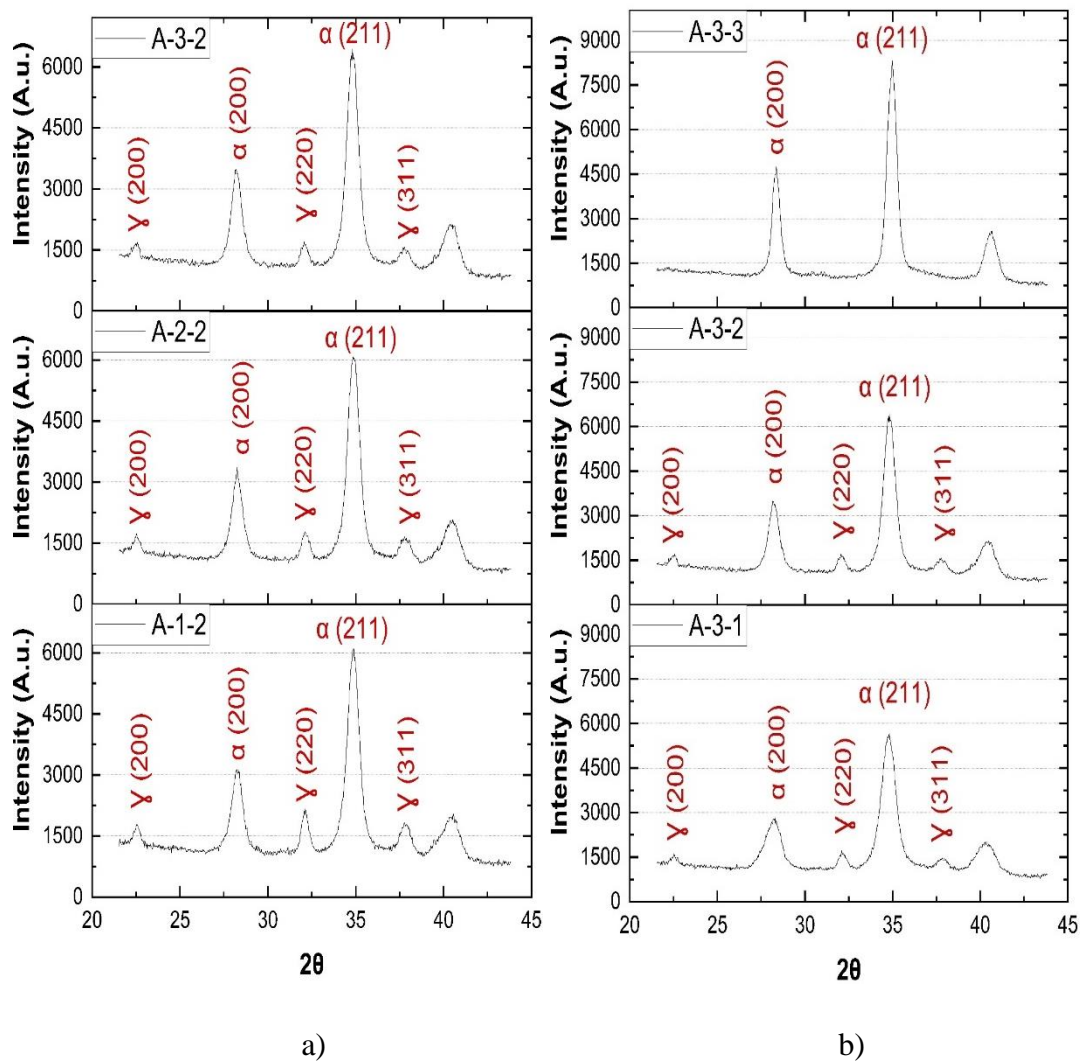


Figure 5.7. XRD pattern of retained austenite measurements of the a) A-1-2, A-2-2 and A-3-2, showing the effect of sub-zero treatment b) A-3-1, A-3-2, and A-3-3, showing the effect of tempering temperature

Table 5.2 Retained-austenite content of the specimens

Sample	Retained Austenite (%)	Sample	Retained Austenite (%)
A	18,8 ± 0,1	B	18,4 ± 0,2
A-1	19,0 ± 0,2	B-1	25,4 ± 0,3
A-1-1	15,0 ± 0,2	B-1-1	17,0 ± 0,2
A-1-2	13,4 ± 0,1	B-1-2	15,9 ± 0,1
A-1-3	Below 1	B-1-3	Below 1
A-2-1	11,2 ± 0,1	B-2-1	11,0 ± 0,1
A-2-2	9,6 ± 0,1	B-2-2	10,5 ± 0,1
A-2-3	Below 1	B-2-3	Below 1
A-3-1	6,6 ± 0,1	B-3-1	7,9 ± 0,1
A-3-2	7,1 ± 0,1	B-3-2	7,8 ± 0,1
A-3-3	Below 1	B-3-3	Below 1

Each sample had a different % retained austenite. They can be categorized and studied based on distinctive steps of the carburizing recipe such as carburizing time, cooling rate, medium, cryogenic treatment temperature, and tempering temperature.

A similar effect of carburizing time was observed on all samples independent from the subsequent heat treatments. 6 hours carburized group B samples has more retained austenite than the 3 hours carburized group A. For example, the B-1 contains more retained austenite than the A-1, which can be attributed to the B-1 sample's higher surface carbon content as a result of the longer carburizing time. The area under the (211) and (200) ferrite peaks of the A-1 sample was greater than that of the B-1 sample however such a big difference was not observed at (220) and (311) austenite peaks. (Figure 5.6). The biggest difference exists between A-1 and B-1 which are at the as-quenched condition, further heat treatment steps minimize the retained austenite difference either by forming martensite, carbide precipitations at sub-zero treatment and  $\epsilon$ -carbide precipitation in tempering at 150°C and transformation into bainite in tempering at 300°C [41] (Figure 5.6).

It was observed that air-cooled samples have less % retained austenite than the oil quenched ones. The reason could be shown as the decarburization during the cooling stage, the air-cooled parts were exposed to open air just after carburizing.

Cryogenic treatment seems to be the most effective tool to change the retained austenite (Figure 5.7). A-1-1, A-2-1, and A-3-1 were subjected to sub-zero treatment at -25, -75, or -100°C respectively, at the beginning the retained austenite values of them were about 19%, and after treatment, they decrease to 15, 11, and 7%, respectively (Table 5.2). The gradual decrease in the area and intensity was observed at (220) and (311) austenite peaks while lowering the sub-zero temperature (Figure 5.7).

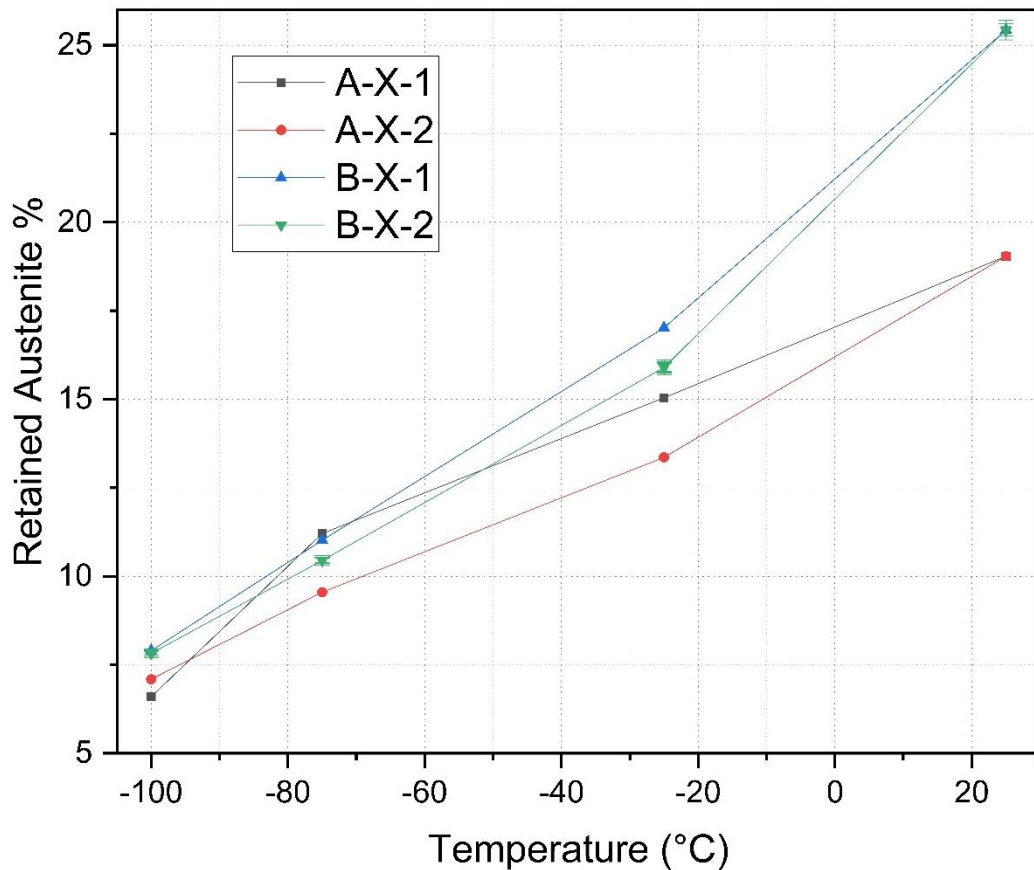


Figure 5.8. Effect of sub-zero treatment temperatures on the amount of retained austenite of A-X-1, A-X-2, B-X-1, B-X-2 samples, X denotes 1,2,3



Tempering also reduces the retained austenite content of the samples. Tempering wasn't applied to the A-3-1 sample however, A-3-2 and A-3-3 samples were tempered at 150 and 300°C respectively. As tempering temperature increases austenite peaks diminish, eventually after tempering the samples at 300°C they disappeared (Figure 5.7). For both A and B group samples, tempering at 150°C didn't make a remarkable change, just decreased retained austenite content around 2% by forming  $\epsilon$ -carbide precipitates [50] (Figure 5.8). Despite that, tempering at 300°C induced transformation of thermodynamically unstable retained austenite to martensite and bainite, also proven with calculated CCT and TTT diagram [51]. A representative TTT diagram for the A-3-3 sample determined by JMatPro is given in Figure 5.8 to show the heat treatment path.

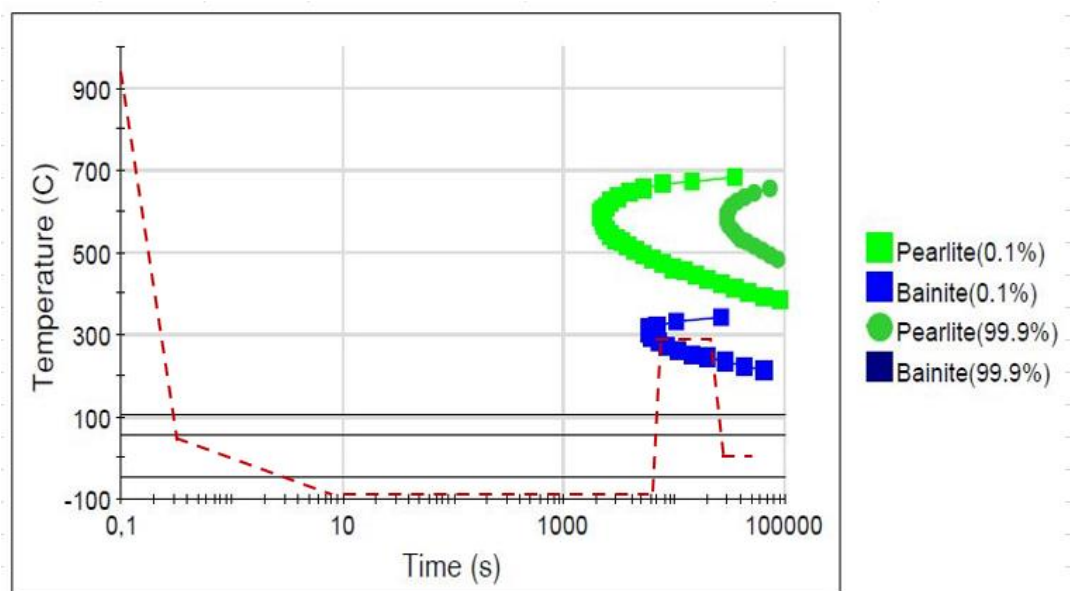


Figure 5.9. Representative TTT diagram of the A-3-3, calculated by JMatPro, no scale

In addition to retained austenite measurements, a glow discharge optical spectrometer (SPECTRUMA Analytik) was used to analyze surface carbon content of the 3-hours carburized and 6 hours carburized specimens, the 3hours carburized specimen's surface carbon content found as 0,89 and that of 6hours carburized

specimens found as 0,94wt.%C. Similar surface carbon contents were observed with measurements and the calculated values (Table 4.4).

### 5.3 Hardness Test Results

The effect of cooling rate on case depth and surface hardness was demonstrated in the hardness test (Figure 5.10). Surface hardness was higher in the air-cooled samples A and B than in the quenched samples A-1 and B-1.

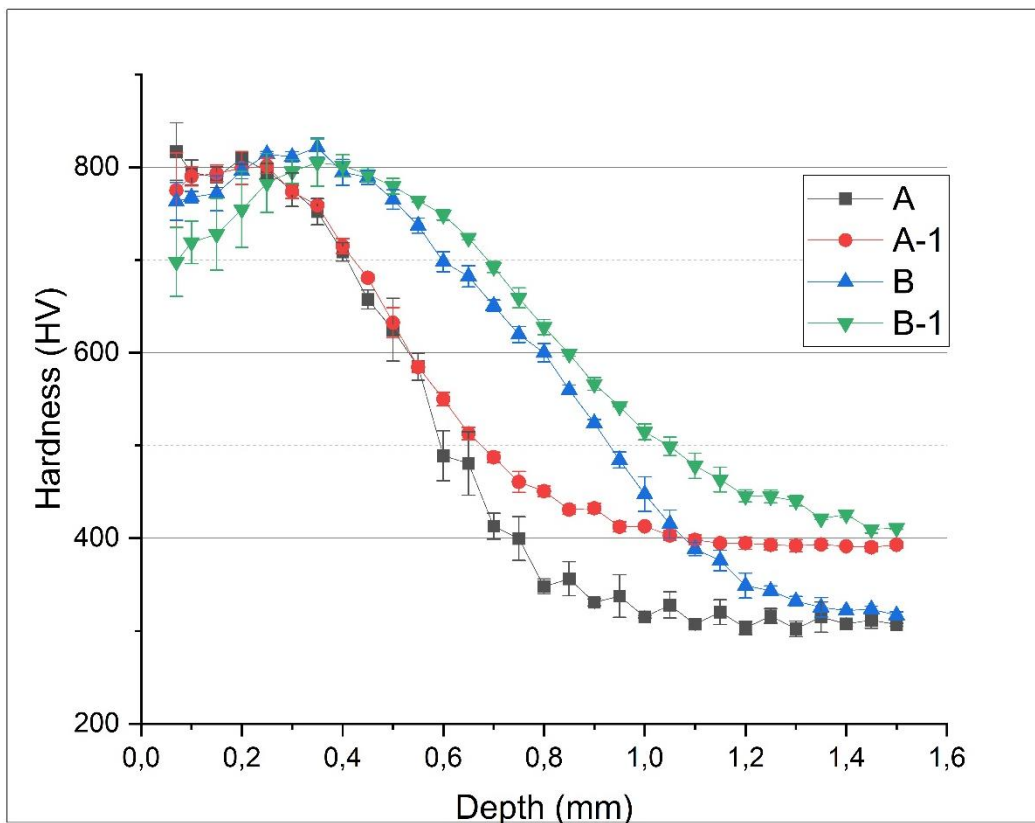


Figure 5.10. Hardness depth profiles of the A, A-1, B, B-1, showing the effects of cooling rate

However, that situation was not valid for the hardness profile. For example, the B and B-1 samples had 0,91 and 1,01mm case depth respectively. While their surface hardness values were 763 and 698HV. Till the 0,3mm depth, air-cooled sample B had a higher hardness than the quenched sample B-1. Below the depth of 0,3mm, the

hardness of quenched sample B-1 exceeded that of sample B. The same trend was also observed on the A and A-1 samples, however, the breaking point was around 0,2mm. That difference occurred due to the carbon profile since higher carburizing time results in a higher carbon profile while other carburizing process parameters were kept constant. The reason for the higher hardness of the air-cooled samples can be regarded as the higher amount of retained austenite in the quenched samples, which is proven by the XRD measurements.

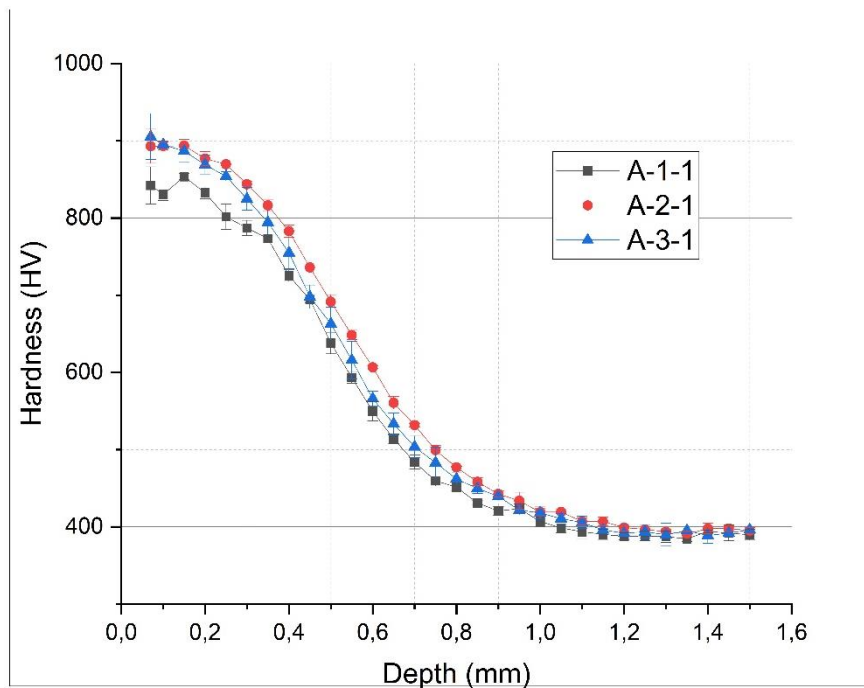


Figure 5.11. Hardness depth profiles of the A-1-1, A-2-1, A-3-1, showing the effect of sub-zero treatment temperature

According to the hardness test results, sub-zero treatment temperature did not cause a significant difference. The hardness profile obtained for  $-25^{\circ}\text{C}$  treatment gave the lowest values. However, 697HV and 513 HV hardness depths showed a slight shift (Figure 5.11). Furthermore,  $-75^{\circ}\text{C}$  and  $-100^{\circ}\text{C}$  sub-zero treated samples produced nearly identical results. For example, A-2-1 and A-3-1 samples had 893 and 905HV surface hardness and 0,73 and 0,69 case depth respectively. As a result, sub-zero treatment had a minor effect on the oil quenched samples.

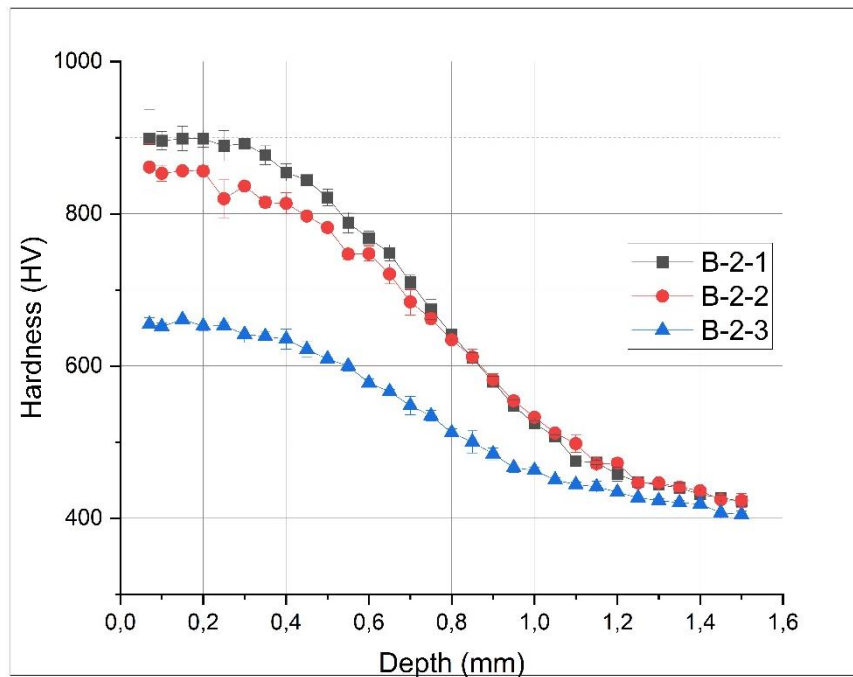


Figure 5.12. Hardness depth profiles of the B-2-1, B-2-2, B-2-3, showing the effect of tempering temperature

Hardness test results indicated that tempering affects hardness profile significantly, especially after a certain temperature. For instance, identical samples were produced using the same recipe only difference was the tempering temperature, B-2-1 was not tempered B-2-2, and B-2-3 samples were exposed to tempering treatment at 150°C and 300°C (Figure 5.12). B-2-1 and B-2-2 produced nearly the same results, their surface hardness values were 898 and 861, and case depths were 1,03 and 1,05 respectively. The hardness profile of them followed the same path after 0,7mm. On the contrary, the B-2-3 sample, tempered at 300°C, showed a dramatic decrease both at the surface hardness and case depth. It did not show even 697HV surface hardness, it was measured as 655HV, and case depth was measured as 0,81mm, due to cementite formation at 300°C and reduction in dislocation density [51]. The tempering operation had a greater impact on the surface and near-surface regions than on the deeper zone. Since carbon content decreases by obeying Fick's diffusion laws. Hence, an increase in carbon content results in a decrease at bainite start temperature and 300°C tempering passes the bainite start line at both 3 hours and 6

hours carburized samples. So, tempering at 300°C reduced hardness values at the case region.

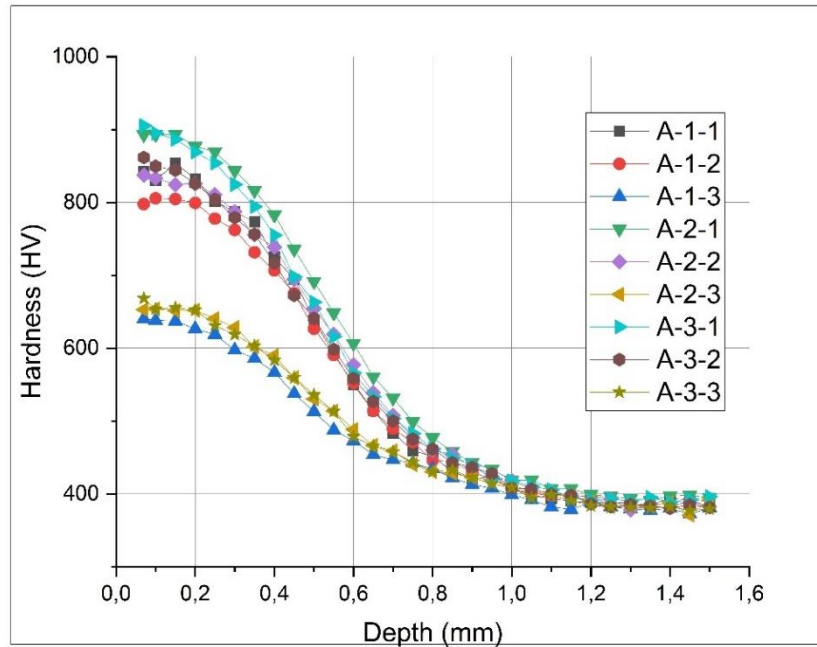


Figure 5.13. Hardness depth profiles of the sample group A

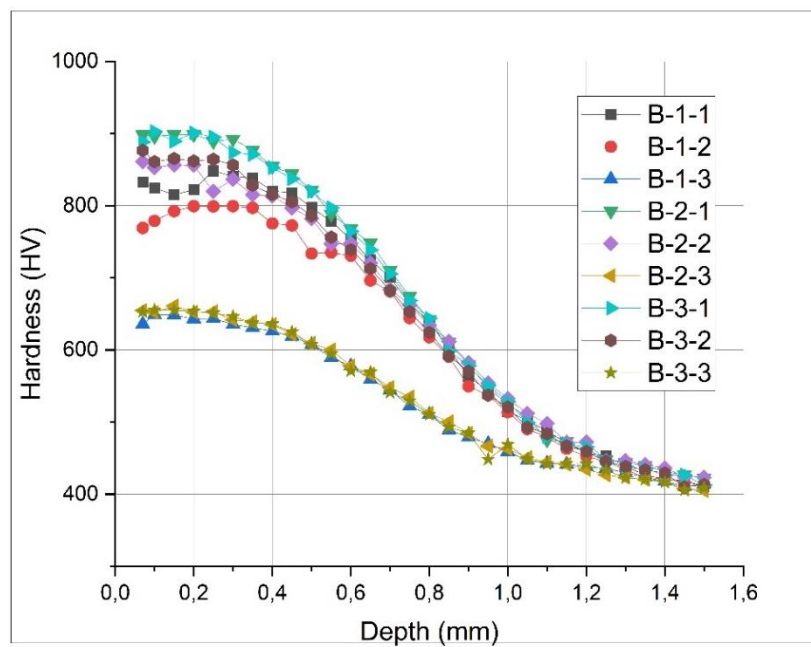


Figure 5.14. Hardness profiles of the sample group B

The hardness profiles of the group A and group B samples are given in Figure 5.13 and Figure 5.14. It is seen that tempering temperature is the most powerful parameter for the hardness profile. All 300°C tempered both A and B samples were grouped separately from the other samples in terms of low hardness behavior.

The cooling rate was discovered to be the only important parameter for regions that weren't affected by diffusion (core); after quenching, the core region's hardness values were not significantly affected by subsequent operations. In that study, after quenching the core hardness remained constant at the 37-38HRC band and didn't change. On the other hand, the air-cooled samples showed a 27-28HRC band (Table 5.3). It was also related to the stability of the phases at process temperature and constant carbon content at the core regions, also proven with CCT and TTT diagrams.

Carburized SAE 9310 steel components are generally designed for min. 60HRC (697HV) surface hardness to obtain optimum wear resistance, strength, and toughness properties. Therefore, the minimum depth of specified case hardness (697HV) becomes an important hardness parameter per AMS 2759 7/B [47]. AMS 2759 7/B defines case depth as the depth below the surface where the hardness is equivalent to 50 HRC (513HV).

Minimum depth of specified case hardness was mainly related to the carburizing time, 3h carburized group A specimens had roughly 697HV depth below 0,4mm, that of group B specimens was 0,7mm. 697HV depth was affected slightly from subsequent processes (cooling rate, sub-zero temperature, and tempering), excluding over tempering. The over tempering (300°C) decreased surface hardness below 697HV. On the other hand, the effect of over tempering on case depth (513HV) was lower.

Table 5.3 Results of the hardness measurements: surface and core hardness, and the depths corresponding to 697HV and 513HV

Sample	Surface Hardness (HV0,5)	697 HV0,5 (mm)	513 HV0,5 (mm)	Core Hardness (HV10)
A	817	0,41	0,60	284
A-1	775	0,43	0,65	366
A-1-1	842	0,45	0,65	368
A-1-2	797	0,42	0,65	367
A-1-3	640	-	0,50	364
A-2-1	893	0,49	0,73	375
A-2-2	838	0,45	0,69	365
A-2-3	653	-	0,56	368
A-3-1	905	0,46	0,69	366
A-3-2	862	0,42	0,67	366
A-3-3	668	-	0,56	364
B	763	0,62	0,91	287
B-1	698	0,69	1,01	374
B-1-1	832	0,70	1,02	371
B-1-2	769	0,66	1,00	367
B-1-3	636	-	0,79	373
B-2-1	898	0,72	1,03	369
B-2-2	861	0,69	1,05	367
B-2-3	655	-	0,81	366
B-3-1	888	0,71	1,02	371
B-3-2	877	0,68	1,01	371
B-3-3	653	-	0,79	370

## 5.4 Results of Magnetic Barkhausen Noise Measurements

MBN measurements were carried out with the following settings, gain magnetization voltage and amplification values were 20 and 90 respectively. To observe the impact of each carburizing parameter, sample group A, 3 hours carburized, was drawn in relative RMS voltage versus relative magnetic excitation field graph (Figure 5.15). Microstructure change as a function of cooling rate had the greatest effect on the MBN pattern. Since retained austenite is not ferromagnetic, an increase in retained austenite content reduces the RMS voltage, which could be attributed to increasing in magnetic domain free regions [53].

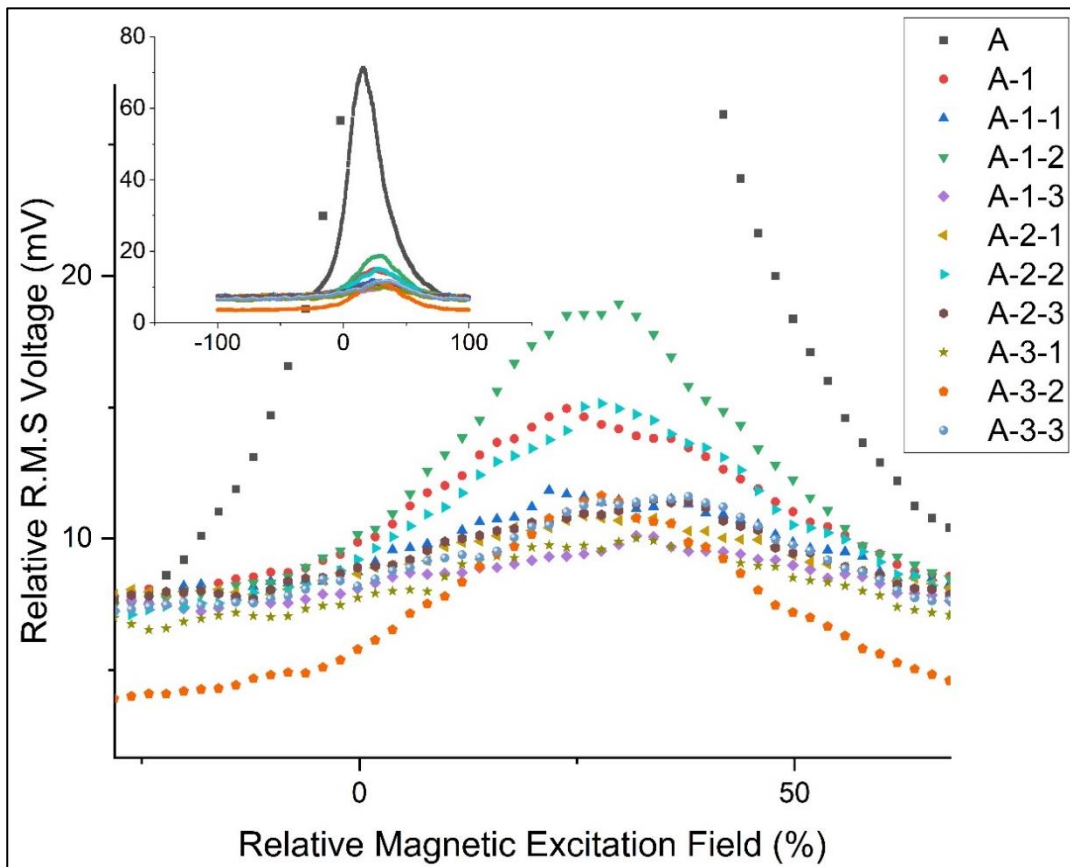


Figure 5.15. Relative RMS voltage versus relative magnetic excitation field data of the group A samples



For instance, the air-cooled sample, A, can be easily distinguished from other samples. It was affected by the relative magnetic excitation field at lower percentages than the others, i.e., broader than the remaining samples.

Using the MBN method, one part that has completed its entire heat treatment recipe can be distinguished from the unfinished one. For example, the B-2-2 was produced with a full heat treatment cycle, whereas the B was only carburized and air-cooled. To achieve the final heat treatment condition, it must be austenitized and quenched, subsequent sub-zero treatment and finally tempering operation. MBN measurements of the samples revealed that the unfinished sample, B, had a higher RMS voltage and broader relative magnetic excitation field percentage than the finished, B-2-2, sample (Figure 5.16).

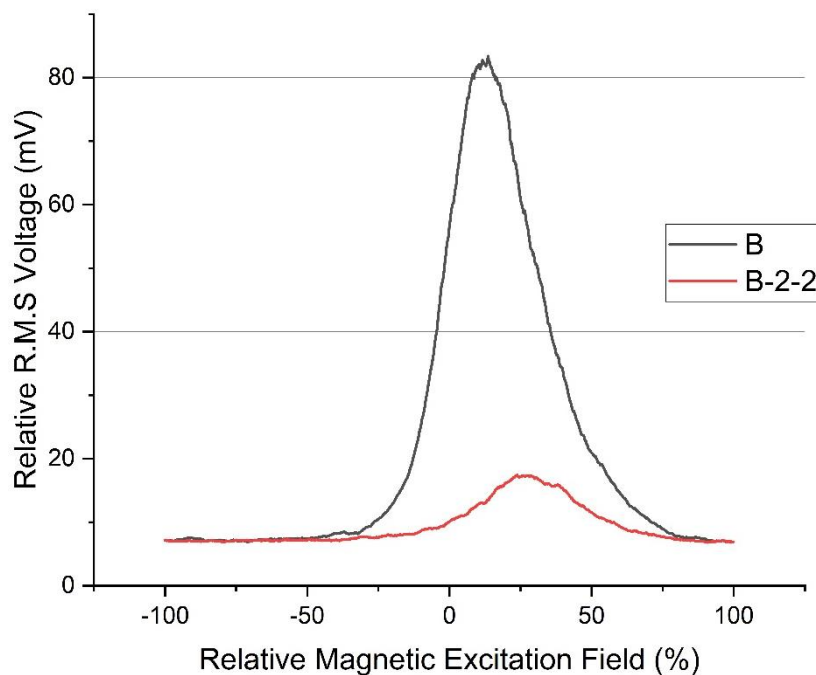


Figure 5.16. Relative RMS voltage versus relative magnetic excitation field data of the B and B-2-2

As the sub-zero temperature dropped lower degrees, RMS voltage reduced due to the fine carbide precipitation and the increase in dislocation density [41]. A decrease in sub-zero treatment temperature increases the magnitude of compressive residual

stress. Microstructural change and residual stress have a combined effect on MBN emission levels. For instance, A-1-2, A-2-2, A-3-2 samples were identically processed except the sub-zero treatment temperatures:  $-25^{\circ}\text{C}$ ,  $-75^{\circ}\text{C}$ , and  $-100^{\circ}\text{C}$ . The A-3-2 sample had the lowest MBN peak (10,9mV), and the A-1-2 sample had 18,0mV. A-1-2 and A-2-2 sample's MBN patterns were close to each other, on the contrary, the A-3-2 showed a higher difference from them (Figure 5.17).

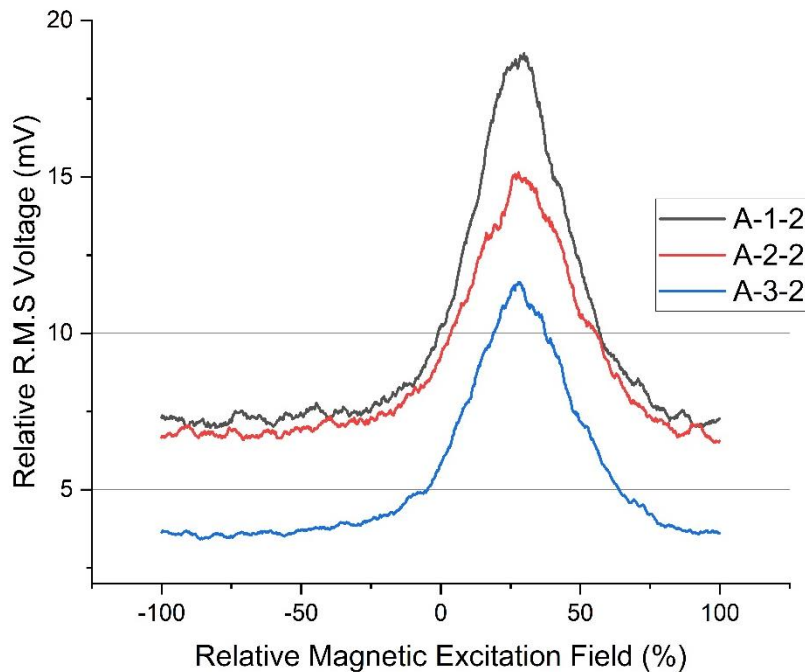


Figure 5.17. Relative RMS voltage versus relative magnetic excitation field data of the A-1-2, A-2-2, A-3-2, cryogenic treatment at  $-25^{\circ}\text{C}$ ,  $-75^{\circ}\text{C}$  and  $-100^{\circ}\text{C}$

The variation of carburizing time at  $925^{\circ}\text{C}$  did not show a significant effect on MBN emission, higher carburizing time caused a slight increase at the RMS voltages. As an example, A-2-2 and B-2-2 samples were subjected to nearly identical processes, with the only difference being the carburizing time, 3 hours and 6 hours respectively, in addition, their both case and core microstructures are similar as tempered martensite and retained austenite. MBN patterns of them were so close to each other. It is difficult to determine which pattern belongs to A or B without knowing the samples (Figure 5.18).

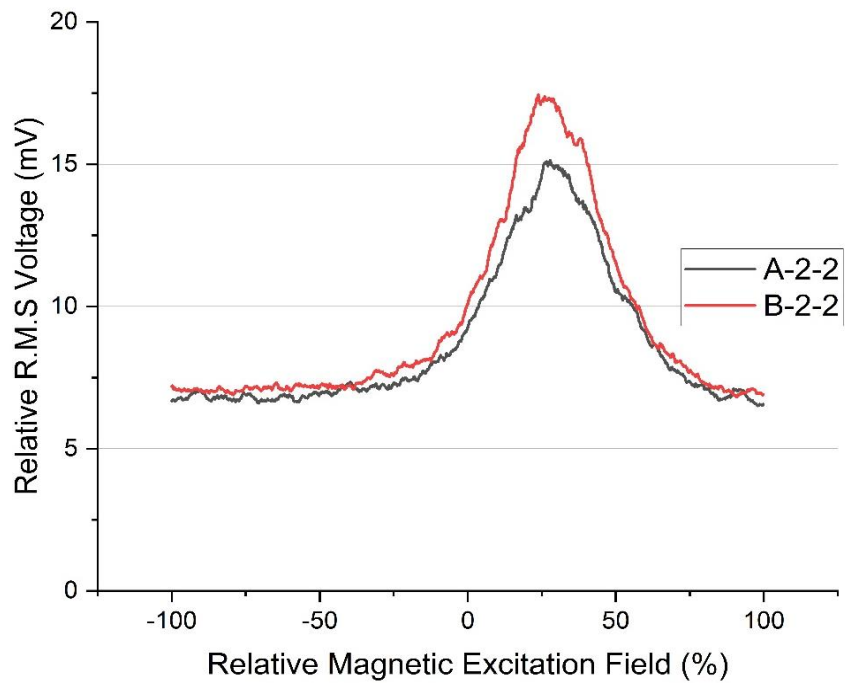


Figure 5.18. Relative RMS voltage versus relative magnetic excitation field data for A-2-2 and B-2-2, carburized for 3 hours and 6 hours, respectively

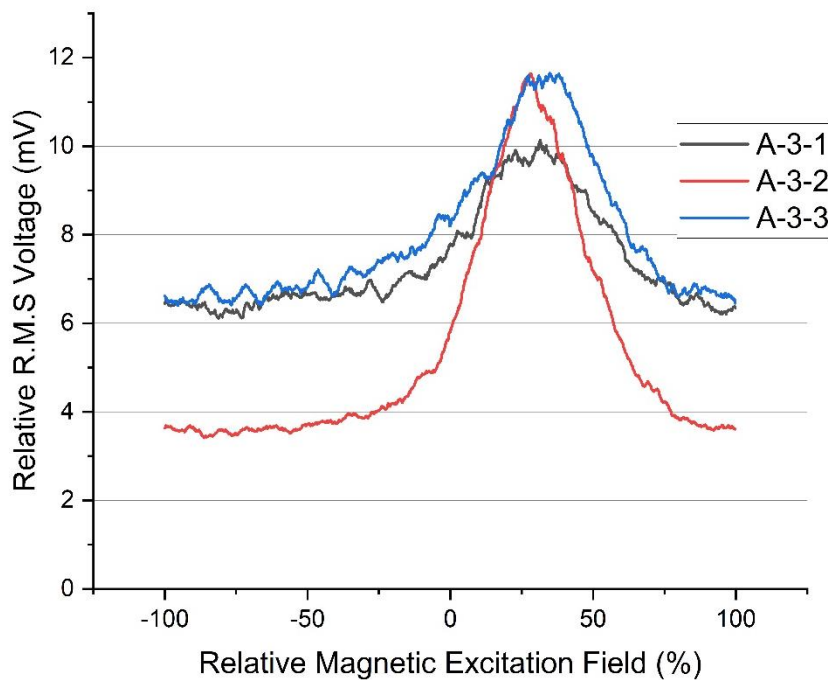


Figure 5.19. Relative RMS voltage versus relative magnetic excitation field data of A-3-1, A-3-2 and A-3-3, untempered, tempered at 150°C and 300°C, respectively

Depending on the tempering temperature, there will be alterations in both microstructure and the severity of the residual stress at different levels. For instance, after 300°C tempering, the surface residual stress is almost relieved (-509MPa to 80MPa), and the microstructure remarkably changes in comparison to the untempered sample and the sample tempered at 150°C by the transformation of retained austenite, and formation of carbides depending on the tempering temperature. Correspondingly, the maximum peak level of MBN increases, and the MBN peak gets sharper. It is rather difficult to differentiate the effects of microstructure and residual stress if the process applied changes both of them. The maximum peak level for the A-3-1 sample was 9,8mV, while those levels were 10,9mV and 11,4mV for A-3-2 and A-3-3 respectively (Figure 5.19). In addition to that, the MBN profiles of A-3-1 and A-3-3 samples resembled each other. The MBN emission levels before the peak starts were nearly the same. However, A-3-1 had the highest surface hardness and compressive stress out of the three samples. Those values were low at the A-3-3, transformation of retained austenite to bainite and carbide formation might be the reason. Furthermore, although the tempering temperature of the A-3-2 below that of the A-3-3, and A-3-1 sample wasn't tempered, the A-3-2 gave the sharper peak and MBN level before peak start was lowest. According to Kaleli and Gür, at low tempering temperatures, changes are happened primarily by carbon atom rearrangements, recovery, and retained austenite transformation to the mixture of carbide and ferrite. At higher temperatures carbide transformations are replaced by cementite and ferrite formation. Combinations of that issues reduce the magnitude of compressive residual stress and hardness significantly. So, a lower amount of magnetic field will be enough to domain wall movements, which increases the RMS voltage [48].

MBN patterns can be represented by the RMS voltage or the maximum MBN peak level since there is a linear relation between them (Figure 5.20). All A and B group samples results were drawn in a graph with a low error margin and it indicates that to analyze the MBN pattern either RMS or maximum MBN peak level can be used.

MBN results versus hardness graphs also support it (Figure 5.21, 5.22, 5.23, and 5.24).

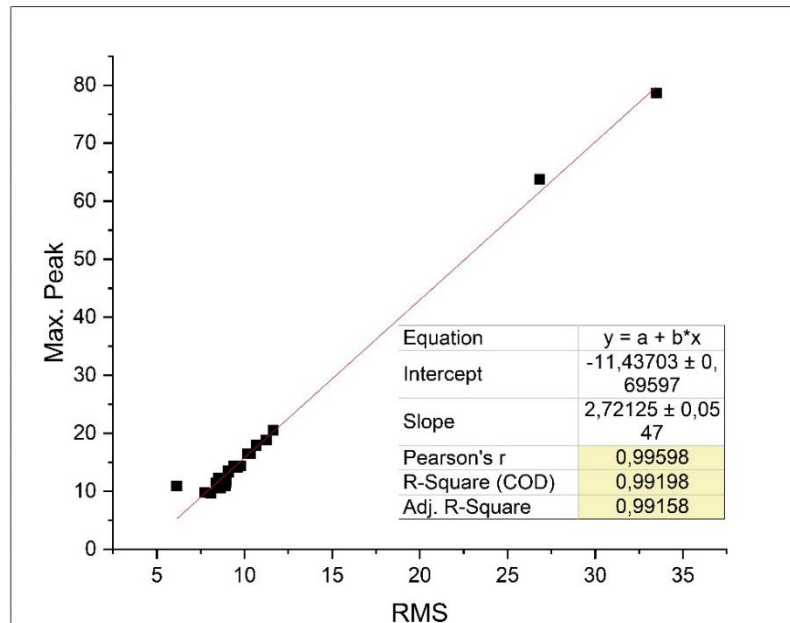


Figure 5.20. Graph of maximum peak versus RMS, MBN measurements

By forming groups based on tempering temperatures, the correlation between hardness and MBN parameters was discussed. 300°C tempered A-X-3 samples had the lowest hardness values and their RMS voltages were between 8-10mV (Table 5.4). The same situation is also valid for the B-X-3 samples (Figure 5.23, 5.24). Normally, it is expected that lower hardness corresponds to a higher RMS voltage but in the 300°C tempered samples, the RMS voltages were close to the high hardness samples.

150°C tempered A-X-2 and B-X-2 samples showed a variation in both hardness and RMS values as sub-zero temperature reduced i.e., hardness increased while RMS voltages decreased (Figure 5.21 and 5.23). The reason might be dependent on the relation between hardness and RMS voltage. Where an increase in hardness results in a reduction in the RMS voltages by keeping residual stress constant, and having the same morphology with different phase amounts.

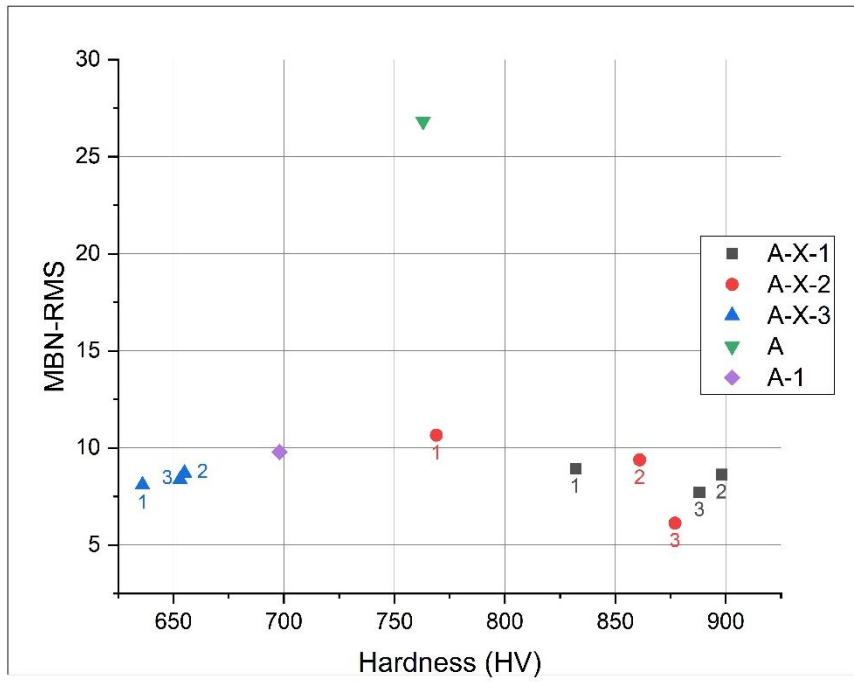


Figure 5.21. Variation of MBN-RMS with hardness, group A

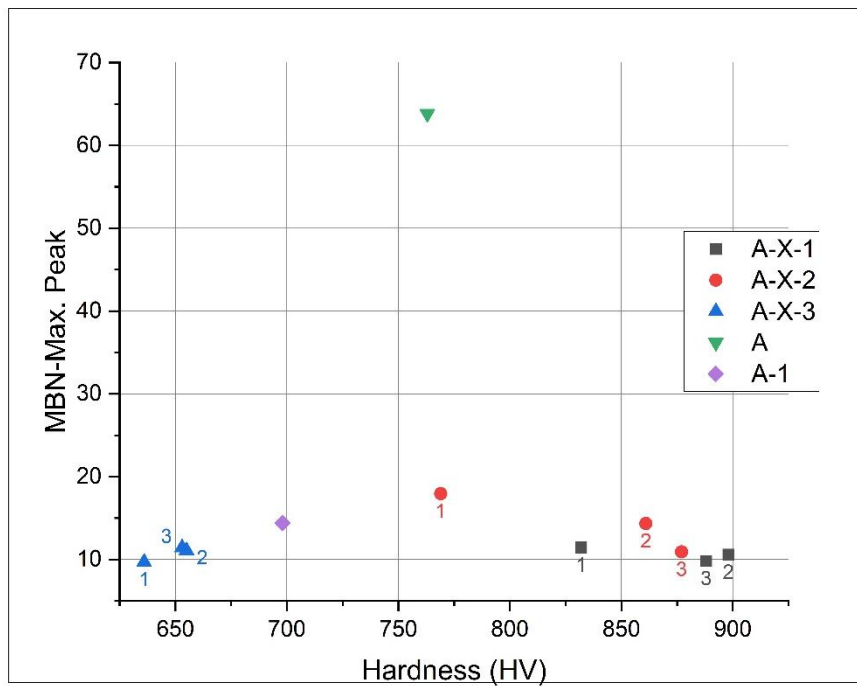
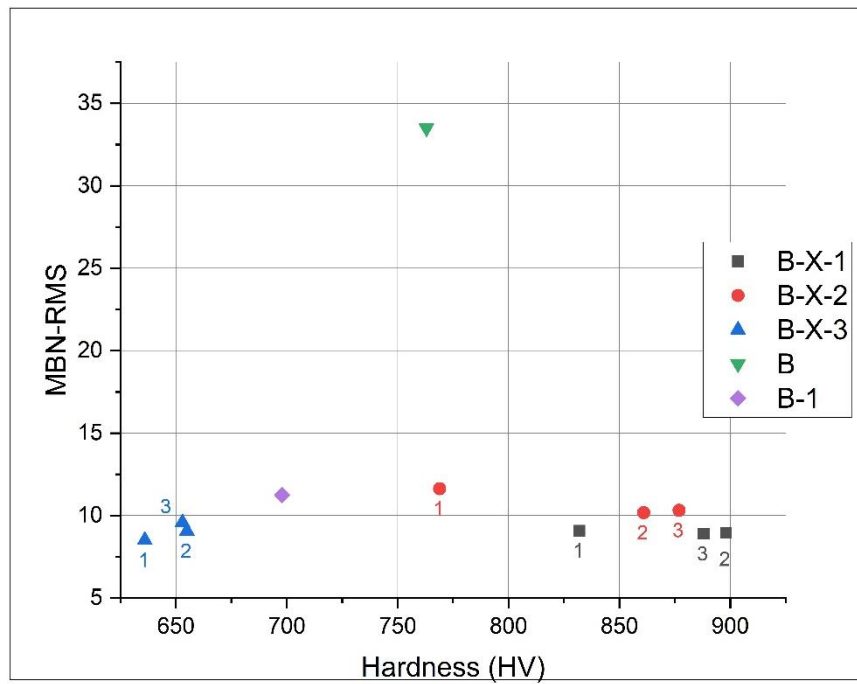


Figure 5.22. Variation of MBN-Maximum peak with hardness, group A



When true tempering temperatures were applied to the samples, different sub-zero temperatures can be distinguished from each other. But if the non-tempering or over-tempering were applied to the samples effect of the previous process such as sub-zero treatment cannot be differentiated from each other only by the MBN method (Figure 5.21, 5.22, 5.23, and 5.24).

Table 5.4 Results of MBN measurements

Sample	RMS (mV)	Max. Peak (mV)	Saturation (Tesla)	Coercivity (kA/m)	Remanence (Tesla)
A	26,8	63,8	368,8	0,16	182,0
A-1	9,8	14,4	184,3	0,12	25,3
A-1-1	8,9	11,5	169,1	0,09	15,1
A-1-2	10,7	18,0	192,6	0,15	38,7
A-1-3	8,1	9,7	155,7	0,07	10,8
A-2-1	8,6	10,6	164,3	0,07	11,6
A-2-2	9,4	14,4	173,8	0,13	27,9
A-2-3	8,7	11,1	168,4	0,07	13,4
A-3-1	7,7	9,8	146,6	0,09	14,4
A-3-2	6,1	10,9	106,6	0,17	27,2
A-3-3	8,4	11,4	159,2	0,10	18,3
B	33,5	78,7	460,5	0,13	188,9
B-1	11,2	18,9	204,0	0,12	40,6
B-1-1	9,1	13,3	170,8	0,11	23,3
B-1-2	11,6	20,6	209,1	0,15	47,5
B-1-3	8,5	12,3	159,1	0,11	21,5
B-2-1	9,0	11,9	171,0	0,08	15,0
B-2-2	10,2	16,5	185,9	0,14	33,7
B-2-3	9,1	13,6	169,1	0,13	23,9
B-3-1	8,9	11,0	168,1	0,06	10,8
B-3-2	10,3	16,5	192,1	0,13	33,5
B-3-3	9,6	14,2	177,8	0,13	26,1

The representative saturation, coercivity, and remanence values cannot be used as true values because magnetization is applied on the local spot in the MBN method, the actual values are far beyond.



### 5.4.1 Magnetic Hysteresis Curves

As the carburizing time was increased magnetic saturation also increased, on the contrary, the same logic was not valid for the coercivity (Figure 5.25). Coercivity values showed slight variation, implying that the values were insufficient and close to each other for stating a general argument.

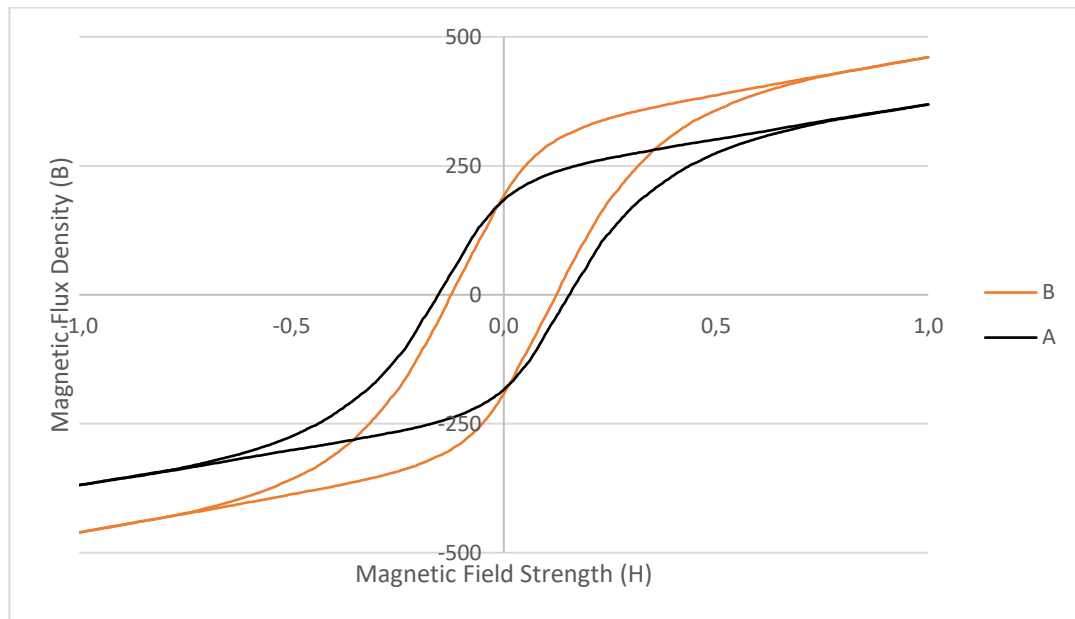


Figure 5.25. Magnetic hysteresis curves of A and B samples, showing the effect of carburizing time

Magnetic hysteresis curves revealed that the cooling rate was critical for magnetic saturation and coercivity, even if the final microstructure morphologies were almost identical. While the saturation and coercivity values in the quenched sample were lower, the values in the air-cooled one were higher (Figure 5.26). Although the difference in saturation points between A and A-1 was nearly twice that of the quenched sample, the difference between coercivity values was less. A similar tendency exists for B and B-1 (Figure 5.27). B had 461 and 0,13 saturation and coercivity values respectively, while B-1 had 204 and 0,12.

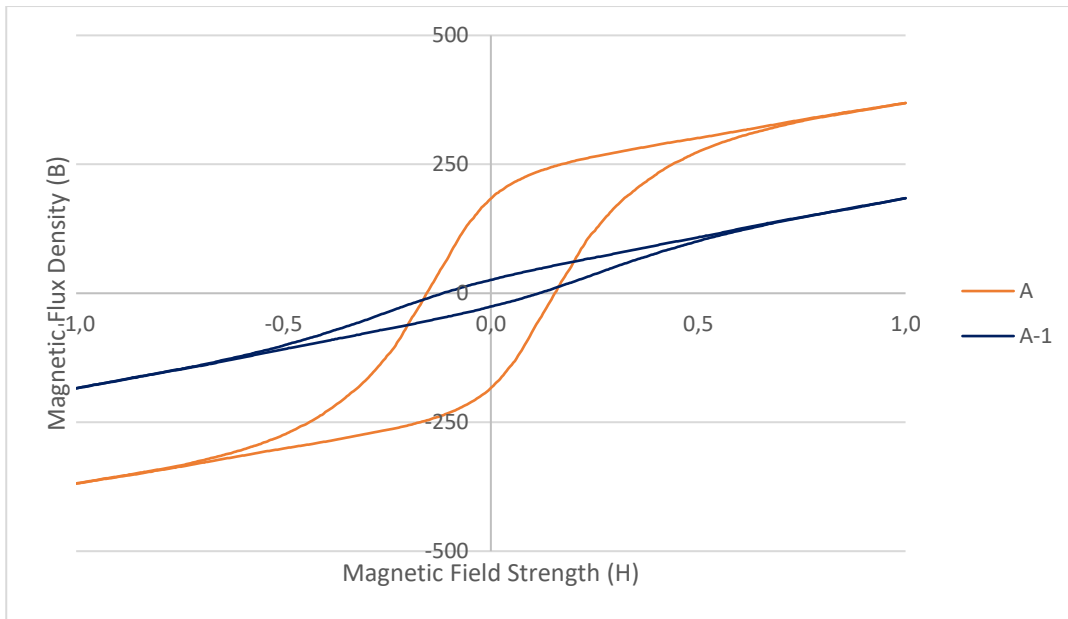


Figure 5.26. Magnetic hysteresis curves of A and A-1, showing the effect of cooling rate

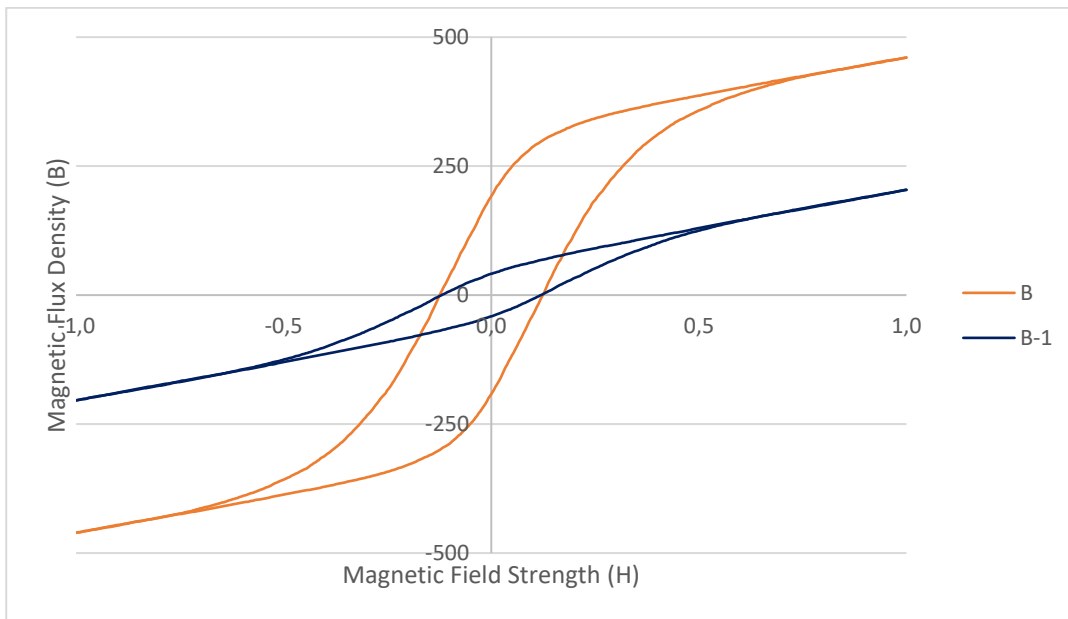


Figure 5.27. Magnetic hysteresis curves of B and B-1, showing the effect of cooling rate

While the difference of saturation values was higher at the air-cooled samples, that difference was reduced when cryogenic and tempering treatments were applied. For instance, air-cooled A and B had 369 and 461 saturation points, respectively. Whereas sub-zero treated and tempered A-2-2, B-2-2 had 174 and 186 (Figure 5.28).

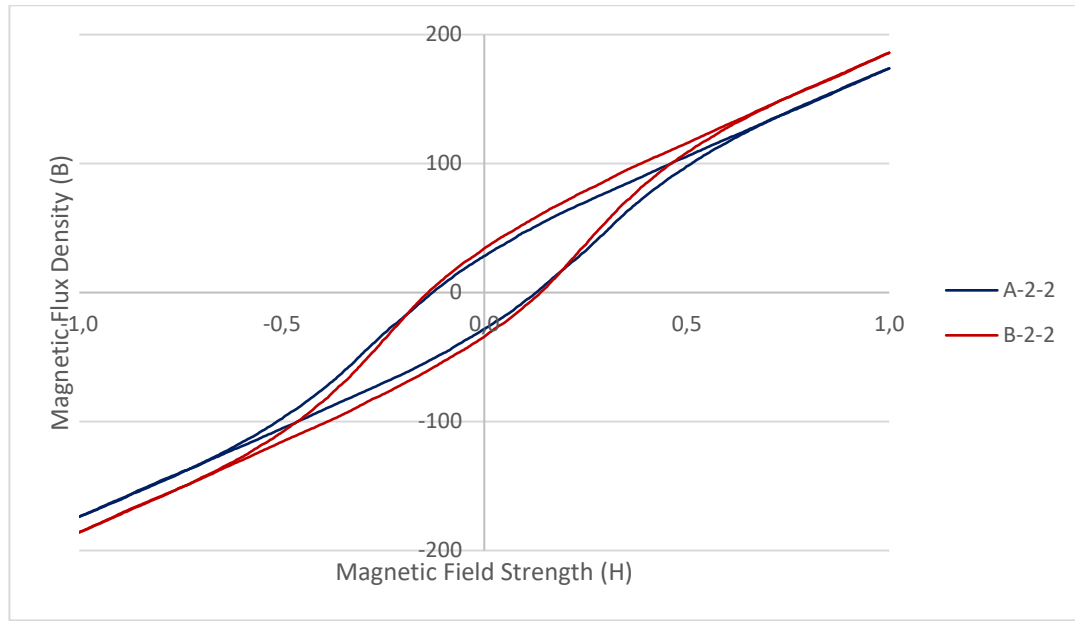


Figure 5.28. Magnetic hysteresis curves of A-2-2, B-2-2, showing the effect of cryogenic and tempering treatment on 3hours and 6hours carburized samples

Change in the sub-zero temperature affected the magnetic hysteresis, as the sub-zero temperature dropped saturation points decreased. For example, A-1-1, A-2-1, and A-3-1 were exposed to  $-25^{\circ}\text{C}$ ,  $-75^{\circ}\text{C}$ , and  $-100^{\circ}\text{C}$ , 169, 164, and 147 values were measured as saturation points. To see the effect of  $-25^{\circ}\text{C}$  treatment, the as-quenched A-1 was measured. It produced 184,3 values at the saturation point (Figure 5.29). It can also be said that, as the sub-zero treatment temperature is reduced magnetic hysteresis curve slightly rotates clockwise.

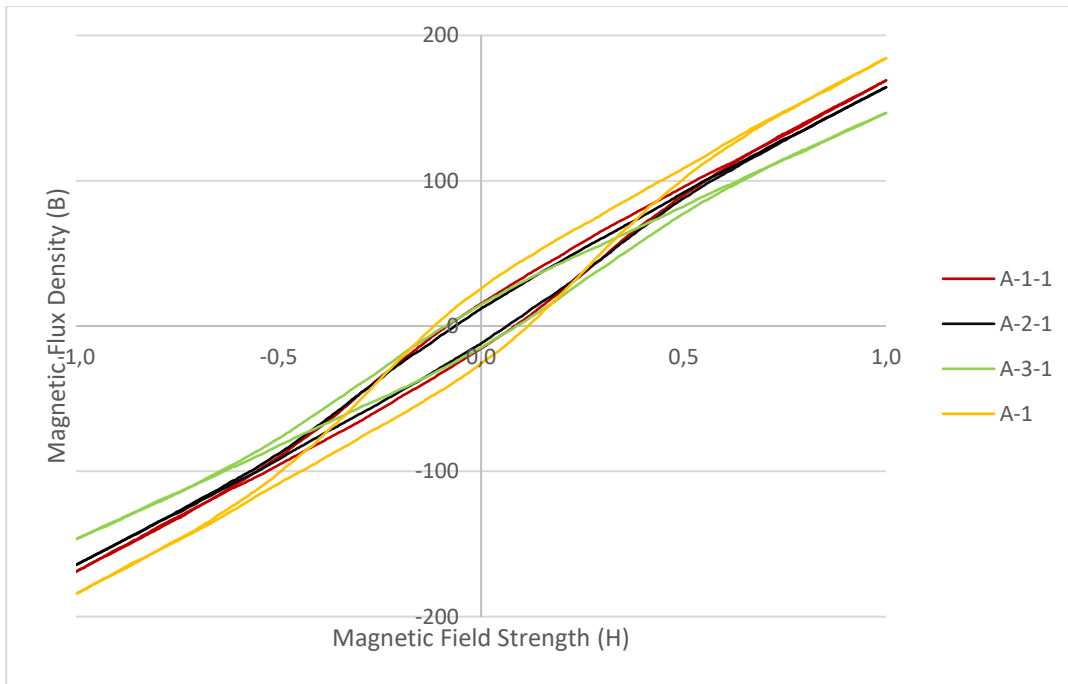


Figure 5.29. Magnetic hysteresis curves of A-1, A-1-1, A-2-1, A-3-1, showing the effect of sub-zero treatment temperature

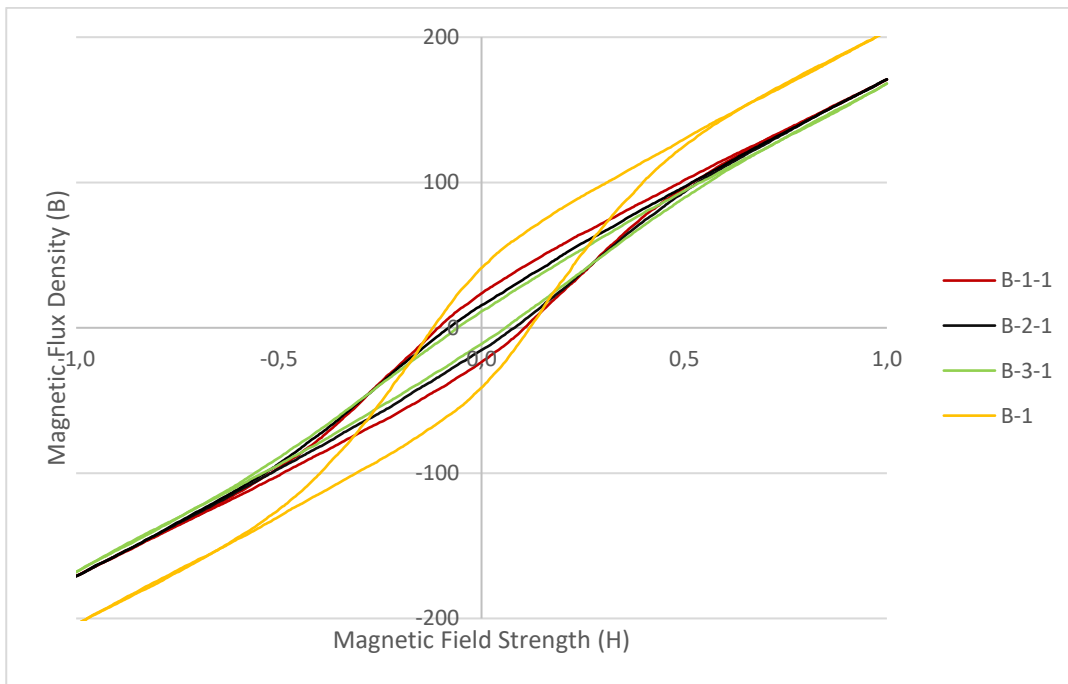


Figure 5.30. Magnetic hysteresis curves of B-1, B-1-1, B-2-1, B-3-1, showing the effect of sub-zero treatment temperature

However, the difference between saturation points of the sub-zero treated samples was to a small degree. For instance, B-1-1, B-2-1, and B-3-1 give nearly the same curves (Figure 5.30). Determining which curves belong to which sample solely by checking the hysteresis curves is a difficult issue if the measurements were performed after sub-zero treatment.

On the other hand, if the same tempering treatment was applied to sub-zero treated samples, the difference in hysteresis curves increased. For example, tempering treatment at 150°C was applied to the A-1-1, A-2-1, and A-3-1 samples, and they were renamed as A-1-2, A-2-2, and A-3-2 respectively. While in the sub-zero treated condition the difference at saturation levels between them was small but after tempering operation that difference increased (Figure 5.31). Moreover, the largest change was observed at -100°C, results at -25°C and -75°C were closer to each other than the results at -100°C treatment.

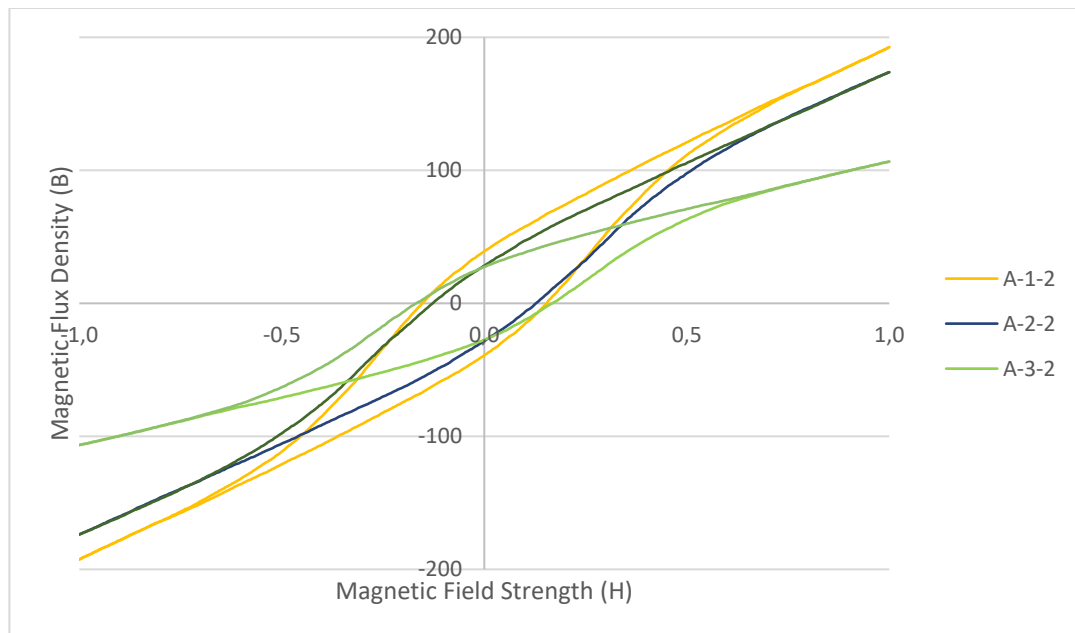


Figure 5.31. Magnetic hysteresis curves of A-1-2, A-2-2, A-3-2, showing the effect of sub-zero treatment temperature

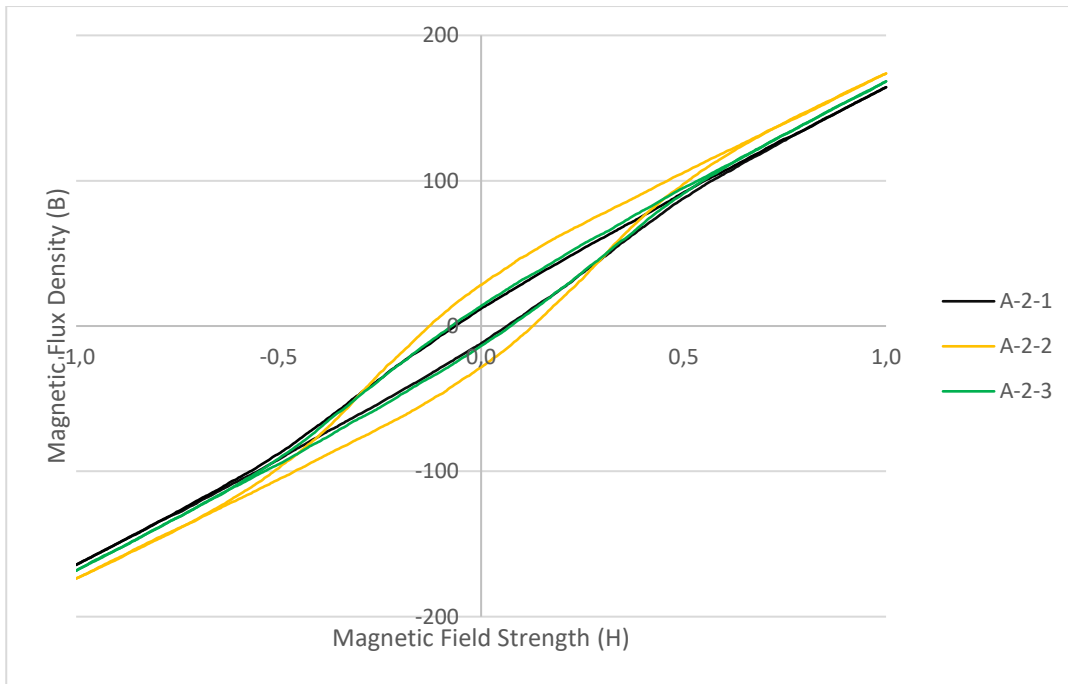


Figure 5.32. Magnetic hysteresis curves of A-2-1, A-2-2, A-2-3, showing the effect of tempering temperature

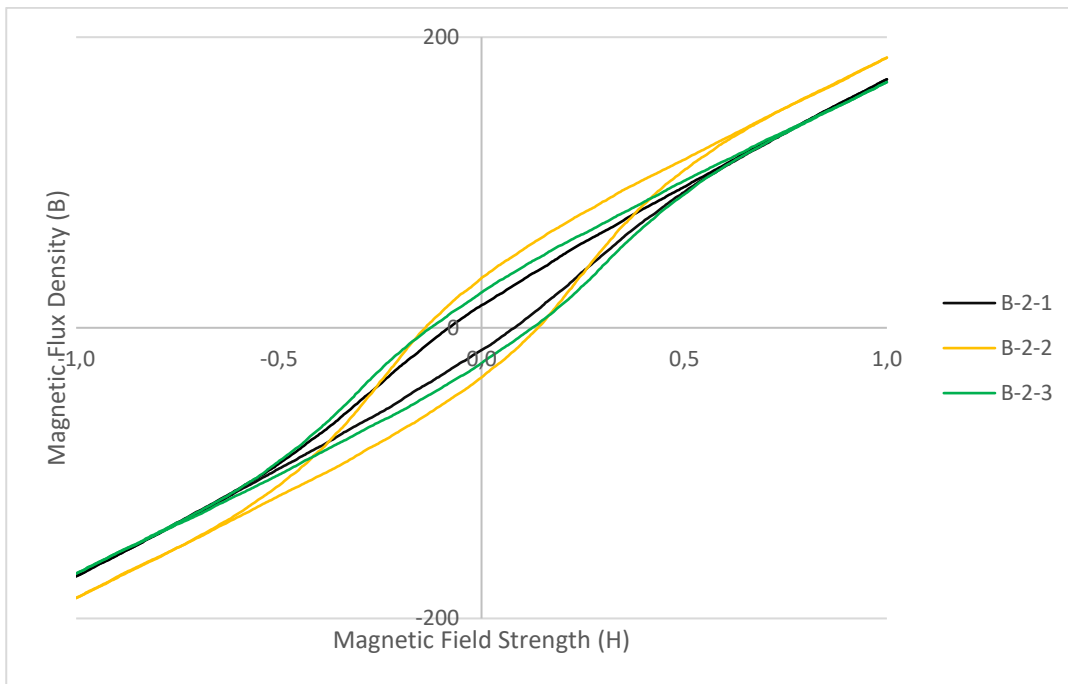


Figure 5.33. Magnetic hysteresis curves of B-2-1, B-2-2, B-2-3, showing the effect of tempering temperature

Magnetic hysteresis curves showed that the tempering temperature had a minor effect on the saturation and coercivity values of the samples. The experiment was planned to investigate tempering operations at 150°C and 300°C in addition to them, the untempered sample was also produced and measured to see the effect of tempering. For example, A-2-1, A-2-2, and A-3-2 were processed with the same recipe, except for the tempering temperature. A remarkable change wasn't monitored, however, 150°C made a small change and the 300°C sample had a nearly identical hysteresis curve with a sub-zero treated sample (Figure 5.32).

Similar results were also observed for the B group (Figure 5.33). Saturation values were reduced in the following order, B-2-2, B-2-1, and B-2-3. Additionally, the highest saturation values were obtained at 150°C tempered samples among the groups that were exposed to the same recipe until the tempering stage (Table 5.4).

Since the MBN emission is derived from magnetization cycles, a collection of rectified bursts represents a magnetic hysteresis loop. Saturation, remanence, and coercivity parameters can be obtained from the hysteresis loop, but they cannot be used as true values because magnetization was applied on the local spot in the MBN method [18].

## **5.5 XRD Results**

### **5.5.1 Residual Stress Measurements**

The measurements were carried out between -45° to 45° with 15 tilt angles. Then, d-spacings versus  $\sin^2(\psi)$  graphs were constructed (Figure 5.34). The principal residual stresses were calculated by equation 10. As the slope of the fitting decreases amount of compressive stress increases, the highest slope was observed on the A-3-1 sample, electropolishing was carried out.

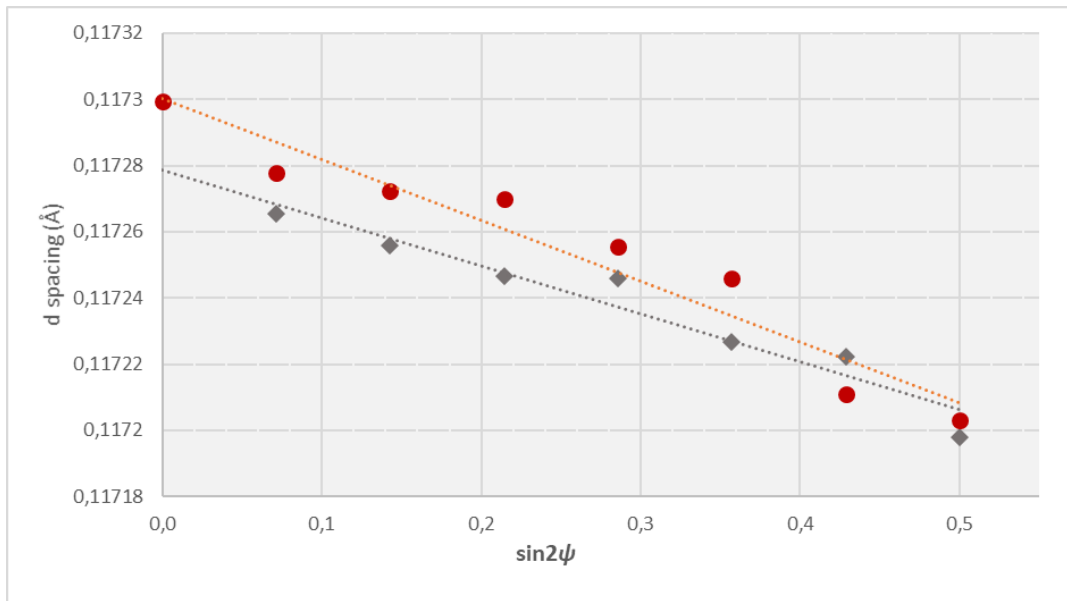


Figure 5.34. d-spacing versus  $\sin^2(\psi)$  values of the A-3-1 sample

X-ray diffraction results point out that increasing cooling rate rises the compressive residual stress. For example, A and B were air-cooled after carburizing process however, A-1 and B-1 were quenched into the oil. A-1 and B-1 samples show higher compressive stress both at as heat-treated surface and electropolished surface (Table 5.5). The important point is the difference between as heat-treated surface and electropolished surface results of air-cooled A and B samples 116 and 385MPa stress were measured respectively from the as heat-treated surface. But, after electropolishing, the stress states decrease to -236 and -244 MPa. Oxidation, decarburization, or stress relaxation may be regarded as the reason for such difference but further investigation has to be made.



Table 5.5 Magnitudes of principal surface residual stresses (effective) measured by XRD methods

Sample	Residual Stress (MPa) As heat-treated surface	Residual Stress (MPa) 30 $\mu$ m electropolished
<b>A</b>	116 $\pm$ 16	-236 $\pm$ 58
<b>A-1</b>	-363 $\pm$ 14	-259 $\pm$ 10
<b>A-1-1</b>	-423 $\pm$ 10	-458 $\pm$ 24
<b>A-3-1</b>	-458 $\pm$ 39	-509 $\pm$ 78
<b>A-3-3</b>	35 $\pm$ 13	80 $\pm$ 78
<b>B</b>	385 $\pm$ 27	-244 $\pm$ 12
<b>B-1</b>	-407 $\pm$ 26	-321 $\pm$ 201
<b>B-3-1</b>	-519 $\pm$ 13	-483 $\pm$ 103

The results show that the sub-zero treatment temperature had a dominant effect on the residual stress state. Sub-zero treatment wasn't applied to the A-1 sample and A-1-1, A-3-1 samples were treated at -25°C and -100°C, and residual stresses were calculated as -363MPa, -423MPa, and -458MPa respectively at as heat-treated surfaces (Figure 5.36). And the corresponding values at 30 $\mu$ m of electropolished surfaces were -259MPa, -458MPa, and -509MPa respectively (Figure 5.36). B-1 and B-3-1 had similar patterns. Hence, as sub-zero treatment temperature decreases the magnitude of the compressive residual stress on the surfaces of samples increases. According to Yan et al. sub-zero treatment increases the fine carbide precipitations and dislocation density [41]. Carbide precipitations rise the compressive residual stress on the steel part [49].

Tempering operation decreases the magnitude of the tensile and compressive residual stresses, i.e., it acted as a stress relief operation [48]. Moreover, tempering at 300°C annihilates any stress of the part (Figure 5.35 and 5.36). For example, the A-3-1 sample was sub-zero treated at -100°C and any tempering operation wasn't carried out. When 300°C tempering treatment was applied to it, the sample becomes A-3-3. The A-3-3 gave -458MPa and -509MPa at heat-treated and electropolished surfaces, but those measurements gave approximately 35MPa and 80MPa for the A-3-3.

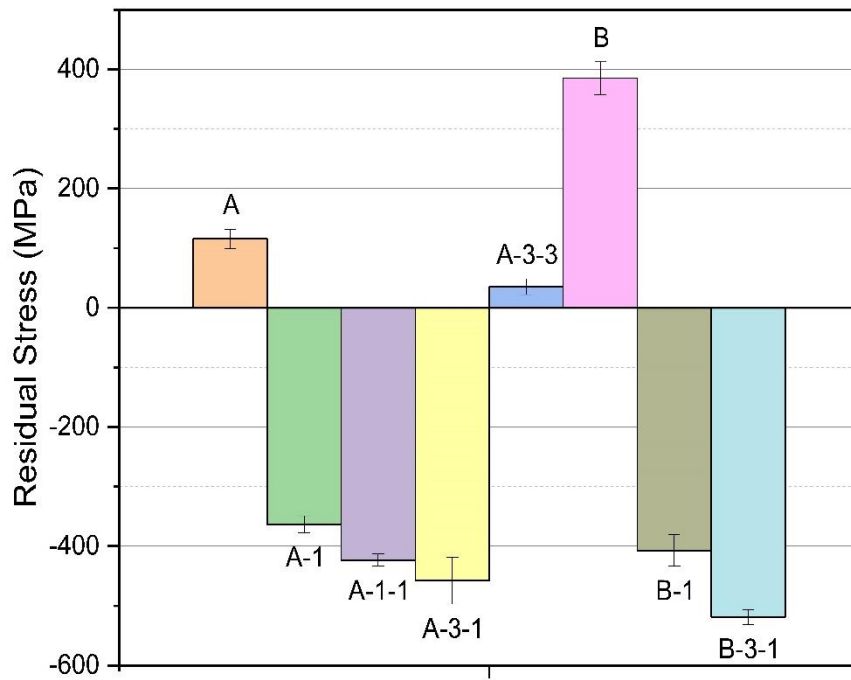


Figure 5.35. Magnitude of the surface residual stresses of the samples, as heat-treated surface

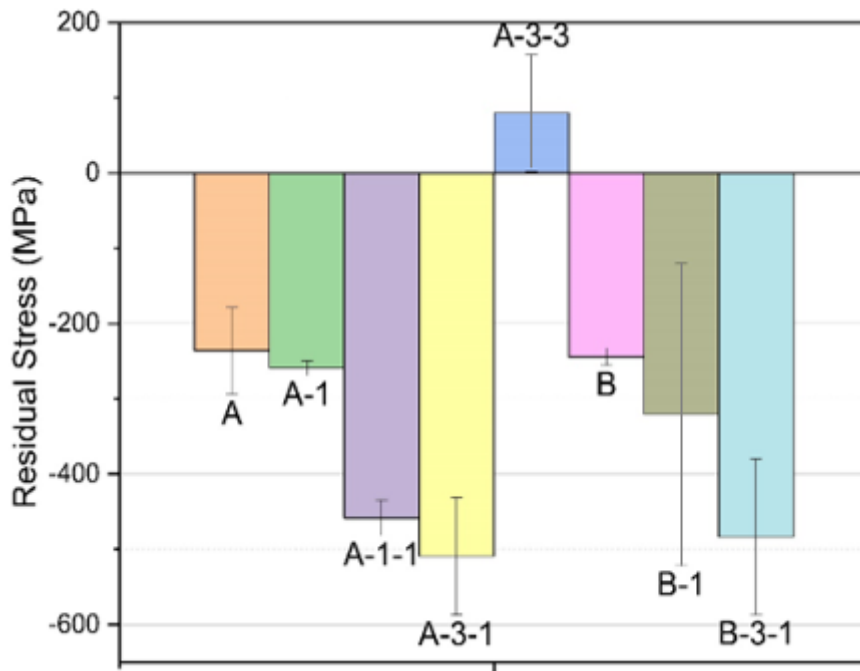


Figure 5.36. Magnitude of the surface residual stresses of the samples, after 30µm electropolishing

Carburizing time didn't show a big difference according to test results, A-1 and A-3-1 were carburized for 3 hours whereas B-1 and B-3-1 samples were carburized for 6 hours, the remaining recipe was the same for both groups. A-1 and B-1 gave a similar tendency for variation of the surface residual stress, the same results were valid for A-3-1 and B-3-1, too.

In addition to the residual stress measurements at 0 and 30µm depths for all samples, A and A-3-1 were analyzed in detail down to 600 µm depth (Table 5.6). A-3-1 gave a higher residual stress profile at each depth from A (Figure 5.37). Maximum stresses were measured at 0,4mm depth for both A and A-3-1 as -784MPa and -1167 MPa, respectively where 0,4mm depth corresponds to the case depth (513HV) (Table 5.6).

Table 5.6 Depth profiles of residual stresses for some samples, measured by XRD

Depth (mm)	A (MPa)	Depth (mm)	A-3-1 (MPa)
<b>0,000</b>	115 ± 16	<b>0,000</b>	-457 ± 39
<b>0,030</b>	-236 ± 57	<b>0,030</b>	-509 ± 78
<b>0,055</b>	-256 ± 28	<b>0,050</b>	-506 ± 42
<b>0,104</b>	-394 ± 40	<b>0,101</b>	-672 ± 26
<b>0,204</b>	-660 ± 46	<b>0,198</b>	-781 ± 65
<b>0,401</b>	-784 ± 62	<b>0,401</b>	-1167 ± 46
<b>0,606</b>	-595 ± 19	<b>0,597</b>	-777 ± 95

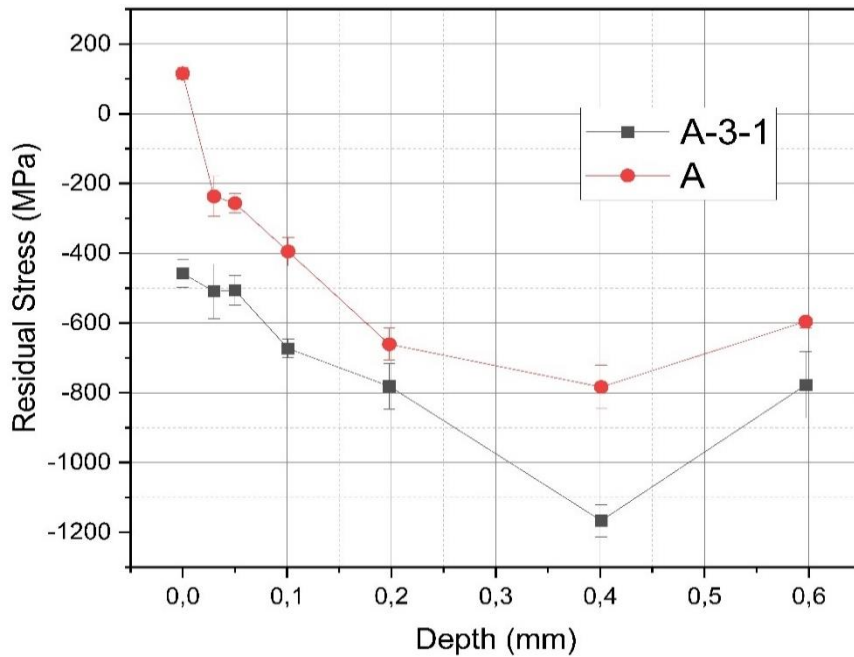


Figure 5.37. Residual stress profiles of the A and A-3-1 samples

Residual stress state obtained by XRD method and maximum peak level obtained by MBN method shows linear relation (Figure 5.38). Taking the A-3-3 sample as the outlier, there is an almost linear correlation between the residual stress and the MBN emission (the maximum peak height): the maximum compressive stress (-519MPa) corresponds to the minimum MBN emission (11mV) whereas the maximum tensile stress (385MPa) corresponds to the maximum MBN emission (79mV) (Table 5.7). Compressive residual stress causes a minimum MBN peak height, and the MBN emission increases as the magnitude of the compressive residual stress decreases, and it continues to increase with the increasing magnitude of the tensile residual stress.

Table 5.7 Surface hardness, MBN, retained austenite, and the principal surface residual stress values at electropolished surfaces of the samples

Sample	Surface Hardness (HV)	MBN Max. Peak Height (mV)	Retained Austenite by XRD (%)	Residual Stress by XRD (MPa)
A	817	64	18,8	-236
A-1	775	14	19,0	-259
A-1-1	842	12	15,0	-458
A-3-1	905	10	6,6	-509
A-3-3	668	11	<1	80
B	763	79	18,4	-244
B-1	698	19	25,4	-321
B-3-1	888	11	7,9	-483

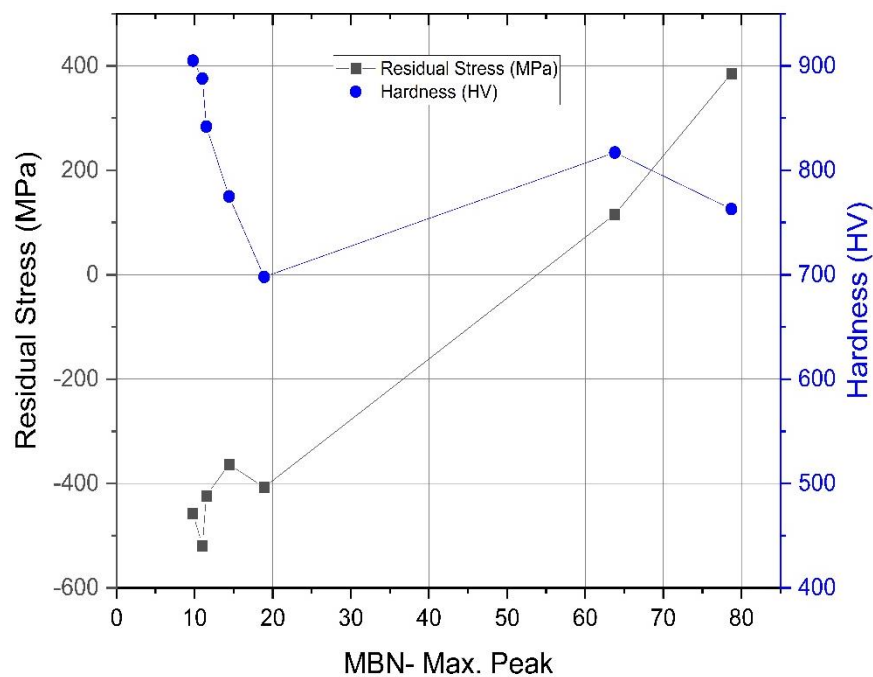


Figure 5.38. Graph of the surface residual stresses measured by XRD versus the MBN max. peak height and the hardness values

It was observed that residual stresses were more dominant than the hardness on MBN results. For instance, the samples containing compressive residual stress displayed low MBN signals independent of the hardness values (Figure 5.38). The samples that contain tensile residual stress exhibit high MBN signals even if they have high hardness values. A-1 has -363MPa residual stress and 775HV hardness, B has 385MPa and 763HV respectively. And their corresponding MBN maximum peak levels were 14,4 and 78,7mV. In that comparison hardness values are nearly the same and indicate that the MBN method is so sensitive to residual stress change. A-1-1 had -423MPa residual stress and 842HV hardness, B-1 had -407MPa and 698HV, respectively. Their corresponding MBN maximum peak levels were 11,5 and 18,9mV. It is seen that the change in hardness values affects the MBN emissions but, residual stress has a pronounced effect on MBN.

Multiple regression analysis was performed to observe the quantitative effect of surface hardness (HV), retained austenite (R.A.), and the principal residual stresses (R.S) at 30µm electropolished surfaces on the MBN-RMS emission using the data of Table 5.7. Since the magnitude of residual stress and the MBN signals are material and geometry dependent, the analysis is valid only for the experimental setups. Equation 17 also shows that retained austenite content and the hardness decreases the MBN signals whereas an increase in the magnitude of residual stress increases the MBN signals.

$$\text{MBN-RMS}=0,1*\text{R.S.}-0,9*\text{R.A.}-0,01*\text{HV}+70,6 \quad (\text{R}^2=0,78) \quad \text{Eq.17}$$

## CHAPTER 6

### CONCLUSION

This research aimed to determine non-destructively the variations in the microstructure and residual stress at the surface of the carburized AISI SAE 9310 steel components by the Magnetic Barkhausen Noise (MBN) method.

A series of specimens having different microstructure and residual stress states were prepared by changing the cooling rate, the carburizing time, the cryogenic treatment temperature, and the tempering temperature whereas the other process parameters were kept constant. All specimens were carefully characterized through metallographic investigation, hardness measurement, retained-austenite determination via the XRD method, measurement of residual stresses with the XRD method, and the MBN measurements.

The following conclusions can be drawn from this thesis study:

- In the as-quenched condition, martensite and some retained-austenite exist in the hardened zone of all samples. At constant austenitizing temperature, as the time for carbon diffusion is increased from 3h to 6h, the C-content of the surface, the amount of the retained-austenite increase, and the case depth, which corresponds to the maximum hardness and also the maximum compressive residual stress increases. The magnetic parameters obtained by the MBN measurements can differentiate any alteration in the microstructure and the residual stress.
- Sub-zero treatment of the quenched samples remarkably changes the microstructure and the residual stress by reducing % retained-austenite with a corresponding rise in the magnitude of compressive residual stress. A decrease in sub-zero treatment reduces the MBN-RMS level and the hysteresis curve's saturation point.

- After the sub-zero treatment, as the tempering temperature is increased from 150°C to 300°C, carbide transformation is replaced by cementite and ferrite formation, and the surface hardness is reduced remarkably with changing the residual stress state, compressive to tension. An increase in tempering temperature rises the MBN-RMS by the action of both the microstructural and the residual stress state alteration.
- An almost linear relationship exists between the residual stress and the MBN emission. The maximum compressive stress corresponds to the minimum MBN emission, and the maximum tensile stress corresponds to the maximum MBN emission. A decrease in the magnitude of the compressive residual stress, and a further increase in the magnitude of tensile residual stress results in a remarkable increase in the MBN emission. However, if there is a considerable change in the microstructure together with the residual stress, the individual effects of both factors on the MBN emission cannot be distinguished due to combined effect of the factors.

The overall results show that a good correlation exists between the results, i.e., microstructure and residual stress, obtained by the conventional methods and the parameters derived from the MBN signals such as MBN-RMS, MBN max. peak height, the relative hysteresis curve. Based on the detailed experimental analysis, it can be concluded that the MBN parameters measured are sensitive to the alterations in the microstructure and residual stress at the surface of the carburized steels. This method has the potential to be used as a fast and reliable non-destructive tool for the qualitative control of the success of the carburizing process stages. Moreover, if there is not any significant change in the microstructure, it can also be used to measure the magnitude of the residual stress after completing a careful pre-calibration/correlation procedure.



## 6.1 Recommendations for Further Studies

The following issues are recommended for further studies;

- The MBN calibration should be done with a large number of samples with tensile and compressive residual stress.
- The effect of higher tempering temperatures on the MBN voltage should be investigated and correlated with the residual stress measurements by XRD.
- While measuring the magnitude of residual stress by XRD, some assumptions are made such as  $d_0$  of the samples obtained from d-spacing versus  $\sin^2(\psi)$  graph and  $\sigma_{33}$  excepted as zero, the  $d_0$  should be measured accurately from powder form of the sample.
- Effect of grain size and distribution and size of the precipitates on the MBN emission should be examined.



## REFERENCES

- [1] Zhichao Li, Andrew M. Freborg, Bruce D. Hansen & T. S. Srivatsan,(2012). “*Modeling the Effect of Carburization and Quenching on the Development of Residual Stresses and Bending Fatigue Resistance of Steel Gears*”, Journal of Materials Engineering and Performance volume 22, pp.664–672
- [2] M.Deveci, (2016). “*Non Destructive Determination of Case Depth by Barkhausen Noise Method*”, MSc Thesis, Tampere University of Technology
- [3] D.Dragomir, M.O.Cojocaru, N. Dumitru, (2013). “*The Effect of Change of Carburizing Media Nature on Growth Kinetics of Layers*”, U.P.B. Sci. Bull., Series B, Vol. 75, Iss. 1,
- [4] O.Karabelchtchikova, (2007), “*Fundamentals of Mass Transfer in Gas Carburizing*” ,PhD Thesis, Worcester Polytechnic Institute
- [5] Callister, W. D., Rethwisch, D. G. (2020). *Diffusion. In Materials science and engineering*. NJ: Wiley. pp. 119-120
- [6] Linde Gas” Furnace Atmospheres No. 1Gas Carburizing and Carbonitriding Carburising; Carbonitriding” (n.d.). Retrieved January 17, 2021, from [https://www.lindegas.com/en/processes/heat\\_treatment/carburising\\_carbonitriding/index.html](https://www.lindegas.com/en/processes/heat_treatment/carburising_carbonitriding/index.html)
- [7] Pacific Metallurgical, Inc. (n.d.). Retrieved January 17, 2021, from <http://www.pacmet.com/index.php?h=basicheatreat#:~:text=Austenitizing%20heat%20treatment%20is%20heating,transform%20the%20austenite%20into%20martensite.>
- [8] Schulze, J. (2019). *A technical guide to quenching*. Retrieved January 17, 2021, from <https://thermalprocessing.com/a-technical-guide-to-quenching/>

- [9] Withers, P. J., Bhadeshia, H. K. D. H. (2001). *Residual stress. part 1 – measurement techniques. Materials Science and Technology*, 17(4), 355–365. <https://doi.org/10.1179/026708301101509980>
- [10] M.E. Fitzpatrick, A.T. Fry, P. Holdway, F.A. Kandil, J. Shackleton and L. Suominen, (2005) *Determination of Residual Stresses by X-ray Diffraction*. National Physical Laboratory, United Kingdom
- [11] Schields J.P, (2204). “Bragg’s Law and Diffraction: How waves reveal the atomic structure of crystals”. <http://skuld.bmsc.washington.edu/~merritt/bc530/bragg/#:~:text=Deriving%20Bragg's%20Lawtext=%3D%20AB%20%2BBC%20.,adjacent%20to%20the%20top%20beam.>
- [12] Cullity, B. D., Stock, S. R. (2015). *Elements of X-ray diffraction. Stress Measurement*, Pearson India Education Services.
- [13] Motazedian, F., Wu, Z., Zhang, J., Shariat, B., Jiang, D., Martyniuk, Yang, H., (2019). *Determining intrinsic stress and strain state of fibre-textured thin films by X-ray diffraction measurements using combined asymmetrical and Bragg-Brentano configurations.* <https://www.sciencedirect.com/science/article/pii/S0264127519305015>
- [14] *X-ray Diffraction.* (2020). <https://www.stresstech.com/knowledge/non-destructive-testing-methods/x-ray-diffraction/>
- [15] Vaidhianathasamy M., April 2016, *Important Factors Influencing the Magnetic Barkhausen Noise Profile*, [https://www.researchgate.net/publication/284281190\\_Important\\_Factors\\_Influencing\\_the\\_Magnetic\\_Barkhausen\\_Noise\\_Profile](https://www.researchgate.net/publication/284281190_Important_Factors_Influencing_the_Magnetic_Barkhausen_Noise_Profile)
- [16] Nave C.R., (2017). *Ferromagnetism*, <http://hyperphysics.phy-astr.gsu.edu/hbase/Solids/ferro.html>

- [17] Xiong, E., Zhao, N., Yan, Z., Yang, L, He, H. (2016). *Magnetic nondestructive testing techniques of Constructional Steel*. MATEC Web of Conferences, 43, 03002. <https://doi.org/10.1051/mateconf/20164303002>
- [18] Kaleli, T. (2017). *Determination of Residual Stress State in SAE/AISI 8620 Carburized Steel by Non-Destructive Testing Methods*. MSc Thesis, Middle East Technical University.
- [19] *Application note: Non-destructive Testing on Gear Teeth*, (2020). <https://www.stresstech.com/application-note-non-destructive-testing-on-gear-teeth/>
- [20] Deveci M., (2017). *Stresstech Bulletin 2: The properties of Barkhausen*, <https://www.stresstech.com/stresstech-bulletin-2-the-properties-of-barkhausen-noise/>
- [21] *Barkhausen Noise Analysis*, (n.d.). <https://www.stresstech.com/knowledge/non-destructive-testing-methods/barkhausen-noise-analysis/>
- [22] ASTM International - Standards Worldwide (2016). *Standard practice for X-ray determination of retained austenite in steel with near random crystallographic orientation*. Retrieved February 22, 2022, from <https://www.astm.org/e0975-13.html>
- [23] V. Moorthy, B.A. Shaw, P. Mountford, P. Hopkins, (2005). *Magnetic Barkhausen emission technique for evaluation of residual stress alteration by grinding in case-carburised En36 steel*
- [24] H.Hızlı, (2016), *Nondestructive monitoring of the variations in microstructure and residual stress in carburized steels*, MSc Thesis, Middle East Technical University.
- [25] M.M.Blaow, M.A Ballem, B.A.Shaw, (2019). *Nondestructive characterization of subsurface plastic deformation in case carburized steel using magnetic barkhausen noise technique*

- [26] American Gear Manufacturers Association. (2005). *Recommended Practice for Carburized Aerospace Gearing*, AGMA 926-C99 (reaffirmed November 29, 2017).<https://members.agma.org/ItemDetail?iProductCode=926C99&Category=STANDARDS>
- [27] Hauk, V., & Behnken, H. (2006). *Two-phase materials*. In Structural and residual stress analysis by nondestructive methods: Evaluation - application - assessment (pp. 266–270)., Elsevier.
- [28] Murray, C. E., Noyan, C. (2013). *Applied and Residual Stress Determination Using X-ray Diffraction*. Practical Residual Stress Measurement Methods, First Edition. Edited by Gary S. Schajer. John Wiley & Sons, Ltd. Published 2013 by John Wiley & Sons, Ltd.
- [29] Buzzetti, O., Merletti, L.G., Fusari, M., Pezzoni, R. (n.d.). *Residual Stress Evaluation in Helicopter Gears Through Barkhausen Noise Measurement*.
- [30] Lo, C. C., Kinser, E. R., Jiles, D. C. (2006). *Analysis of barkhausen effect signals in surface-modified magnetic materials using a hysteretic-stochastic model*. Journal of Applied Physics, 99(8). <https://doi.org/10.1063/1.2163272>
- [31] Anglada-Rivera, J., Padovese, L. R., Capó-Sánchez, J. (2001). *Magnetic Barkhausen noise and hysteresis loop in commercial carbon steel: Influence of applied tensile stress and grain size*. Journal of Magnetism and Magnetic Materials, 231(2-3), 299–306. [https://doi.org/10.1016/s0304-8853\(01\)00066-x](https://doi.org/10.1016/s0304-8853(01)00066-x)
- [32] Moorthy, V., Vaidyanathan, S., Jayakumar, T., Raj, B. (1997). *Microstructural characterization of quenched and tempered 0.2% carbon steel using Magnetic Barkhausen Noise Analysis*. Journal of Magnetism and Magnetic Materials, 171(1-2), 179–189. [https://doi.org/10.1016/s0304-8853\(97\)00049-8](https://doi.org/10.1016/s0304-8853(97)00049-8)
- [33] Moorthy, V., Shaw, B. A., Evans, J. T. (2003). *Evaluation of tempering induced changes in the hardness profile of case-carburised EN36 steel using Magnetic Barkhausen Noise Analysis*. NDT E International, 36(1), 43–49. [https://doi.org/10.1016/s0963-8695\(02\)00070-1](https://doi.org/10.1016/s0963-8695(02)00070-1)

- [34] Gür, C. H., Çam, İ. (2007). *Comparison of magnetic barkhausen noise and ultrasonic velocity measurements for microstructure evaluation of SAE 1040 and SAE 4140 Steels*. *Materials Characterization*, 58(5), 447–454. <https://doi.org/10.1016/j.matchar.2006.06.008>
- [35] Arslan E., Murathan Ö.F., Davut K., Kılıçlı V. (2016) *Evaluation of the Microstructure of AISI D2 Steel by Magnetic Barkhausen Noise Technique*. Conference: 18th International Metallurgy & Materials Congress (IMMC2016). [https://www.researchgate.net/publication/311592715\\_Evaluation\\_of\\_the\\_Microstructure\\_of\\_AISI\\_D2\\_Steel\\_by\\_Magnetic\\_Barkhausen\\_Noise\\_Technique](https://www.researchgate.net/publication/311592715_Evaluation_of_the_Microstructure_of_AISI_D2_Steel_by_Magnetic_Barkhausen_Noise_Technique)
- [36] Davut, K., Hakan Gür, C. (2007). *Monitoring the microstructural changes during tempering of quenched SAE 5140 steel by Magnetic Barkhausen Noise*. *Journal of Nondestructive Evaluation*, 26(2-4), 107–113. <https://doi.org/10.1007/s10921-007-0025-x>
- [37] Gur, C. H. (2018). *Review of residual stress measurement by Magnetic Barkhausen Noise technique*. *Materials Performance and Characterization*, 7(4), 20170080. <https://doi.org/10.1520/mpc20170080>
- [38] Wang, Yanfei & Gong, Jianzhou & Rong, D. & Gao, F.. (2014). *Measurement and calculation of carbon concentration and diffusion-induced stress in stainless steelafter low temperature gas carburizing*. *Jinshu Xuebao/Acta Metallurgica Sinica*. 50. 409-414. 10.3724/SP.J.1037.2013.00537.
- [39] G, Ramesh & Prabhu, Narayan. (2011). *Review of thermo-physical properties, wetting and heat transfer characteristics of nanofluids and their applicability in industrial quench heat treatment*. *Nanoscale research letters*. 6. 334. 10.1186/1556-276X-6-334.
- [40] *Scattering and Diffraction. The Bragg's Law* (n.d.) [https://www.xtal.iqfr.csic.es/Cristalografia/parte\\_05\\_5-en.html](https://www.xtal.iqfr.csic.es/Cristalografia/parte_05_5-en.html)

- [41] Yan, Y., Liu, K., Luo, Z., Wang, M., Wang, X. (2021). *Effect of cryogenic treatment on microstructure, mechanical properties and distortion of carburized gear steels*. *Metals*, 11(12), 1940. <https://doi.org/10.3390/met11121940>
- [42] Prieto, G., Tuckart, W. R., Perez Ipiña, J. E. (2017). *Influence of a cryogenic treatment on the fracture toughness of an AISI 420 martensitic stainless steel*. *Materiali in Tehnologije*, 51(4), 591–596. <https://doi.org/10.17222/mit.2016.126>
- [43] Moorthy, V., Shaw, B., Hopkins, P. (2006). *Surface and subsurface stress evaluation in case-carburised steel using high and low frequency Magnetic Barkhausen emission measurements*. *Journal Of Magnetism And Magnetic Materials*, 299(2), 362-375.
- [44] *ASM material data sheet*. (n.d.). Retrieved February 3, 2022, from <http://asm.matweb.com/search/SpecificMaterial.asp?bassnum=M931AL>
- [45] *Permeability. Engineering ToolBox*. (n.d.). Retrieved February 3, 2022, from [https://www.engineeringtoolbox.com/permeability-d\\_1923.html](https://www.engineeringtoolbox.com/permeability-d_1923.html)
- [46] ASTM International Standards Worldwide. (2017). *Standard test methods for determining average grain size*. Retrieved February 3, 2022, from <https://www.astm.org/e0112-96r04.html>
- [47] SAE International, (2014). *AMS2759/7b: Carburizing and heat treatment of carburizing grade steel parts - SAE international. AMS2759/7B: Carburizing and Heat Treatment of Carburizing Grade Steel Parts* , Retrieved February 3, 2022, from <https://www.sae.org/standards/content/ams2759/7b/>
- [48] Kaleli, T., Gür, C. H. (2020). *Determination of surface residual stresses in carburised AISI 8620 steel by the Magnetic Barkhausen Noise Method*. *Insight - Non-Destructive Testing and Condition Monitoring*, 62(7), 416–421. <https://doi.org/10.1784/insi.2020.62.7.416>



- [49] Wei, Y. H., Yu, X. F., Su, Y., Shen, X. Y., Xia, Y. Z., Yang, W. W. (2021). *Effect of residual stress and microstructure evolution on size stability of M50 Bearing Steel*. Journal of Materials Research and Technology, 10, 651–661. <https://doi.org/10.1016/j.jmrt.2020.12.060>
- [50] Gavriljuk, V.G., Sirosh, V.A., Petrov, Y.N., (2014). *Carbide Precipitation During Tempering of a Tool Steel Subjected to Deep Cryogenic Treatment*. Metall Mater Trans A 45, 2453–2465. <https://doi.org/10.1007/s11661-014-2202-8>
- [51] Haiko, O., Kaijalainen, A., Pallaspuuro, S., Hannula, J., Porter, D., Liimatainen, T., Kömi, J. (2019). *The effect of tempering on the microstructure and mechanical properties of a novel 0.4c press-hardening steel*. Applied Sciences, 9(20), 4231. <https://doi.org/10.3390/app9204231>
- [52] Yamaura, S. (2001). *The effect of grain boundary microstructure on Barkhausen noise in ferromagnetic materials*. Acta Materialia, 49(15), 3019–3027. [https://doi.org/10.1016/s1359-6454\(01\)00189-6](https://doi.org/10.1016/s1359-6454(01)00189-6)
- [53] Kahrobaee, S., Kashefi, M. (2015). *Assessment of retained austenite in AISI D2 tool steel using magnetic hysteresis and Barkhausen noise parameters*. Journal of Materials Engineering and Performance, 24(3), 1192–1198. <https://doi.org/10.1007/s11665-014-1337-5>
- [54] SAE International (2020). AMS2750: Pyrometry - SAE international. AMS2750: Pyrometry, Retrieved February 12, 2022, from <https://www.sae.org/standards/content/ams2750/>
- [55] Prevey, P. (2014). *X-ray diffraction residual stress techniques*. Retrieved February 12, 2022, from [https://www.academia.edu/6630504/X-RAY\\_DIFFRACTION\\_RESIDUAL\\_STRESS\\_TECHNIQUES](https://www.academia.edu/6630504/X-RAY_DIFFRACTION_RESIDUAL_STRESS_TECHNIQUES)
- [56] Macherauch, E., Vöhringer, O. (1992). *Residual stresses after quenching*. Theory and Technology of Quenching, 117–181. [https://doi.org/10.1007/978-3-662-01596-4\\_6](https://doi.org/10.1007/978-3-662-01596-4_6)

[57] Réti, Tamás. (2003). *Residual Stresses in Carburised, Carbonitrided, and Case-hardened Components (Part 1)*. Heat Treatment of Metals. 30. 83-96.

[58] Luo, Q. (2022). *A modified X-ray diffraction method to measure residual normal and shear stresses of machined surfaces*. The International Journal of Advanced Manufacturing Technology. <https://doi.org/10.1007/s00170-021-08645-4>

## APPENDICES

### A. TTT Diagrams of 9310 Steel at Initial, 3 h and 6 h Carburized Condition

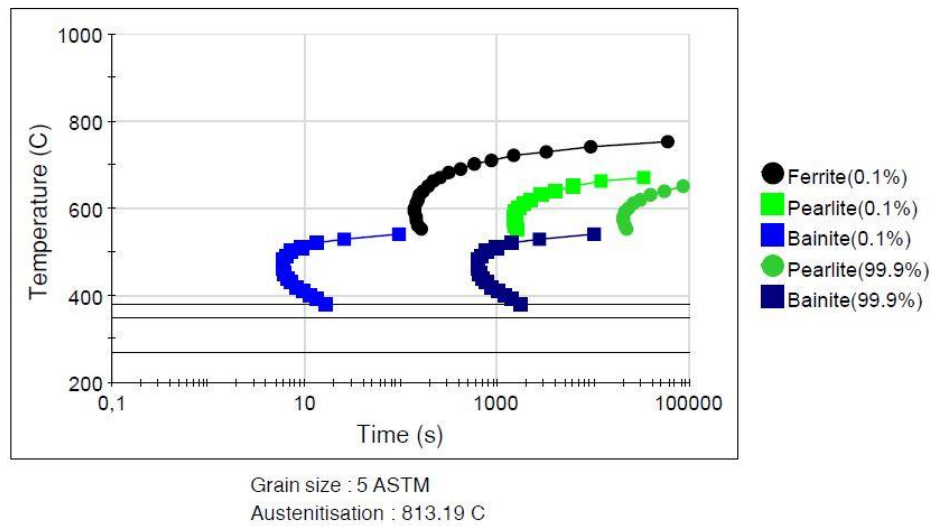


Figure A.1. TTT diagram of 9310 steel at initial condition, calculated by JMatPro

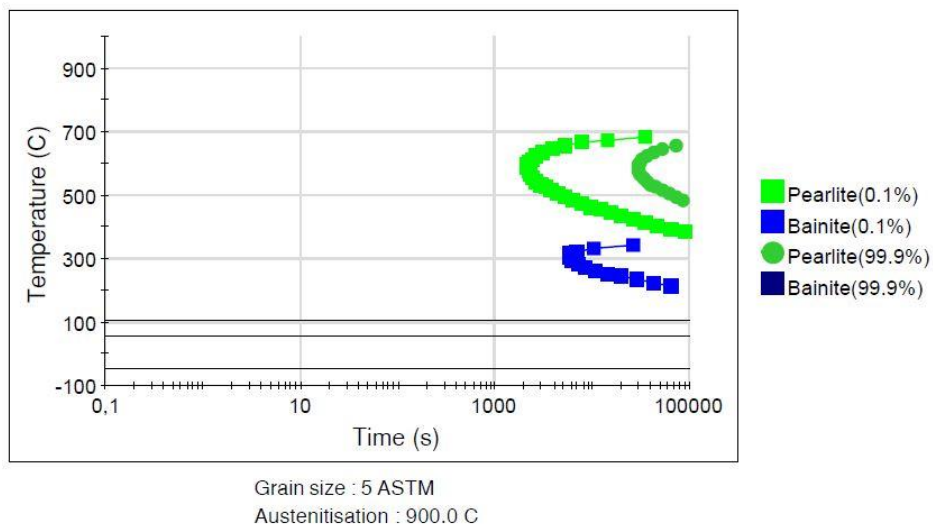


Figure A.2. TTT diagram of 3 hours carburized 9310 steel that surface carbon content reached 0,91 wt.%C, calculated by JMatPro

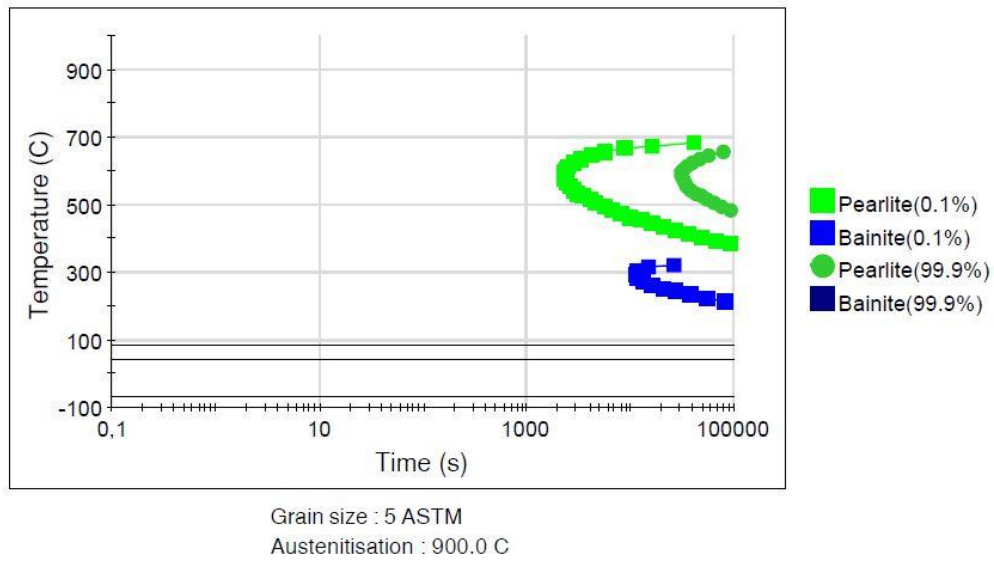


Figure A.3. TTT diagram of 6 hours carburized 9310 steel that surface carbon content reached 0,97wt.%C, calculated by JMatPro

**B. CCT Diagrams of 9310 Steel at Initial, 3 h and 6 h Carburized Condition**

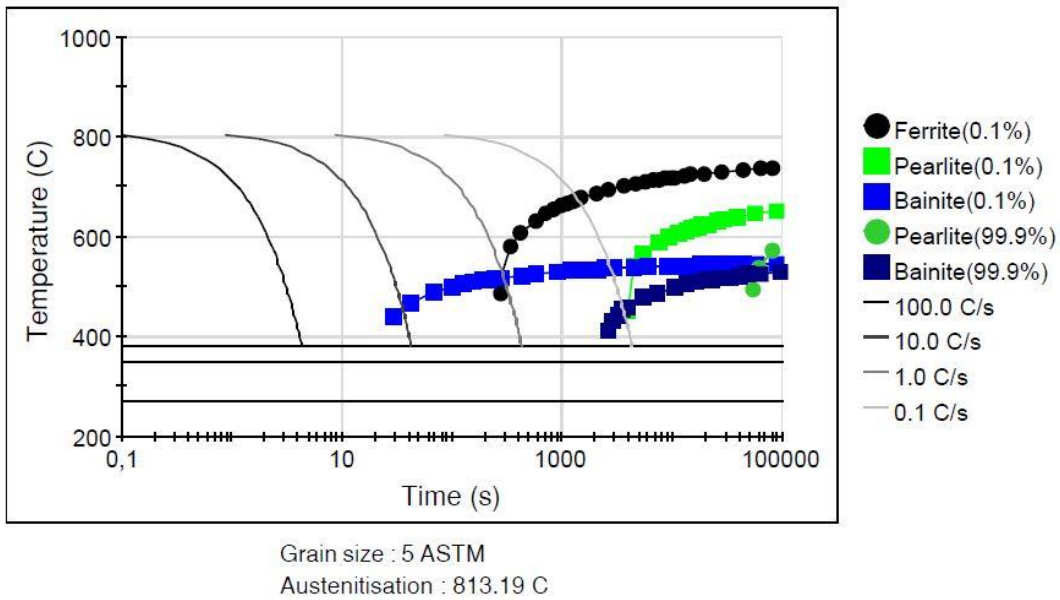


Figure B.4. CCT diagram of 9310 steel at initial condition, calculated by JMatPro

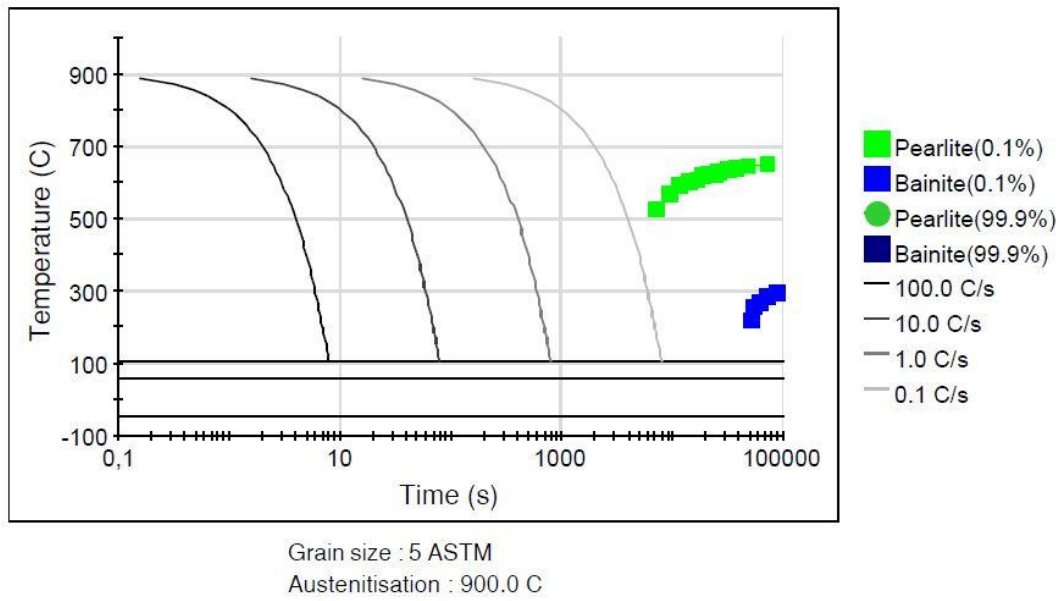


Figure B.5. CCT diagram of 3 hours carburized 9310 steel that surface carbon content reached 0,91wt.%C, calculated by JMatPro

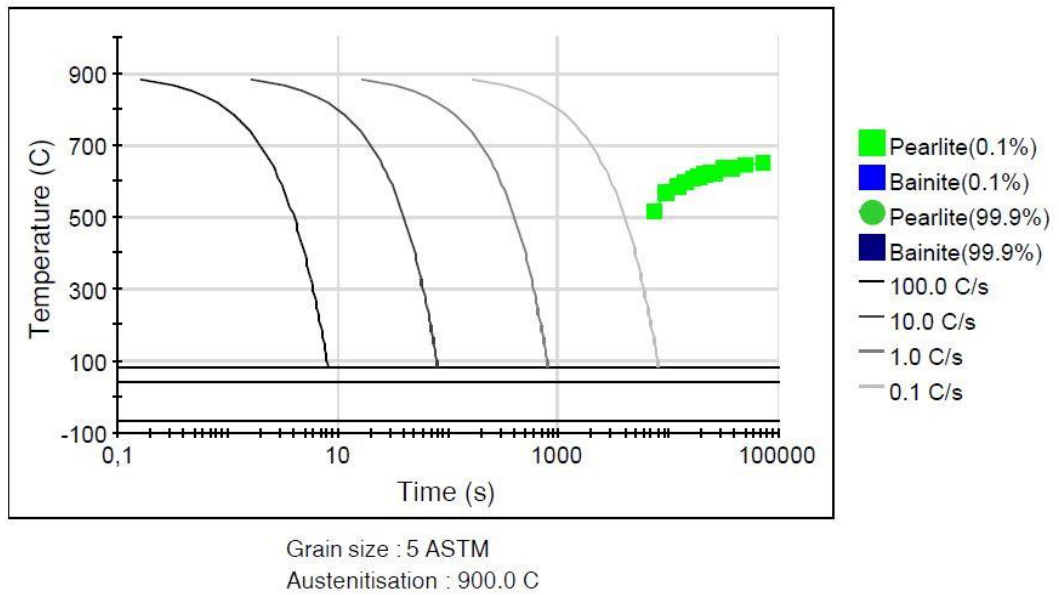


Figure B.6. CCT diagram of 3 hours carburized 9310 steel that surface carbon content reached 0,97wt.%C, calculated by JMatPro